Title
Electron driven instabilities around dipolarizing flux bundles in Earth’s magnetotail

Author
Zhang, Xu

Publication Date
2021

UNIVERSITY OF CALIFORNIA

Los Angeles

Electron driven instabilities around dipolarizing flux bundles in Earth’s magnetotail

A dissertation submitted in partial satisfaction of the requirements

for the degree Doctor of Philosophy

in Geophysics and Space Physics

by

Xu Zhang

2021

ABSTRACT OF THE DISSERTATION

Electron driven instabilities around dipolarizing flux bundles in Earth's magnetotail

by

Xu Zhang

Doctor of Philosophy in Geophysics and Space Physics

University of California, Los Angeles, 2021

Professor Vassilis Angelopoulos, Chair

Dipolarization fronts (DFs) are transient phenomena in the magnetotail with various types of waves observed in their vicinity. The potential effect of these fluctuations on particle distributions and energy conversion near DFs is poorly understood. In this study, we aim to determine the relations between waves and dipolarization fronts. Using observational data from Time History of Events and Macroscale Interactions during Substorms (THEMIS), we established whistler wave event database and electron cyclotron harmonic (ECH) wave event database near dipolarization fronts from year 2007-2017. We find that electron temperature anisotropies are well-constrained by the marginal stability thresholds of whistler instability and electron firehose instability. During earthward transport of electrons, a significant portion of the suprathermal electron energy flux is evacuated in the form of whistler wave Poynting flux. Later we investigate the generation mechanism of ECH waves near dipolarization fronts. We find that moderately oblique (with wave normal angle at around 70^{o}) ECH waves are frequently observed behind DFs and they are driven unstable by low energy electron beams. By performing a parametric survey of beam-driven ECH waves, we demonstrate that these waves are unstable under a wide range of plasma conditions. This work emphasizes the importance of wave-particle interaction in the magnetotail.

This dissertation of Xu Zhang is approved.

Jacob Bortnik

Robert J. Strangeway

Marco Velli

Vassilis Angelopoulos, Committee Chair

University of California, Los Angeles

2021

TABLE OF CONTENTS

LIST OF FIGURES

LIST OF TABLES

ACKNOWLEDGEMENTS

I would like to express my greatest gratitude to my advisor, Prof. Vassilis Angelopoulos, without whom I would not have been able to complete this research. I still remember the equations he wrote on the white board when I discussed with him on research for the first time. It was on this white board and through countless hours of helpful discussions that he taught me independent thinking and guided me along my journey of colorful graduate student life. Not only did his profound knowledge and innovative ideas benefited me a lot, but his patience and encouragement also helped me though frustrations. He has been very supportive when I came across difficulties and I would not have been able to make it without his priceless trust. It is my great privilege to have his mentorship during this journey.

I would like to extend my sincere thanks to Dr Anton Artemyev for many fruitful scientific discussions. I can always learn a lot from his solid foundations in math and physics and extensive reading in academic literature. I am also grateful to Dr Xiaojia Zhang for knowledge in ECH waves and introducing me various powerful codes. I must also thank Dr Jiang Liu for his dipolarization front event list and for our discussions on DFs. I would also like to thank to Professor Philip Pritchett for his suggestions on my first research work, Professor Yu Lin for helpful discussions on kinetic Alfvén waves, Dr Terry Zixu Liu for guidance on data analysis software and for being a good example, Dr Xin An for helpful discussions on wave-particle interactions. I really appreciate Professor Marco Velli, Professor Jacob Bortnik and Dr Robert Strangeway for their valuable suggestions as my committee members. I would also like to express my gratitude to many faculty members in UCLA (Vassilis Angelopoulos, Marco Velli, Larry Lyons, Jacob Bortnik, George Morales, etc), from whose courses I learned a lot.

I acknowledge NASA contract NAS5-02099 for financial support and for the use of data from the THEMIS mission. I thank J.W. Bonnell and F.S. Mozer for the use of EFI data; C. W. Carlson and J. P. McFadden for use of ESA data; D. Larson and R.P. Lin for use of SST data; A. Roux and O. Le Contel for use of SCM data. I thank K. H. Glassmeier, U. Auster and W. Baumjohann for the use of FGM data provided under the lead of the Technical University of Braunschweig and with financial support through the German Ministry for Economy and Technology and the German Center for Aviation and Space (DLR) under contract 50 OC 0302. I am very grateful to Judy Hohl, who helped me a lot in improving my scientific writing skills.

I would like to express my sincere gratitude to my friends, Yingdong Jia, San Lu, Chen Shi, Zixu Liu, Yun Long, Yi Zuo, Yuqin Yang, Dongwu Wang, Yongyong Feng and etc for all the laughters and joys.

To my parents. Words cannot express my gratitude.

VITA

2010-2014	Bachelor of Science in Space Physics School of Earth and Space Sciences, Peking University
2014-2021	Graduate Student Researcher Department of Earth, Planetary and Space Sciences University of California, Los Angeles

PUBLICATIONS

Zhang, X., V. Angelopoulos, P. L. Pritchett, and J. Liu (2017), Off-equatorial current-driven instabilities ahead of approaching dipolarization fronts, J. Geophys. Res. Space Physics, 122, 5247–5260, doi: 10.1002/2016JA023421.

Zhang, X., Angelopoulos, V., Artemyev, A. V., & Liu, J. (2018). Whistler and electron firehose instability control of electron distributions in and around depolarizing flux bundles. Geophysical Research Letters, 45, 9380–9389. doi: /10.1029/2018GL079613

Zhang, X., Angelopoulos, V., Artemyev, A. V., & Liu, J. (2019). Energy transport by whistler waves around dipolarizing flux bundles. Geophysical Research Letters, 46. https://doi.org/10.1029/2019GL084226

Zhang, X., Angelopoulos, V., Artemyev, A. V., Zhang, X.-J., & Liu, J. (2021). Beam-driven electron cyclotron harmonic waves in Earth's magnetotail. Journal of Geophysical Research: Space Physics, 126, e2020JA028743. doi: 10.1029/2020JA028743

Zhang, X., Angelopoulos, V., Artemyev, A. V., & Zhang, X.-J. (2021). Beam-driven electron cyclotron harmonic waves: a parametric study, Physics of Plasma, under review

Chapter 1

Introduction

1.1 Plasma Waves in Earth's Magnetosphere

When the solar wind arrives at Earth, Earth's dipolar magnetic field interacts with it and forms the magnetosphere, with compressed magnetic field in the dayside and stretched magnetic field in the nightside. A schematic of Earth's magnetosphere is shown in Figure 1.1. The nightside of Earth's magnetosphere with stretched magnetic field lines and charged particles is referred to as the magnetotail, with a size of tens of Re (earth radii) in west-east direction and more than 200Re in anti-sunward direction. Open magnetic field lines with one foot on the ionosphere constitute the northern and southern lobes of the magnetotail; lobe plasma has very low density and temperature. The plasma sheet lies in regions between the northern and southern lobes; it consists of closed magnetic field lines with both feet on the ionosphere and hot (~keV), dense ($\sim 0.1 cm^{-3}$) plasma. The magnetotail is a key element of Earth's magnetosphere with dynamic environments and explosive activities. Magnetic reconnection in the plasma sheet, a process by which the magnetic energy stored in lobes is converted to bulk plasma acceleration and collisionless heating, is closely related to substorms and has a significant impact both to the ionosphere and the inner magnetosphere. The magnetotail, therefore, is of major interest for space studies and the specific region of study in this dissertation.

Various plasma waves exist in Earth's magnetotail. Figure 1.2 shows the electric field power spectral density observed on CRRES during one Earth orbit with apogee (the longest portion of the data shown) in the magnetotail [Meredith et al., 2004]. Several plasma waves are identified and demonstrated in this survey plot. Whistler mode chorus wave is an electromagnetic emission in the frequency range between $0.1f_{ce}$ and $0.8f_{ce}$ with a frequency gap at $0.5f_{ce}$ (f_{ce} is electron cyclotron frequency) [Tsurutani and Smith, 1974]. Both upper band and lower band chorus waves consist of discrete elements of rising or falling tones in the spectrogram [Santolik., 2003]. These electromagnetic emissions are usually generated near the magnetic equator through cyclotron resonance with energetic electrons (tens of keV) injected from the plasma sheet [Li et al., 2009b]. In the radiation belt, chorus waves play an important role in the acceleration process by accelerating electrons to relativistic energy range [Thorne et al., 2013] and the loss process by scattering electrons into loss cones [Thorne et al., 2010]. Plasmaspheric hiss is a broadband, structureless whistler mode wave which is often observed in Earth's plasmasphere or plasmaspheric plumes [Thorne et al., 1973]. The generation mechanism of plasmaspheric hiss remains an active area of research: they can be generated by lightning-generated whistler waves [Sonwalkar and Inan, 1989] but most recently shown to be driven primarily from chorus emissions outside the plasmapause [Bortnik et al., 2008]. Plasmaspheric hiss is very effective in scattering radiation belt electrons into the loss cone, responsible for the formation of the slot region between the inner and outer radiation belt [Lyons et al., 1972]. ECH (electron cyclotron harmonic) waves are electrostatic emissions in the frequency range between $\mathrm{n}f_{ce}$ (electron cyclotron frequency) to $(n+1)f_{ce}$ with the strongest wave power in the first harmonic frequency band [Kennel et al., 1970]. Previous theoretical work demonstrated that ECH waves can be excited by the loss-cone instability of hot plasma sheet electrons in the presence of a cold electron component [Ashour-Abdalla and Kennel, 1978; Ashour-Abdalla et al., 1979]. Because both whistler waves and ECH waves are capable of resonating with electrons over the energy range from hundreds of eV to tens of keV, the relative importance of whistler waves and ECH waves in scattering plasma sheet electrons and driving diffuse aurora has been controversial over decades [Ni et al., 2011b, 2011c]. Nowadays, it is generally accepted that ECH waves play an important role in scattering plasma sheet electrons into the loss cone and driving diffuse aurora in the outer magnetosphere beyond 8Re [Zhang et al., 2015].

1.2 Electron dynamics near dipolarization fronts

Various activities occur in the Earth's magnetotail with different temporal and spatial scales and bursty bulk flows (BBFs) are one of these activities with a temporal scale of 10-15 minutes and a spatial scale of several Res in azimuthal direction. Bursty bulk flows are plasma flows in the central plasma sheet with high speed (hundreds of km/s) and predominantly earthward direction [Baumjohann et al., 1990; Angelopoulos et al., 1992, 1994]. Although BBFs last only 10%-15% of the satellite observation time in the plasma sheet, they are responsible for 60%-100% of the earthward transport of mass, energy and magnetic flux [Angelopoulos et al., 1994]. These fast plasma sheet flows are originated from reconnection at 20-30 Re [Angelopoulos et al., 2008, 2013], or from interchange instabilities [Pritchett and Coroniti, 1998, 2010]. Embedded in these flows are magnetic flux tubes with magnetic field more dipolar than the magnetic field in the ambient plasma sheet [Nakamura et al., 2002; Ohtani et al., 2004]. These dipolarized flux tubes can be described as plasma bubbles with much lower plasma entropy ($pV^{5/3}$, p is the plasma pressure and V is the flux tube volume) than their surroundings [Chen and Wolf, 1993] and are later termed as diploarizing flux bundles in Liu et al. [2013a]. The leading edge of DFBs is characterized by a sharp increase in the B_z magnetic field (south-north component of the magnetic field in GSM coordinate), referred to as "dipolarization fronts", and are usually preceded by a small decrease in

B_z [Runov et al., 2009, 2011]. Figure 1.3 from Runov et al. [2009] demonstrates THEMIS observations of earthward propagation of dipolarization fronts from 20Re to 11Re. Dipolarizing flux bundles are often associated with enhancement of the electric field in dusk-dawn direction ($+Y_{GSM}$ direction) and therefore are major contributors to the earthward transport of magnetic flux in near-Earth plasma sheet [Liu et al., 2014]. The cross-tail currents inside dipolarizing flux bundles are reduced and diverted along magnetic field lines [Liu et al., 2013a]. A complex field-aligned current system is formed ahead of and inside dipolarzing flux bundles and these field-aligned currents might be related to the substorm current wedge which has a much larger spatial scale and a much longer time scale [Liu et al., 2015].

Dipolarizing flux bundles play an important role in regulating magnetotail dynamics not only because they provide the dominant earthward transport of magnetic flux, but also because they energize particles and then transport them towards the inner magnetosphere [Birn et al., 2014; Runov et al., 2015]. To understand particle dynamics, especially electron dynamics, inside dipolarizing flux bundles, we would like to first introduce the three adiabatic invariants related to particles' motions [Northrop, 1963]. The first adiabatic invariant is the magnetic moment of a particle gyrating around the magnetic field line and is defined as $\mu = mv_\perp^2/2B$, where $v_\perp$ is the particle velocity in the direction perpendicular to the magnetic field and B is the magnetic field strength. The second adiabatic invariant is related to a particle's bounce motion between mirror points of the magnetic field line and is defined as $J = \int_a^b p_\parallel ds$, where a and b are two mirror points of particle's bounce motion and $p_\parallel$ is particle's moment in parallel direction. The third adiabatic invariant is the magnetic flux enclosed by the particle's drift path around the magnetic dipole.

Because the gyration period and the gyroradius of plasma sheet electrons are very small compared to temporal and spatial scales associated with dipolarizing flux bundles, the first adiabatic invariant should be conserved during the electrons' interaction with them. Figure 1.4 from Birn et al. [2013] shows the trajectory of equatorially mirroring electrons projected to the magnetic equator during their interaction with earthward propagating flow bursts and dipolarization fronts. When an Electron's first adiabatic invariant is conserved, the equation of motion of its guiding center can be expressed as:

$$\frac{dW_{\perp}}{dt} = \mu\frac{dB}{dt} = \mu\frac{\partial B}{\partial t} + q\boldsymbol{E} \cdot \boldsymbol{V_{drift}} \tag{1.1}$$

where $W_{\perp}$ is electron's perpendicular energy, μ is the first adiabatic invariant, **E** is the electric field associated with dipolarizing flux bundles and $\boldsymbol{V_{drift}}$ is electron's guiding center drift velocity. The first term on the right-hand side of Eq (1.1) is electron energization from the temporal change of the magnetic field and the second term is the electron drift in the electric field that is related to the motion of nearby dipolarizing flux bundles and the diversion of the pre-existing plasma sheet plasma around them. This electron energization process illustrated by Figure 1.4 is betatron acceleration caused by the compression of the magnetic field and it has also been extensively discussed in Gabrielse et al. [2016]. While betatron acceleration process accounts for electron energization in perpendicular direction, fermi acceleration process leads to electron energization in parallel direction [Fu et al., 2011]. If the second adiabatic invariant is also conserved during the interaction with dipolarizing flux bundles (if the time-scales of the interaction in the plasma frame are longer than electron bounce-times to the ionosphere, a few seconds), electrons will be energized by fermi acceleration caused by the shortening of flux tube during earthward propagation. Adiabatic acceleration processes, including betatron and fermi acceleration, have been suggested as a major mechanism for particle acceleration in DFBs. The effects of non-adiabatic processes on particle dynamics near dipolarization fronts are not well understood. Therefore, this dissertation will mainly focus on the non-adiabatic wave-particle interaction process near dipolarization fronts.

1.3 Wave-particle interaction

In 1946, Landau described the oscillation of electrostatic waves in a collisionless plasma and demonstrated that electrostatic waves would eventually be damped if the collisionless plasma has a Maxwellian distribution function. The interaction between collisionless plasma and electrostatic waves can be described by the Vlasov equation:

$$\frac{\partial f_1}{\partial t} - \boldsymbol{v} \cdot \boldsymbol{\nabla} f_1 + q\boldsymbol{E_1} \cdot \frac{\partial f_0}{\partial \boldsymbol{v}} = 0 \tag{1.2}$$

where f_0 is the unperturbed term of particle's distribution function and f_1 is the perturbed term of the distribution function, $\boldsymbol{E_1}$ is the wave electric field. The mathematical effort of trying to solve this equation involves an integral in the complex plane of velocity $\boldsymbol{v}$ where the integration path is along the real axis encircling the singularity at ω/k. With pure mathematical derivation, the astounding result obtained by Landau demonstrated that energy transfer can occur between waves and particles in a system of a collisionless plasma. This damping mechanism is known as Landau damping and the physical meaning underlying the solution is profound. The damping of the electrostatic wave by electrons with Maxwellian distribution is only related to electrons traveling at a velocity equal to the phase velocity of the wave. In the frame moving at the velocity of wave phase speed, electrons will sense a static wave electric field. When the electron's velocity is slightly smaller than wave phase speed, it will be trapped in the potential well of wave electric field and eventually move at the wave phase speed during the resonant interaction. Therefore, the electron will gain energy from the wave. When the electron's velocity is slightly larger than the wave phase speed, it will lose energy to wave. Because there are more electrons with $v < \omega/k$ than electrons with $v > \omega/k$ in a Maxwellian distribution, the net result is that energy is transferred from electrons to waves and waves are damped.

Now we consider the situation where particles interact with an arbitrary type of plasma waves in a magnetized plasma. The resonance condition is expressed as the equation below:

$$\omega - k_\parallel v_\parallel = \frac{n\Omega_c}{\gamma}\ , \mathrm{n} = 0, \pm 1, \pm 2\ ... \tag{1.3}$$

where ω is the wave frequency, $k_\parallel$ is the wave vector in the direction parallel to the magnetic field, Ω_c is the cyclotron frequency of the particle, and $\gamma = (1 - v^2/c^2)^{1/2}$ is the relativistic factor. When the Doppler-shifted frequency of the wave matches the gyrofrequency of the particle, the first adiabatic invariant is no longer conserved (the time-scale of significant variations associated with the wave match that of the particle gyration, violating the assumption of adiabatic invariance) and particles are capable of exchanging energy with the waves effectively. When *n* is 0, Eq (1.3) describes the resonance condition for Landau resonance when the particle's parallel velocity equals to the wave's parallel phase velocity. Whether particles are accelerated or decelerated by the wave electric field in parallel direction ($E_\parallel$) through Landau resonance depends on the sign of the phase space density slope in the parallel direction ($\partial f/\partial v_\parallel\,|_{v=\omega/k}$). When *n* is not 0, particles resonate with plasma waves through cyclotron resonance. In the frame moving at the parallel velocity of the resonating particle, the wave frequency is Doppler-shifted to match the gyrofrequency of the particle. The wave perpendicular electric field ($E_\perp$) after Doppler-shifting will be circling around the background magnetic field line at the same angular velocity and in the same direction with respect to the gyrating particles. Therefore, these particles are capable of interacting with the waves effectively, leading to wave growth or damping and diffusion in energy and pitch angle in phase space.

To better understand wave-particle interaction which leads to wave growth or wave damping, we use the concept of "diffusion curve" or "resonance curve" [Gendrin, 1968, 1981; Summers et al., 1998]. When electromagnetic waves propagate in the direction parallel to the background magnetic field, a particle's motion is governed by the wave electric field and the Lorentz force from both background magnetic field and wave magnetic field. In the frame moving at the wave phase velocity $\omega/k_\parallel$, the wave electric field will vanish and the particles' energy is conserved since they only sense the Lorentz force. After moving back to the laboratory frame, we obtain the equation which defines the diffusion curve:

$$v_\perp dv_\perp + (v_\parallel - \omega/k_\parallel)dv_\parallel = 0 \tag{1.4}$$

where $v_\perp$ and $v_\parallel$ are particle's velocity in the perpendicular and parallel direction. We can easily determine whether this results in wave growth or wave damping from the relative positions of diffusion curve, constant energy curve and constant phase space density curve in velocity space. This is illustrated in Figure 1.5. Since the particles' energy is conserved in the frame moving at the wave phase speed, particles are confined to move along the diffusion curve when interacting with waves. They will diffuse in both directions along the diffusion curve and the net result is directed toward the lower phase space density. If this direction is towards larger particle energy, then energy will be transferred from waves to particles as illustrated in Figure 1.5(a). If this direction is towards smaller particle energy, then energy will be transferred from particles to waves as illustrated in Figure 1.5(b). Eq (1.4), the definition of diffusion curve, is only valid under the circumstances that particles interact with plasma waves through cyclotron resonance. Considering plasma waves with parallel wave electric field ($E_{\parallel}$), wave electric field does not disappear in the frame moving at wave phase velocity and particles' energy is not conserved. When particles interact with waves through Landau resonance, Eq (1.4) is no longer valid and the "resonance curve" or "diffusion curve" is $v_{\perp} = constant$. The energy exchange between particles and waves only happens in the parallel direction and particles' perpendicular energy is conserved for Landau resonance. The physical meanings underlying the wave-particle interaction can help us better understand electrons' non-adiabatic behaviors during interaction with waves in DFBs.

1.4 Whistler wave

Assuming a spatially homogeneous plasma with uniform background magnetic field and zero temperature of electrons and ions, we obtain the full dispersion relation of plasma waves in cold plasma approximation [Stix, 1962]:

$$\begin{bmatrix} S - n^2cos^2\theta & iD & n^2sin\theta cos\theta \\ -iD & S - n^2 & 0 \\ n^2sin\theta cos\theta & 0 & P - n^2sin^2\theta \end{bmatrix} \begin{bmatrix} E_x \\ E_y \\ E_z \end{bmatrix} = 0 \tag{1.5}$$

where n is refractive index ($n = ck/\omega$), $S = (R + L)/2$, $D = (R - L)/2$ and R, L, P are defined as:

$$R = 1 - \sum_j \frac{\omega_{pj}^2}{\omega} \frac{1}{\omega + \Omega_{cj}}, L = 1 - \sum_j \frac{\omega_{pj}^2}{\omega} \frac{1}{\omega - \Omega_{cj}}, P = \sum_j \frac{\omega_{pj}^2}{\omega^2} \tag{1.6}$$

ω_{pj} is the plasma frequency of species j and Ω_{cj} is the cyclotron frequency of species j

Considering a parallel propagating wave when $\theta = 0$, we obtain two solutions with $n^2 = R$ and $n^2 = L$. $n^2 = R$ is the solution for right-handed polarization mode with $E_y/E_x = -i$. Whistler mode wave, which belongs to that mode, is electromagnetic wave in the frequency range between lower-hybrid frequency ($\Omega_{LH} \approx \sqrt{\Omega_{ce}\Omega_{ci}}$) and electron cyclotron frequency (Ω_{ce}) [Helliwell, 1965]. Whistler mode waves have been observed both in the inner magnetosphere [Russell et al., 1969; Tsurutani and Smith, 1974] and in the magnetotail [Gurnett et al., 1976; Zhang et al., 1999]. Most of whistler mode waves are confined near magnetic equator [Meredith et al., 2003; Li et al., 2009b] but they are also observed at higher magnetic latitude [Agapitov et al. 2013]. The propagation directions of whistler mode waves are found to be both in the parallel direction [Burton and Holzer, 1974; Hayakawa et al., 1984] and in very oblique propagation direction [Li et al., 2013; Agapitov et al., 2014]. Whistler wave intensity is dependent on geomagnetic activity and is related to the injection of energetic electrons from plasma sheet [Li et al., 2008, 2009b].

Whistler mode waves are generally thought to be driven unstable by electrons at energy range from a few keV to tens of keV with perpendicular temperature anisotropies ($T_\perp/T_\parallel > 1$, $T_\perp$ is the electron temperature in perpendicular direction and $T_\parallel$ is the electron temperature in parallel direction) [Kennel and Petscheck 1966; Helliwell 1967; Santolik et al., 2010a; Omura and Nunn, 2011]. Assuming parallel propagating whistler waves and cold plasma, Kennel and Petscheck [1966] calculated the growth rate for whistler mode waves:

$$\gamma = \pi\Omega_{ce}\left(1-\frac{\omega}{\Omega_{ce}}\right)^2 \eta^-(v_R)\cdot\{A^-(v_R)-\frac{1}{\Omega_{ce}/\omega-1}\} \tag{1.7}$$

where v_R is the resonance velocity defined as $v_R = (\omega - \Omega_{ce})/k_\parallel$.

$\eta^-(v_R)$ can be roughly interpreted as the fraction of electrons that are in cyclotron resonance with whistler waves:

$$\eta^-(v_R) = 2\pi\frac{\Omega_{ce}-\omega}{k}\cdot\int_0^\infty f(v_\perp, v_\parallel = v_R)v_\perp dv_\perp \tag{1.8}$$

$A^-(v_R)$ describes the pitch angle anisotropy and is defined as

$$A^-(v_R) = \left.\frac{\int_0^\infty v_\perp dv_\perp(v_\parallel\frac{\partial f}{\partial v_\perp} - v_\perp\frac{\partial f}{\partial v_\parallel})\frac{v_\perp}{v_\parallel}}{2\int_0^\infty f v_\perp dv_\perp}\right|_{v_\parallel = v_R} \tag{1.9}$$

The whistler mode wave is unstable when the anisotropy of resonating electrons is sufficiently large ($A^- > \frac{1}{\Omega_{ce}/\omega-1}$). The growth rate of the whistler wave is determined by both the fraction of resonating electrons and the pitch angle anisotropy. Figure 1.6 provides further understanding of whistler wave excitation by anisotropic electron population through cyclotron resonance. Using an electron distribution function with $n_e = 1cm^{-3}$, $T_e = 1keV$, $T_\perp/T_\parallel = 3$ as input parameters, we solved the hot plasma dispersion relation and found that the whistler mode wave is most unstable when $\omega/\omega_{ce} = 0.55$ and $k\rho_e = 0.39$. When whistler mode waves propagate in the antiparallel direction, the phase velocity of the wave and the electron's resonance velocity are in opposite directions (resonance velocity is calculated from $v_R = (\omega - |\Omega_{ce}|)/k_\parallel$). The diffusion curve (shown as the sold magenta line in Figure 1.6) can be obtained from Eq (1.4). Constant phase space density curve for electron distribution with sufficiently large pitch angle anisotropy is illustrated as solid black line in Figure 1.6. Electrons will diffuse in the direction towards lower phase space density (indicated by the magenta arrow in Figure 1.6), leading to the decrease of electron energy and wave gain.

Whistler waves have received substantial attention because they play an important role in accelerating and scattering electrons [Horne and Thorne 1998, 2003; Bortnik and Thorne, 2007; Thorne et al., 2010, 2013]. They have been considered to contribute significantly to electron scattering to produce diffuse and pulsating aurora [Nishimura et al., 2010; Ni et al., 2011b]. Furthermore, whistler waves act to reduce electron temperature anisotropies through pitch angle scattering and limit the anisotropies near marginal instability thresholds [Gary & Wang, 1996; Gary et al., 2000]. In the inner magnetosphere, whistler mode chorus waves can resonate with electrons at energies of a few hundred keV effectively and accelerate them to relativistic energy range (several MeV) [Summers et al., 2002; Horne and Thorne 2003; Li et al., 2014]. Being effective in regulating electron dynamics by scattering and accelerating electrons, whistler mode wave is one of our major interests in this dissertation.

1.5 Electron cyclotron harmonic wave

ECH (electron cyclotron harmonic) wave is an electrostatic emission in the frequency range between nf_{ce} (electron cyclotron frequency) to $(n+1)f_{ce}$ with the strongest wave power in the first harmonic frequency band [Fredricks and Scarf, 1973; Roeder and Koons, 1989; Meredith et al., 2009]. ECH waves were first observed by OGO 5 satellite with wave power centered around

$(n+1/2)f_{ce}$ and therefore are known as “n+1/2” waves [Kennel et al., 1970]. These electrostatic emissions have been observed over a large range of radial distances with L=4-12, both in the inner magnetosphere [Meredith et al., 2009; Ni et al., 2011a, 2017] and in the magnetotail [Liang et al., 2011; Zhang et al., 2014]. Statistical studies on the global distribution of ECH waves have previously demonstrated that these waves are typically confined to within a few degrees to the magnetic equator and are most frequently observed in the night and dawn sector with 2100-0600 MLT (magnetic local time) [Roeder and Koons, 1989; Meredith et al., 2009; Ni et al., 2017]. ECH waves exist under various geomagnetic activity levels, but they intensify for active geomagnetic conditions [Ni et al., 2011a]. Zhang and Angelopoulos [2014] demonstrated that more than 70% of ECH waves in the magnetotail are correlated with energetic electron injections and more than 50% of them are correlated with dipolarization fronts. Upon arrival of dipolarizing flux bundles, high-amplitude ECH waves excited near the magnetic equator tend to propagate to higher latitudes due to the increase in curvature radius, resulting in ECH wave intensification [Zhang et al., 2014].

Previous theoretical work has attributed ECH wave excitation to loss-cone instability of hot plasma sheet electrons in the presence of a cold electron component [Young et al., 1973; Karpman et al., 1975; Ashour-Abdalla and Kennel, 1978; Ashour-Abdalla et al., 1979]. The electron loss cone distribution function which provides the free energy source for ECH wave generation has a positive slope in perpendicular direction in the velocity space where $\partial f/\partial v_\perp > 0$. Abdalla and Kennel [1978] represented the hot electron distribution function by a subtracted bi-maxwellian distribution function:

$$f(v_\perp, v_\parallel) = \sum_i f_i = \sum_i \frac{n_i}{\pi^{2/3}\alpha_{\perp i}^2 \alpha_{\parallel i}} \exp\left(-\left(\frac{v_\parallel - v_{di}}{\alpha_{\parallel i}}\right)^2\right)$$

$$\cdot\left[\Delta_i \exp\left(-\frac{v_\perp^2}{\alpha_{\perp i}^2}\right)+\frac{(1-\Delta_i)}{(1-\beta_i)}\cdot\left(\exp\left(-\frac{v_\perp^2}{\alpha_{\perp i}^2}\right)-\exp\left(-\frac{v_\perp^2}{\beta_i\alpha_{\perp i}^2}\right)\right)\right] \tag{1.100}$$

where the subscript *i* denotes the *i*th component of the electron distribution function, n_i is the electron number density, $\alpha_{\parallel i}$ and $\alpha_{\perp i}$ are the thermal velocity of electrons in the parallel and perpendicular direction, Δ_i and β_i are the depth and size of the loss cone. By assuming an unstable loss cone distribution and solving the hot plasma dispersion relation, Ashour-Abdalla and Kennel [1978] demonstrated that ECH waves are unstable when the density and temperature ratios between cold and hot electrons are small enough. Using the unstable electron loss cone distribution function in Table 1.1 as input parameters, we solved the hot plasma dispersion relation of ECH waves. The most unstable mode of ECH wave is at a wave normal angle of 85.5° and at $\omega/\omega_{ce} = 1.55$ and $k\rho_e = 8.5$ ($\omega_{ce} = 1.4kHz$ is the electron cyclotron frequency, ρ_e is the electron gyroradius of component 1 in Table 1.1). Figure 1.7 illustrates ECH wave generation in the velocity space of electron loss cone distributions. When analyzing the particle equation of motion for the non-relativistic case using a Hamiltonian approach during wave-particle interaction, we obtain that quantity C_n in Eq. (1.11) is a constant [Shklyar and Matsumoto, 2009]

$$C_n = nW - \mu\omega = \text{constant} \tag{1.11}$$

where W is the particle kinetic energy ($W = \frac{1}{2}m(v_\perp^2 + v_\parallel^2)$), μ is ($\frac{1}{2}mv_\perp^2)/\omega_{ce}$, ω is the wave frequency and *n* is the resonance harmonic number in Eq. (1.3). Electrons diffuse along the contour of Eq. (1.11) towards the direction of lower phase space density, indicated by the solid magenta arrow in Figure 1.7. Electrons, therefore, will lose energy and diffuse into the loss cone. Electron cyclotron harmonic waves driven by such a loss-cone distribution are usually unstable at very large (around $88^o \sim 89^o$) wave normal angles and heavily damped at smaller wave normal angles due to Landau and cyclotron resonance [Horne, 1989; Horne and Thorne, 2000; Horne et al., 2003; Ni et al., 2011b, 2012; Liu et al., 2018]. Because of the lack of electron distribution function measurements with sufficient angular resolution to reveal the properties of the loss cone (usually less than 1^o in the magnetotail) and of the cold electron population, such an excitation mechanism has never been proven directly.

Electron cyclotron harmonic waves have received substantial attention due to their potential roles in diffuse aurora precipitation. The diffuse aurora is a belt of weak emission which extends over a latitude range of 5^0 to 10^0 within the auroral oval and maps to the central plasma sheet [Newell et al., 2009]. The origin of diffuse aurora is related to the scattering of plasma sheet electrons in the energy range from hundreds of eV to tens of keV by plasma waves [Fontaine and Blanc, 1983]. Because both ECH waves and whistler waves are capable of resonating with electrons at this energy range and scattering them into loss cones, the relative importance of whistler waves and ECH waves in driving diffuse aurora has been controversial over decades [Kennel et al., 1970; Lyons, 1974; Belmont et al., 1983; Roeder and Koons, 1989; Horne and Thorne, 2000; Horne et al., 2003; Meredith et al., 2009]. Ni et al. [2012] quantified the pitch angle scattering rates of plasma sheet electrons by ECH waves and demonstrated that the scattering can approach strong diffusion limit. In Zhang et al. [2015], the authors modeled the energy flux of diffuse aurora precipitation from ionospheric observations and estimated the ECH wave induced precipitation based on wave properties observed by THEMIS. By comparing the ECH wave induced precipitation and diffuse aurora precipitation, Figure 1.8 demonstrated that ECH waves are the dominant driver for diffuse aurora precipitation in the outer magnetosphere beyond 8Re.

All of the above progress in understanding the potential roles of ECH waves in driving diffuse aurora is based on the assumption that ECH wave is excited by loss cone distributions. Despite the difficulty in validating this excitation mechanism through direct observations, there has been very little reconsideration of the free energy sources of ECH waves since the 1970s. This dissertation aims to explore alternative generation mechanisms of ECH waves.

1.6 Low frequency fluctuations

Recent 3D PIC (particle-in-cell) simulations in Pritchett et al. [2014] have found electromagnetic instabilities near ion cyclotron frequency and located away from the magnetic equator ahead of approaching dipolarization fronts. In simulations, the instabilities were driven by a parallel current carried by electrons. We identified such instabilities and analyzed their characteristics using THEMIS observations in Section 2 in this dissertation. One possible candidate for such instabilities is current-driven kink-like instability in Gary et al. [1976] and Perraut et al. [2000]. To better understand the current-driven kink-like instability, we consider the situation when ions are cold and electrons are drifting in the direction parallel to the magnetic field. The two dispersion relations D_+ and D_- when waves are in parallel directions can be written as:

$$D_+ = k^2c^2 - \omega^2 - \frac{1}{\sqrt{2}}\omega_{pe}^2\frac{\omega - kV_{d,e}}{kV_{\parallel,e}}Z(\xi_1) + \omega_{pi}^2\frac{\omega}{\omega + \omega_{ci}} = 0 \tag{1.12}$$

$$D_- = k^2c^2 - \omega^2 - \frac{1}{\sqrt{2}}\omega_{pe}^2\frac{\omega - kV_{d,e}}{kV_{\parallel,e}}Z(\xi_2) + \omega_{pi}^2\frac{\omega}{\omega - \omega_{ci}} = 0 \tag{1.13}$$

$Z(\xi)$ is the plasma dispersion function and arguments ξ_1 and ξ_2 are defined as:

$$\xi_1 = \frac{\omega - kV_{d,e} - |\omega_{ce}|}{\sqrt{2}kV_{\parallel,e}}, \xi_2 = \frac{\omega - kV_{d,e} + |\omega_{ce}|}{\sqrt{2}kV_{\parallel,e}}$$

where ω_{pe} and ω_{pi} are electron plasma frequency and ion plasma frequency, ω_{ce} and ω_{ci} are electron gyrofrequency and ion gyrofrequency, $V_{d,e}$ is the electron drift velocity in the direction parallel to the magnetic field and $V_{\parallel,e}$ is the electron parallel thermal velocity.

In the low frequency limit when $\omega \ll \omega_{ci}$, D_+ describes the dispersion relation for fast magnetosonic wave modified by electron currents and D_- describes the dispersion relation for shear Alfvén wave modified by electron currents. Since $|\xi_1|, |\xi_2| \ll 1$, $Z(\xi)$ is approximated by $-\frac{1}{\xi}$ for large arguments and dispersion relations D_+ and D_- are therefore written as:

$$D_+ = k^2c^2 - \omega^2 - \omega_{pe}^2 \frac{\omega - kV_{d,e}}{\omega - kV_{d,e} - |\omega_{ce}|} + \omega_{pi}^2 \frac{\omega}{\omega + \omega_{ci}} = 0 \tag{1.14}$$

$$D_- = k^2c^2 - \omega^2 - \omega_{pe}^2 \frac{\omega - kV_{d,e}}{\omega - kV_{d,e} + |\omega_{ce}|} + \omega_{pi}^2 \frac{\omega}{\omega - \omega_{ci}} = 0 \tag{1.15}$$

Further simplification of the dispersion relations leads to

$$D_+ = X^2 - X\left(K^2 + K\frac{V_d}{V_A}\right) - \left(K^2 + K\frac{V_d}{V_A}\right) = 0 \tag{1.16}$$

$$D_- = X^2 + X\left(K^2 - K\frac{V_d}{V_A}\right) - \left(K^2 - K\frac{V_d}{V_A}\right) = 0 \tag{1.17}$$

where V_A is the Alfvén velocity, X and K are normalized values defined as: $X = \omega/\omega_{ci}$; $K = kV_A/\omega_{ci}$.

Solutions of Eq (1.17) give rise to current-driven kink-like instability (Two solutions of Eq (1.17) are positive and negative wave frequency branches when there is no electron current. In the presence of electron currents, these two solutions merge to have the current-driven kink-like instability.). The current-driven kink-like instability is extensively investigated in Chapter 2 in this dissertation.

The other low frequency wave we would like to introduce here is kinetic Alfvén waves. Based on MHD (magnetohydrodynamic) equations, three MHD wave modes can be derived: Alfvén waves, fast magnetosonic waves and slow magnetosonic waves. The dispersion relation for Alfvén wave is written as:

$$\omega = k_{\parallel} V_A \tag{1.18}$$

where $V_A = B_0/\sqrt{\mu_0 n_i m_i}$ is the Alfvén velocity, B_0 is the background magnetic field and n_i is the ion number density. The wave electric field is perpendicular to background magnetic field based on frozen-in condition ($\boldsymbol{E_1} + \boldsymbol{u_1} \times \boldsymbol{B_0} = 0$, $\boldsymbol{E_1}$ is the perturbation in electric field and $\boldsymbol{u_1}$ is the perturbation in velocity). In MHD regime, Alfvén waves have no parallel wave electric field and they are unable to interact with electrons through Landau resonance. However, the situation can be quite different when we take finite wave length and finite wave frequency into considerations. Kinetic Alfvén waves (KAWs) are Alfvén waves when the perpendicular wavelength is comparable to the ion gyroradius and have received substantial attention since the early work in Hasegawa [1976]. Kinetic Alfvén waves have parallel wave electric field and the parallel electric field is balanced by electron pressure gradient. The dispersion relation is derived in Stasiewicz et al. [2000] and written as:

$$\omega = k_{\parallel} V_A \sqrt{1 + k_{\perp}^2(\rho_s^2 + \rho_i^2) - \frac{\omega^2}{\omega_{ci}^2}(1 + k_{\perp}^2 \rho_i^2)} \tag{1.19}$$

where ρ_i is the ion gyroradius and $\rho_s = \sqrt{T_e/m_i}/\omega_{ci}$ is the ion acoustic gyroradius. The ratio between wave electric field and wave magnetic field is written as:

$$\frac{E_{\perp}}{B_{\perp}} = V_A(1 + k_{\perp}^2 \rho_i^2)/\sqrt{1 + k_{\perp}^2(\rho_s^2 + \rho_i^2)} \tag{1.20}$$

where $E_{\perp}$ is the wave electric field in the perpendicular direction and $B_{\perp}$ is the wave magnetic field in the perpendicular direction. In the long wave length limit, the ratio between *E* and *B* is the local Alfvén velocity. When the wave number becomes larger, the ratio between *E* and *B* for kinetic Alfvén waves becomes much larger than the Alfvén speed. The generation of kinetic Alfvén waves remains an active area of study for decades. Hasegawa [1976] suggests that Kinetic Alfvén waves can be excited through mode conversion from the large scale MHD surface wave in a plasma where there is sharp gradient in Alfvén velocity.

The parallel wave electric field associated with kinetic Alfvén waves are capable of resonating with particles and energizing particles along the magnetic field lines. Therefore, kinetic Alfvén waves play an important role in electron and ion energization in ionosphere along auroral field lines [Hasegawa 1976; Chaston et al., 2000; Lysak and Song, 2003], in magnetotail [Wygant et al., 2002; Keiling, 2009] and in many other regions in Earth's magnetosphere [Artemyev et al., 2015]. Kinetic Alfvén waves have also been suggested to play important roles in global energy transport. Angelopoulos et al. [2002] demonstrated that the bursty bulk flow energy couples to Alfvén waves and is sufficient to account for the expected auroral energy deposition during substorms. Using

THEMIS observations, Chaston et al. [2012] demonstrated that kinetic Alfvén waves represent ~5% of the total energy transport in the bursty bulk flows on average. We will discuss kinetic Alfvén waves in Section 3.1 in this dissertation.

1.7 Motivation and objectives

Dipolarization fronts are transient phenomena in the magnetotail with various types of waves (for instance, whistler waves, ECH waves and kinetic Alfvén waves discussed earlier) observed in their vicinity. In the dynamic environments of dipolarization fronts, particles undergo complex motions and can easily form unstable distributions. The relations between these waves and unstable particle distributions, however, remain an open question. Waves near DFs are good tracers of particle free energy and the rapid reconfiguration of velocity space distributions related to DFs. Unstable particle distributions and disturbed plasma environments can form around DFBs and provide the free energy sources for wave generation. The free energy sources for different waves and how these free energy sources are related to DFBs are still not fully understood. Additionally, the effects of pitch angle scattering and non-adiabatic acceleration process on modifying particle distributions due to wave-particle interactions are quite important as they signify the energy transfer from waves to particles. Studying the relations between different waves and DFs could significantly improve our understanding of particle dynamics at the DFs and how the DFs would affect the global energy conversion patterns. Therefore, it is important to investigate the relations between waves and DFs, including the predominant waves near DFs, their generation mechanisms and the effects of these waves on regulating particle dynamics near DFs.

Our main objective of this study is to understand the relation between waves and dipolarization fronts. We aim to study different types of waves near DFs, their properties and the predominant waves near DFs. We propose to investigate how the waves are generated by unstable particle distributions related to the DFs. We would like to explore the potential effects of these waves on modifying particle distributions and affecting particle dynamics near DFs. We wish to improve our understanding of the particle dynamics in the magnetotail by not only considering adiabatic interaction, but also taking into account wave-particle interaction in future studies.

1.8 Organization of the dissertation

This dissertation is organized as follows:

In Chapter 2, we seek observational evidence for electromagnetic waves identified in PIC simulations in Pritchett et al. [2014]. Such waves are near ion gyrofrequency, located away from the magnetic equator and ahead of approaching dipolarization fronts. Using THEMIS observations, we found two instabilities, one at a frequency of 0.4 ω_{ci} and the other at a much lower frequency of 0.02 ω_{ci} (ω_{ci} is the ion cyclotron frequency). These low frequency fluctuations are excited by parallel electron currents and later confirmed to be current-driven ion cyclotron instability [Gary and Forslund, 1975] and current-driven kink-like instability respectively [Gary et al., 1976; Perraut et al., 2000]. Driven by parallel electron currents, these instabilities relax by reducing the current and have the potential to contribute to energy conversion near dipolarization fronts. This chapter is a version of Zhang et al. [2017].

In Chapter 3, we identified all whistler wave events near dipolarization fronts from year 2007 to 2017 to investigate the relations between whistler waves and dipolarization fronts. Adiabatic acceleration mechanisms (betatron and Fermi acceleration) should result in $T_{\perp,e}/T_{\parallel,e} > 1$ ($T_{\perp,e}/T_{\parallel,e} < 1$) due to magnetic field compression (shrinkage of a flux tube) [Fu et al., 2011; Birn et al. 2013]. Electron temperatures, however, are often observed to remain isotropic or weakly anisotropic throughout the magnetotail [Walsh et al., 2011; Artemyev et al., 2013]. In this chapter, we emphasize the importance of whistler waves in relaxing electron temperature anisotropies in the magnetotail. We found that electron temperature anisotropies are well-constrained by the marginal stability conditions of the whistler and oblique electron firehose instabilities. Driven by sufficiently large $T_{\perp,e}/T_{\parallel,e} > 1$ ($T_{\perp,e}/T_{\parallel,e} < 1$) near dipolarization fronts, whistler instabilities (electron firehose instabilities) are capable of resonating with electrons effectively and constraining electron temperature anisotropies near the marginal instability threshold of whistler instability (electron firehose instability) through pitch angle scattering process. This chapter is a version of Zhang et al., [2018].

In Chapter 4, we investigate whistler wave excitation within and around dipolarizing flux bundles (DFBs), critical energy transporters in the magnetotail, and the evacuation of perpendicular electron energy by whistler wave Poynting flux using the whistler wave event database established in the previous chapter. We demonstrated that perpendicular anisotropy of the suprathermal electron population (above 10keV) is the major free energy source for whistler wave generation near dipolarization fronts. When electrons are transported earthward by DFBs, 3.7% of the suprathermal electron energy flux will be directed away from the current sheet towards the ionosphere as electromagnetic energy of whistler waves. Chapter 4 is a version of Zhang et al., [2019]. Combining the results in Chapter 3 and Chapter 4, we conclude that whistler waves play an important role in constraining electron perpendicular temperature anisotropies through pitch-angle scattering process and in radiating energetic electron energy flux during the earthward transport process.

In Chapter 5, we identified all ECH waves near dipolarization fronts using 10 years of THEMIS observational data. Electron cyclotron harmonic waves are often correlated with electron injections and dipolarization fronts in the magnetotail and dipolarization fronts are important in driving and intensifying ECH waves [Zhang and Angelopoulos, 2014]. Therefore, we focus on ECH waves observed near DFs in this chapter. Previous theoretical work has long attributed the excitation of electron cyclotron harmonic (ECH) waves to the loss cone instability of hot electrons in the presence of a cold electron component [Ashour-Abdalla and Kennel, 1978; Ashour-Abdalla et al., 1979]. There has not been too much reconsideration of the free energy sources of ECH waves since then. In this chapter, we present both observational evidence and theoretical evidence on the generation mechanism of ECH waves by low energy electron beams. We found that more than 30% of the observed ECH waves behind DFs have moderately oblique (~70^0) wave normal angles, much smaller than the ~85^o expected from classical loss-cone instability. These moderately oblique ECH waves are related with enhancement with parallel electron flux in the subthermal energy range, suggesting that they are likely to be driven unstable by low energy electron beams. We solved the dispersion relation for ECH waves and demonstrated that moderately oblique ECH waves can indeed be driven unstable by low energy electron beams. This chapter is a version of Zhang et al., [2021].

In Chapter 6, we continue to investigate beam-driven ECH waves. Recent THEMIS observations in the previous chapter indicate that ECH waves can be excited by low energy electron beams in Earth’s magnetotail. The ambient and beam plasma conditions under which electron beam excitation can take place are unknown. Knowledge of such conditions would allow us to further explore the relative contribution of this excitation mechanism to ECH wave scattering of magnetospheric electrons at Earth and the outer planets. Using the hot plasma dispersion relation, we address the nature of beam-driven ECH waves and conduct a comprehensive parametric survey of this instability. Our instability analysis demonstrated that the positive growth rates of beam-driven ECH waves are contributed from cyclotron resonance at the first order and at higher orders. We conducted a parametric study to investigate the electron beam characteristics and ambient plasma environments that favor the generation of beam-driven ECH waves. We found that beam-driven ECH waves were unstable under a wide range of plasma conditions. Combining the results in Chapter 5 and Chapter 6, we provide both observational and theoretical evidence of the generation mechanism of ECH waves by electron beams.

Chapter 7 summarizes our results and discusses our future plans.

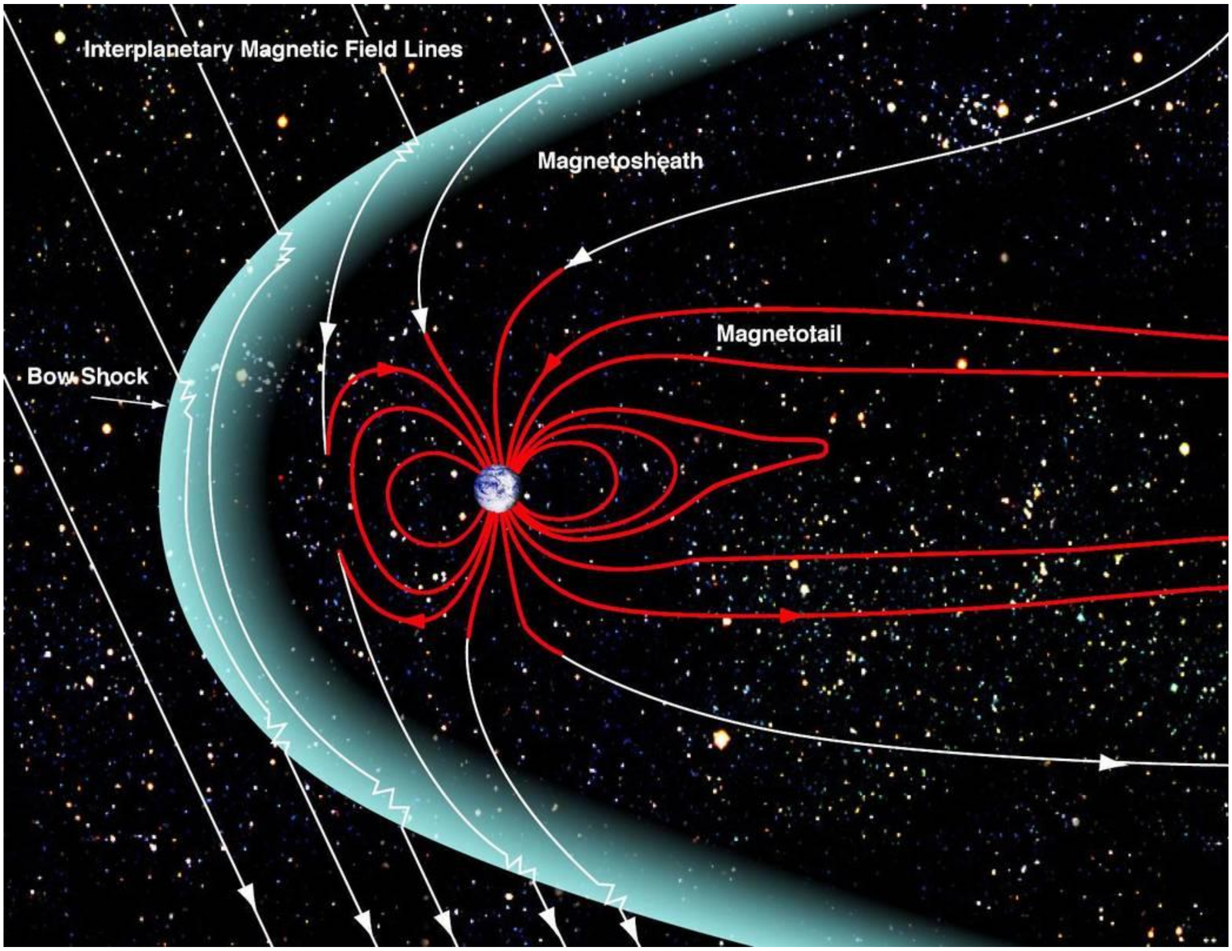

Figure 1.1: A schematic plot showing the structure of Earth’s magnetosphere (NASA website: *https://www.nasa.gov/mission_pages/sunearth/multimedia/magnetosphere.html*).

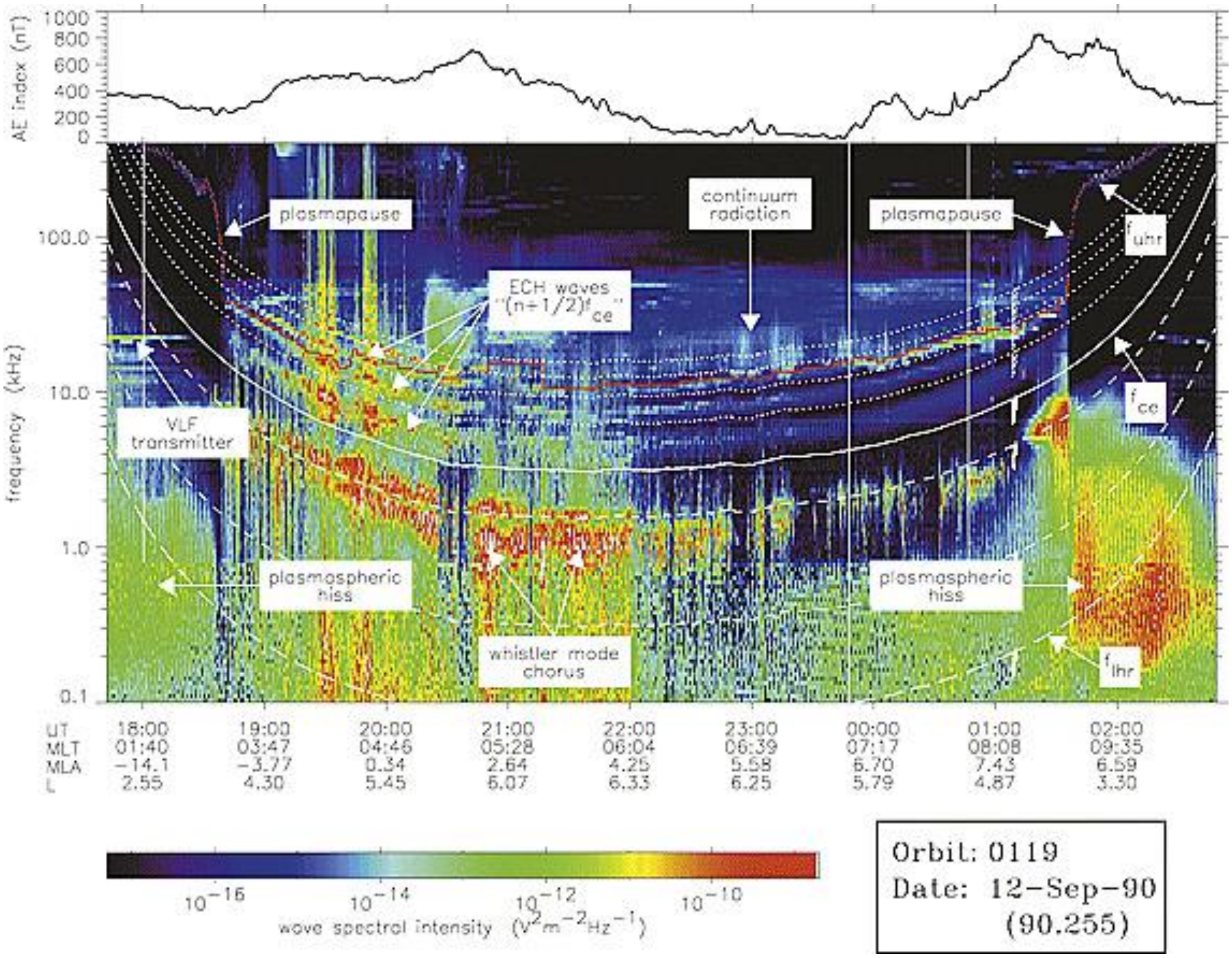

Figure 1.2: Survey plot of the wave spectral intensity observed on CRRES during one orbit. The solid white line represents the local electron gyrofrequency f_{ce}. Dashed lines from bottom to top represent the local lower hybrid resonance frequency f_{LHR}, $0.1f_{ce}$, and $0.5f_{ce}$. The first four harmonics of f_{ce} are represented by the dotted lines and the local upper hybrid resonance frequency f_{UHR} is shown in red (Figure adapted from Meredith et al. [2004])

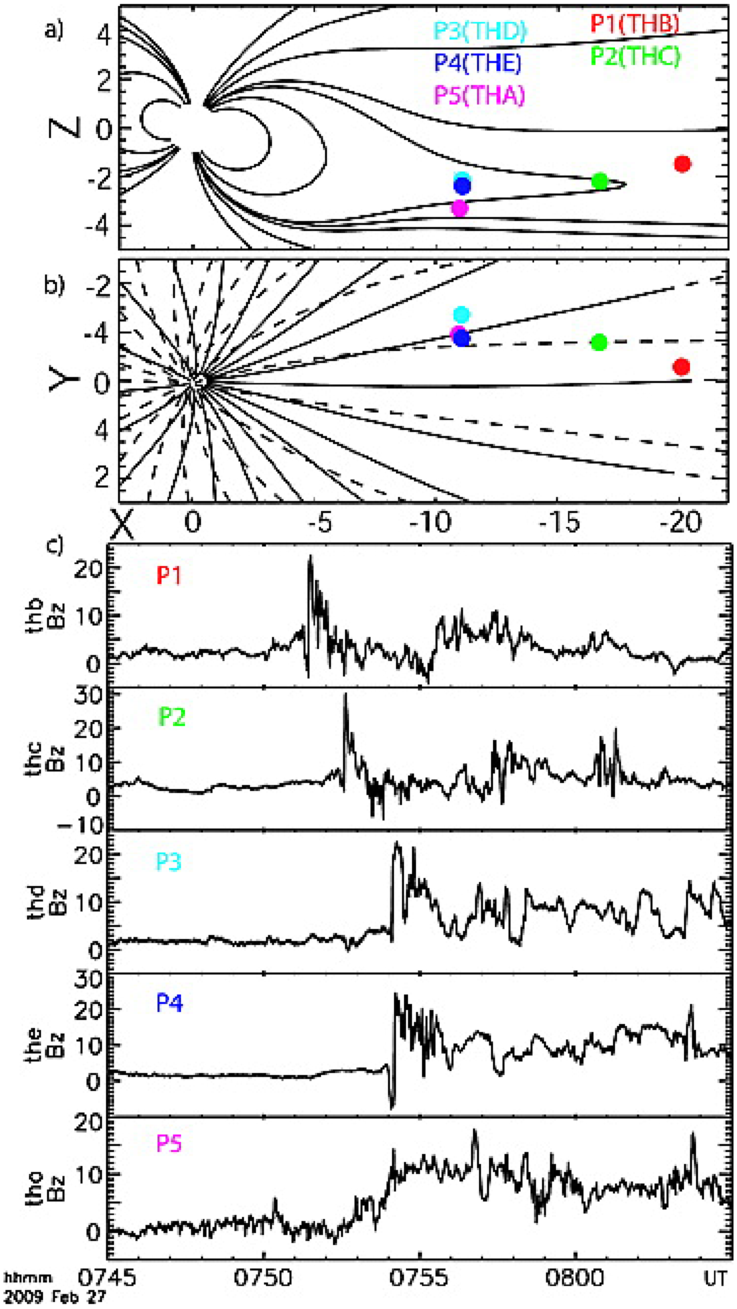

Figure 1.3: THEMIS SC positions in (a) XZ and (b) XZ GSM planes. T96-model magnetic field [Tsyganenko, 1995] is shown. (c) Time series of B_Z (GSM) at all five probes (P1–P5). (Figure adapted from Runov et al. [2009])

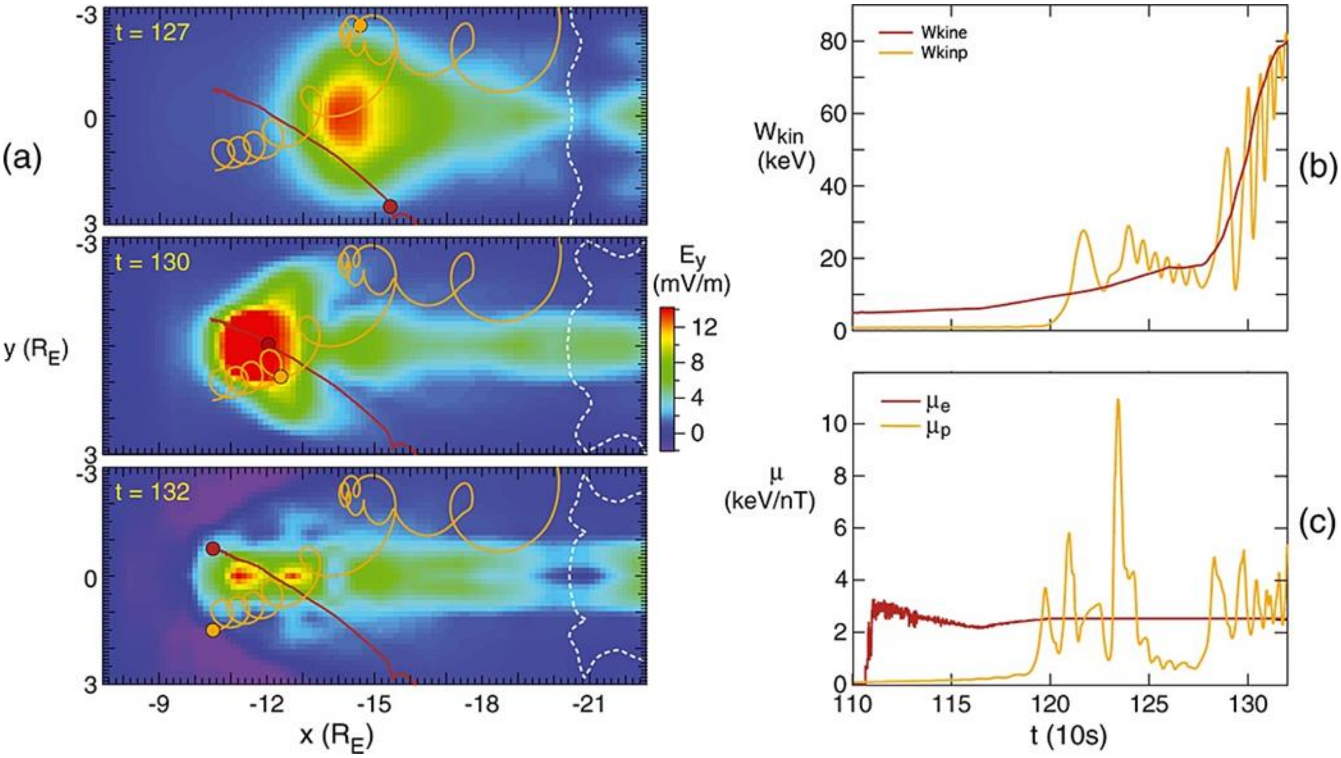

Figure 1.4: (a) Trajectories of a proton (orange) and electron (dark red), accelerated to a final energy of 83.5 keV, over laid on snapshots of the cross-tail electric field (color) in the equatorial plane. The instantaneous locations of protons and electrons are shown as orange and dark red dots, respectively. The white dashed contours show the instantaneous location of the near-Earth x-line (B_Z= 0). Temporal evolution of the (b) kinetic energy and of the (c) magnetic moment of the two particles (red: electron; orange: proton). (Figure adapted from Birn et al. [2013])

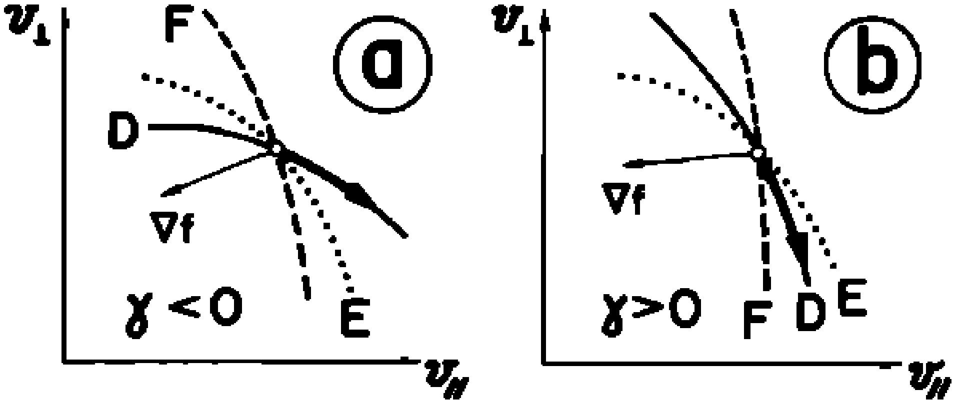

Figure 1.5: Curve D, E and F represent: diffusion curve in Eq (1.4); constant energy curve and constant phase space density curve. In Figures 1.5(a) and 1.5(b) the relative configurations of F and D are fixed, and they are such that the interaction leads to a decrease of the pitch angle. But the relative configuration of the diffusion curve D and the constant energy curve E is changed. In Figure 1.5(a) the medium is absorbing (because particles gain energy during the diffusion); in Figure 1.5(b) it is emitting. (Figure adapted from Gendrin [1981])

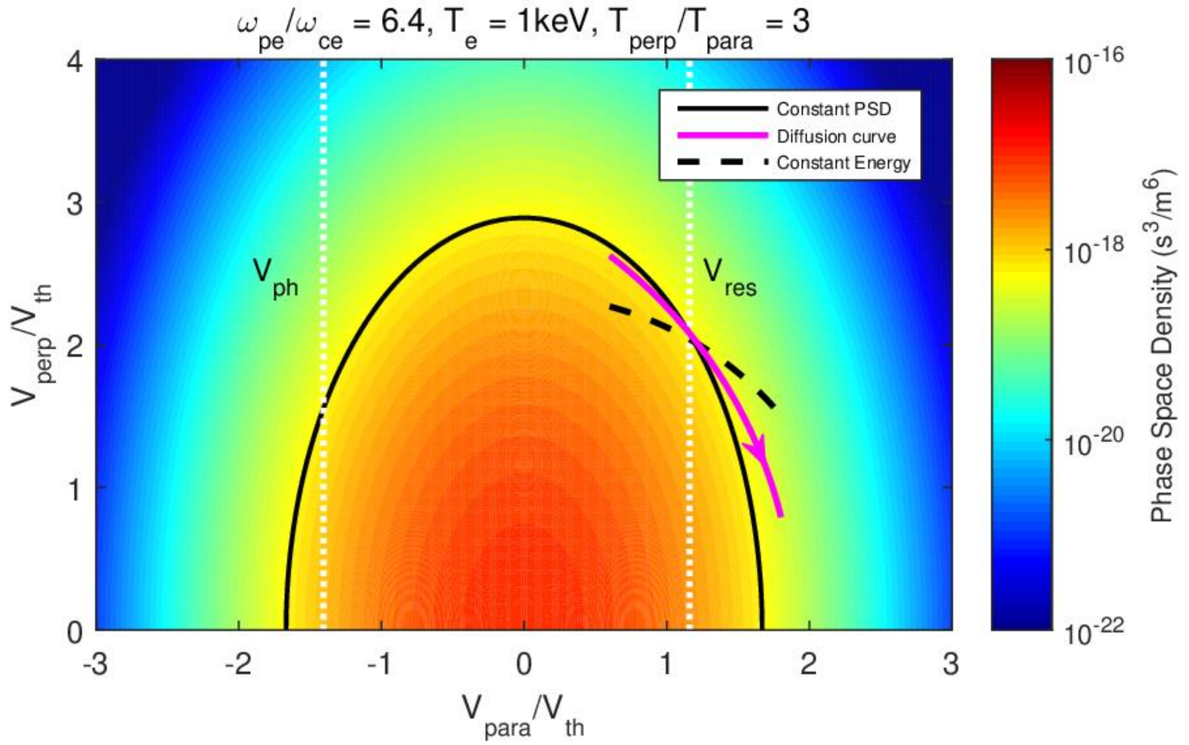

Figure 1.6: Distribution function for electrons when $n_e = 1cm^{-3}$, $T_e = 1keV$, $T_\perp/T_\parallel = 3$. Background magnetic field strength is 50nT. Whistler wave is most unstable when $\omega/\omega_{ce} = 0.55$ and $k\rho_e = 0.39$. Vertical white dashed line is the electron resonance velocity. Solid black line is the constant phase space density curve. Dashed black line is the constant energy curve. Solid magenta line is the diffusion curve and the arrow indicates the direction for electron diffusion.

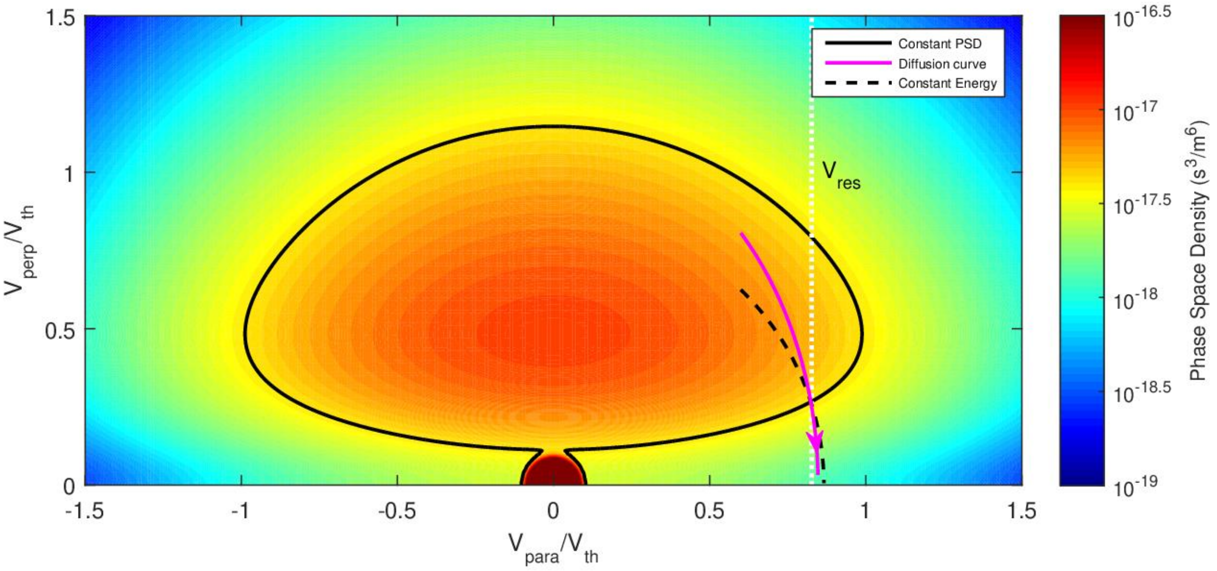

Figure 1.7: Geometric interpretation of ECH wave excitation by loss cone distributions. The electron distribution function is listed in Table 1.1. The background magnetic field strength is 50nT. Parallel velocity on the horizontal axis and perpendicular velocity on the vertical axis are normalized to the thermal velocity of the first component in Table 1.1. The solid black line represents constant phase space density, and the dotted black line represents constant particle energy. Contour of Eq. (1.11) is indicated by the solid magenta line with an arrow pointing towards the direction of particle diffusion. The resonance velocity is indicated by the dotted white line.

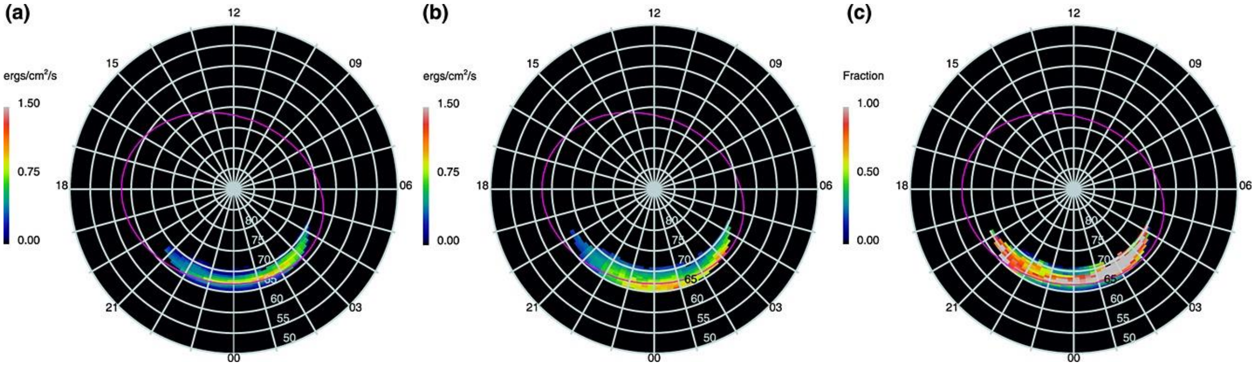

Figure 1.8: Ionospheric distribution of (a) ECH wave-induced electron precipitation energy flux, (b) diffuse auroral precipitation from OVATION Prime model under median solar wind driving condition during ECH wave measurement intervals, and (c) fraction of diffuse auroral precipitation contributed by ECH wave scattering. The magenta ovals mark the latitudes which map to equatorial radial distance of 8 RE in T89 magnetic field model. (Figure adapted from Zhang et al. [2015])

Table 1.1 Electron distribution function

Component	n (cm^{-3})	$T_{||}$ (eV)	$T_{\perp}/T_{\parallel}$	Δ	β
1 Hot electron	0.5	1000	1	0.2	0.1
2 Cold electron	0.05	1	1	1	0.5

Chapter 2

Off-equatorial current-driven instabilities ahead of approaching dipolarization fronts

Kinetic simulations in Pritchett et al. [2014] have revealed that electromagnetic instabilities near the ion gyrofrequency and located slightly away from the equatorial plane can be driven by a current parallel to the magnetic field prior to the arrival of dipolarization fronts. Current-driven electromagnetic ion cyclotron instability and current driven kink-like instability, which have been introduced in Section 1.6, could be consistent with the instabilities in simulations. Such instabilities are important because of their potential contribution to global electromagnetic energy conversion near dipolarization fronts. In this chapter, we used THEMIS observational data to confirm the existence and investigate the characteristics of these instabilities.

The outline of this chapter is as follows. In Section 2.1, we introduce the current-driven electromagnetic instabilities in simulations and their potential candidates. In Section 2.2 we describe the instrumentation and the event selection criteria used in our search. Section 2.3 is a detailed case study of one event with instabilities located off the equator at the plasma sheet boundary layer. Section 2.3.1 demonstrates the wave observation results with two different instabilities observed at the boundary layer. Section 2.3.2 shows the electron and ion distribution functions and identifies the parallel current resulting from the drift of electrons opposite the magnetic field. In Section 2.3.3, we did an instability analysis to characterize the instabilities we observed. In Section 2.3.4, we compared the results of the instability analysis with the simulation instability. Section 2.4 is a summary and discussion of our findings.

2.1 Introduction

Bursty bulk flows (BBFs), plasma flows often observed in the magnetotail with a predominantly earthward direction, short lifetime (typically 10-15 minutes), and high speed (greater than 400 km/s) provide the dominant earthward transport of mass, energy, and magnetic flux observed in that region [Baumjohann et al., 1990; Angelopoulos et al., 1992; 1994]. These flows could be generated from near-Earth reconnection at about 20-30 R_E [Angelopoulos et al., 2008; Angelopoulos et al., 2013; Fu et al., 2013], or by interchange instabilities [Pritchett and Coroniti, 1998, 2010, 2013]. Magnetic field structures more dipolar than the ambient magnetic field, referred to as dipolarizing flux bundles [Liu et al., 2013a, b, 2014], are frequently observed within BBFs. Dipolarizing flux bundles (DFBs) have sharp magnetic field edges called dipolarization fronts (DFs) [Nakamura et al., 2002] or reconnection fronts [Angelopoulos et al., 2013]. Often transient,dipolarizing flux bundles exhibit a sharp increase in B_z (the north - south component of the magnetic field in GSM coordinates) usually preceded by a small decrease in B_z [Ohtani et al., 2004; Runov et al., 2009, 2011; Liu et al., 2013a] and a decrease in the magnitude of B_x in a larger region [Yao et al., 2015] They are often seen in series and are followed by intervals of prolonged (tens of minutes) dipolarized B_z, the tailward-most extension of the influence of the Earth's dipole. These prolonged dipolarized B_z intervals are called magnetic flux pileup regions [Baumjohann et al., 1999]. They signify the lack of an intense cross-tail current and usually develop during substorms.

Dipolarization fronts are considered to be very dynamic environments in which different types of instabilities have been identified. Lower hybrid waves, kinetic Alfvén waves, electromagnetic ion cyclotron waves (EMIC waves), magnetosonic waves, and higher-frequency waves, such as whistler waves and electron cyclotron harmonic waves (ECH waves), have been observed near these fronts [Le Contel et al., 2009; Sergeev et al., 2009; Zhou et al., 2009; Deng et al., 2010; Huang et al., 2012; Zhang et al., 2014].In addition, kinetic-scale processes at DFs play a very important role in global electromagnetic energy conversion [Birn and Hesse, 2005; Eastwood et al., 2010; Angelopoulos et al., 2013].

Although most instabilities have been observed near dipolarization fronts at the central plasma sheet, recent 3D PIC (particle-in-cell) simulations found electromagnetic instabilities at the plasma sheet boundary layer (PSBL), just ahead of approaching dipolarization fronts [Pritchett et al., 2014]. In the simulations, wave fluctuation was very strong in both the magnetic field and the electric field, as well as in background electron and ion density (Figure 8 in [Pritchett et al., 2014]). The peak amplitudes of E_y oscillations are about 30-50mV/m, and the $\delta E/\delta B$ ratio is about 4 times the local Alfvén speed. The E_y oscillations are located off the equator in z direction, at the density gradient region away from the central plasma sheet and extend across the entire DF in the azimuthal direction (Figure 9 in [Pritchett et al., 2014]). The instability was found to have wavelength comparable to the local ion inertial length and frequency near the local ion cyclotron frequency (0.96 Ω_{ci} (the ion cyclotron frequency)), much lower than Ω_{lh} (the lower hybrid frequency).The instabilities were highly oblique and propagated in the duskward direction with a typical speed of about 0.5 V_{ith}(ion thermal velocity) (Figure 10 in [Pritchett et al., 2014]). The oscillations preceded the arrival of the DF and started to reach their peak amplitudes as the front approached. A large parallel current, resulting from a net parallel drift between electrons and ions (about 3.5 V_{ith}), was likely the free energy source for wave generation (Figure 11 in [Pritchett et al., 2014]). The instabilities are driven by a parallel current, a diversion of the perpendicular current near the equator, which connects to the global current system in the magnetotail [Liu et al., 2013a, 2015]. That the free energy source for wave generation is this parallel current rules out the possibility of the instability being a lower hybrid instability, which is driven by diamagnetic currents in perpendicular direction [Daughton, 2003; Gary, 1993]. The field-aligned currents in the vicinity of the dipolarization fronts could potentially be related to the substructure parallel electron beam distribution observed near the fronts [Liang et al., 2013; Yao et al 2016]. Such instabilities, which relax by reducing the parallel current, have the potential to contribute to global energy dissipation. These instabilities radiate intense wave power at the boundary layer, serving as the precursor to the arrival of the DF.

In a two-component plasma, there are various current-driven instabilities near the ion cyclotron frequency, such as the electrostatic ion acoustic instability, the electrostatic ion cyclotron instability, and the electromagnetic ion cyclotron instability [Gary and Forslund, 1975]. In this paper, we focus on two of those instabilities, which have the smallest drift velocity threshold of any current-driven instabilities. One is the current-driven kink-like instability (otherwise known as the current-driven Alfvén instability). This fluid instability has a maximum growth rate when parallel to the magnetic field [Gary et al., 1976], but can also become unstable when oblique to the magnetic field [Perraut et al., 2000]. Driven by a parallel current, the kink-like instability results from coupling between the shear Alfvén mode and the fast magnetosonic mode. The frequency and growth rate of the instability increase when the current increases. The other notable current-driven electromagnetic instability is the electromagnetic ion cyclotron instability, which has a weak cyclotron resonance with ions and Landau resonance with electrons [Gary and Forslund, 1975]. Above the instability threshold, the most unstable mode has a frequency range of about 0.5 - 0.8 Ω_{ci} and propagates very obliquely to the ambient magnetic field with perpendicular wave number approximately ten times larger than the parallel wave number [Forslund et al., 1979]. Both of these current-driven instabilities could explain the instability observed in simulation.

2.2 Data and Event Selection

The original THEMIS mission consisted of five identical probes (P1, P2, P3, P4, and P5) carrying a comprehensive plasma and field instrument suite [Angelopoulos, 2008; Sibeck and Angelopoulos, 2008]. The THEMIS Fluxgate Magnetometer (FGM) measures the magnetic field and its low-frequency fluctuations (up to 64 Hz) [Auster et al., 2008]. During the fast-survey collection mode, low resolution magnetic field data – the FGL data product at 4 data points per second - are available. We use the geocentric solar magnetospheric (GSM) coordinate system throughout most of our paper except when we discuss the magnetic field data in the field-aligned coordinate (explained later). The THEMIS electrostatic analyzers (ESA) measure electron and ion energy fluxes (from a few eV to 30 keV for electrons and to 25 keV for ions) and moments (density, velocity, temperature, and pressure) [McFadden et al., 2008].

Data from two Z-separated satellites (P5 and P3 or P4) were searched for low-frequency fluctuations at the PSBL consistent with the waves in the Pritchett et al. [2014] simulation. P5 is typically separated from the other two spacecraft by 0.5-1R_E , within the limits in our search strategy. Our search method requires one satellite to be at the central plasma sheet (near the neutral sheet) and observe dipolarization fronts. To identify dipolarization fronts, we used the event list of Liu et al. [2013a]. The most important criterion in finding DF events in that list is the sharp change in B_z ($\partial B_z/\partial t > 0.5\ nT/s$). The other satellite is required to be farther from the neutral sheet, with separation from the first satellite in the X_{GSM} and Y_{GSM} directions smaller than that in the Z_{GSM} direction. Thus, our selection criteria for dual (Z-separated) observations of DF events is as follows:

1. The first satellite observed a dipolarization front and the average value of B_x from 5 to 1 minutes before the DF arrival is less than 10 nT (this ensures that the DF observation is close to the neutral sheet).
2. The Z_{GSM} separation between the two satellites is larger than $0.5R_E$. The X_{GSM} and Y_{GSM} separation is less than $0.5\ R_E$

We looked through all DF cases from 2009 to 2013 and found 131 events that satisfy our event selection criteria. All cases were carefully investigated. Magnetic field data and wave polarization analysis methods were used to look for instabilities near the ion cyclotron frequency prior to arrival of the dipolarization front. Clear (monochromatic) wave signatures that could be easily distinguished in wave spectra and high coherence were essential for identification of a good case. We also utilized particle fluxes and moment data to determine whether there was current parallel to the magnetic field associated with the instabilities that could serve as a driver for the instabilities. After manually searching through all 131 candidate cases a few good cases were found. One such case, on 21 July 2012, with clear wave signatures and parallel current, is presented here.

2.3 Case Study

2.3.1 Wave Observations

THEMIS-D (P3), which was at the central plasma sheet, observed the dipolarization front starting at 11:57:05 UT; THEMIS-A (P5) was at the plasma sheet boundary layer with a large B_x component. The Z_{GSM} separation between the two satellites was about 1 R_E. The x and y separations were about 0.3 R_E and 0.2 R_E. Both satellites were located at about 10 R_E in the x direction.

Figure 2.1 shows an overview of the event, including wave polarization analysis, from 11:47 UT to 12:07 UT. The top four panels are the magnetic field and ion flow velocity observed by TH-D and TH-A. The vertical dashed line in (a) and (b) marks the arrival of the dipolarization front at 11:57:05 UT on TH-D. Low-frequency waves were evident at TH-A about 20 seconds before the arrival of the DF; these are better illustrated in Figure 2.2. An earthward bursty bulk flow associated with the dipolarization front was observed at TH-D; no significant ion flows were observed at TH-A. The bottom four panels are wave polarization analysis of the magnetic field data at TH-A. This analysis was done using FGL magnetic field data after filtering with a bandpass range from 0.1 Hz to 2 Hz. The white thick line in the wave power spectrum (Figure 2.1e) is the ion cyclotron frequency, which is about 0.7 Hz in this case. The degree of polarization, otherwise referred to as coherence, with a scale from 0 to 1 is shown in Figure 2.1f. Reddish color indicates coherent waves; coherence less than 0.7 suggests noise. Large wave power combined with a high degree of polarization is a good indicator of coherent waves. The instability of interest has a frequency of about 0.3 Hz and a high degree of polarization. The wave normal angle (Figure 2.1g) is the angle between the wave vector and the ambient magnetic field, and “ellipticity” (Figure 2.1h) indicates the ellipticity of the wave. Positive refers to righthand polarized and negative refers to lefthand polarized. In terms of wave normal angle and ellipticity, only instabilities with wave power spectral density greater than $0.7nT/\sqrt{Hz}$ and degree of polarization larger than 0.9 were plotted. Figures 2.1g and 1h demonstrate that the instability is lefthand polarized and propagates at an angle of about 45^0 with respect to ambient magnetic field. The wave normal angle and ellipticity were farther confirmed by minimum variance analysis and visually inspecting the hodogram in the plane of polarization.

Figure 2.2, a detailed view of the magnetic and electric field at TH-A during a two minute time interval from 11:56:05 to 11:58:05UT, helps illustrate the instability signature. The magnetic field data was filtered in a bandpass range from 0.1Hz to 2Hz in GSM coordinates in Figure 2.2(b), (c), (d) and in mean-field-aligned (MFA) coordinate in Figure 2.2(e), (f), (g). The Z_{MFA} axis is the magnetic field direction; the Y_{MFA} axis is on the plane defined by minus phi (phi is the azimuthal vector in solar magnetospheric coordinates); and the X_{MFA} axis completes the orthogonal righthand system. The instability signature is strong (>2nT peak-to-peak) and coherent, with its dominant component perpendicular to the ambient field direction. The electric field data was cleaned by manually removing the unphysical periodic spikes caused by the boom shadowing in the first place and then filtered in a bandpass range from 0.1Hz to 2Hz in despun sun - L-vectorZ (DSL) coordinates in Figure 2.2(h), (i), (j). The Z_{DSL} axis is along the spin axis of the spacecraft and the electric field data along Z_{DSL} is set to be zero since the measurement of the electric field along the spin axis is inaccurate. Electric field data from TH–A at that time also show strong fluctuations at the same frequency as the magnetic field fluctuation, about 0.3 Hz.

Apart from the most prominent instability at a frequency of about 0.3 Hz (denotes Instability 1), another lower frequency instability was found at about 0.02 Hz (denotes Instability 2). Figure 2.3 still illustrates the magnetic field plot and wave analysis at TH-A but over an expanded, one hour interval. The magnetic field data was filtered with a bandpass range from 5mHz to 0.2Hz. The bottom four panels are wave polarization analysis. Only instabilities with wave power spectral density larger than 1 $nT/\sqrt{Hz}$ and degree of polarization larger than 0.8 were plotted in the wave normal angle and ellipticity panels (g) and (h). We can infer that Instability 2 is at ~ 0.02 Hz, propagates quasi parallel to the magnetic field, and is righthand polarized.

Both instabilities we observed were far from the neutral sheet (as evidenced by the large B_x component) and could be the instability discussed in Pritchett et al. [2014]. Observations of electron and ion distribution functions and detailed instability analysis will be discussed in the following section, which will help us identify what types of instabilities they are and whether they are consistent with the instabilities found in the simulation.

2.3.2 Observed and Fitted Distribution Function

In the simulation the instability was thought to be driven by a parallel current caused by differential drift of ions and electrons. To determine whether such a current was present, we examined electron and ion distribution functions at TH–A when the instabilities were observed. Figure 2.4(a) shows the electron pitch-angle versus energy distribution function spectrum when the waves were present. In the electron differential flux in the antiparallel and parallel directions, we can easily discern a clear asymmetry between antiparallel and parallel electron flux that indicates the existence of an electron drift in the antiparallel direction. Figure 2.4(b) shows the phase space density versus energy. By comparing antiparallel electron and parallel electron phase space density (PSD) in the energy range of about 100 – 200 eV, we can further confirm that a net antiparallel drift for low-energy electrons existed.

We also examined the ion distribution functions, but no ion drift was found. Thus, we concluded that there was a current in parallel direction, resulting from the antiparallel drift of low energy electrons when the instabilities were present at TH–A.

We assumed that the electrons consisted of two populations: one cold with an antiparallel drift and lower number density and one hot with no drift and higher number density. A two-dimensional fit of the electron phase space density was performed. An additional electron population with high temperature, low number density and no drift was added when fitting the electron phase space density. Figure 2.5 compares our fitted electron distribution function with the observed distribution function. Only data from energy channels above 97.2 eV were used in fitting the observational data, since there was photoelectron and secondary electron contamination at very low energies. The fitting result of cold electron component and two hot electron components is shown in the text box at the right of the figure.

The electron distribution functions at each spin period (3s) during which the instability was present (from 11:56:44 UT to 11:57:14 UT) were fitted. Figures 2.6a, 2.6b and 6c are the observed electron distribution function at three different times: 11:56:53 UT; 11:56:59 UT and 11:57:05 UT. The DF arrives at 11:57:05 UT at TH–D and the instabilities observed at TH–A lasted from about 11:56:45 UT to 11:57:20 UT. The electron distribution functions are plotted in a plane parallel (horizontal axis) and perpendicular (vertical axis) to the ambient magnetic field. The plane is chosen to contain the ion flow velocity direction. The big red dot in the middle of the distribution function slice is the photoelectron contamination. The asymmetry between antiparallel and parallel electrons is also evident at the low energy part in the distribution function cuts - this again confirms the existence of the antiparallel drift of a cold electron component. Figure 2.6d is the fitted drift velocity of the cold component electron versus time. The cold electron drift in the antiparallel direction coexists with presence of instabilities at TH-A, which indicates that this parallel current resulting from an electron drift might play an important role in exciting the instabilities observed at the boundary layer. The correspondence between the three electron distribution function slices and three different fitted drift velocities is marked by the arrows.

Ion and electron plasma parameters from observations and fitting results are listed in Table 2.1. Because we did not observe any temperature anisotropy or drift in the ion distribution function, background plasma parameters were used, and no temperature anisotropy or drift was assumed. In terms of electrons, the fitting result at 11:56:58 UT was listed in the Table 2.1. The two hot electron populations have very small drift and no temperature anisotropy; the cold electron population has a drift velocity of ~830 km/s, about 0.2 times $V_{eth,c}$ (the thermal velocity of the cold electron population in the parallel direction), and $T_{||}/T_{\perp}$ is approximately 2. The number density of hot and cold electron components was adjusted slightly so their sum equals the ion number density. The plasma parameters listed in Table 2.1 were then used as input parameters for the instability analysis.

2.3.3 Instability analysis

We solved the hot plasma dispersion relation using WHAMP (Waves in Homogeneous Anisotropic Magnetized Plasma), a program that can solve the kinetic dispersion relation by using a bi-Maxwellian distribution function as input [Ronnmark, 1982]. We would like to mention here that when we did the instability analysis, the drift velocity of the cold electron component was set to be 0.7 $V_{eth,c}$ (2900 km/s); the drift velocity from our fitting result was 0.2 $V_{eth,c}$ (830 km/s). We used a larger drift velocity because the current-driven ion cyclotron instability was stable when 0.2

$V_{eth,c}$ (830 km/s) was used as an input to the drift velocity. This will be further discussed in the next section as part of our parametric study.

The dispersion surfaces for current-driven kink-like instability (Figure 2.7a) and current-driven ion cyclotron instability (Figure 2.7b) are shown in Figure 2.7. The current-driven kink-like instability has a positive growth rate over a large range of parallel and perpendicular wave numbers. The most unstable kink-like mode has a maximum growth rate in the parallel direction, when the normalized wave frequency is 0.02 and the normalized growth rate is 0.2. The most unstable mode of the ion cyclotron instability is in the quasi-perpendicular direction when the wave normal angle is about 81°. The normalized wave frequency is about 0.47, and the normalized wave growth rate is about 0.001.

A comparison between the most unstable mode of the current-driven ion cyclotron instability and the first instability we observed at a frequency of about 0.3 Hz is shown in Table 2.2. Table 2.3 illustrates the comparison between the most unstable mode of kink-like instability and the second instability we observed at about 0.02 Hz.

For the current-driven ion cyclotron instability, the normalized frequency of the most unstable mode is about 0.47, and the frequency of the first instability we observed is about 0.4 Ω_{ci}. The two results are therefore consistent. Both the ion cyclotron instability and the first instability we observed are lefthand polarized. In terms of the wave normal angle, the ion cyclotron instability has a maximum growth rate at about 81^0; the first instability we observed, however, propagated at about 50°. Even so, the ion cyclotron instability still has positive growth rate at a smaller wave normal angle. The growth rate of the ion cyclotron instability is small, probably due to the small drift velocity we observed. It would increase if there is a larger current as we discuss in the following section. We then compared the $\delta E/\delta B$ ratio of the first instability we observed and the $\delta E/\delta B$ ratio of the ion cyclotron instability. The transverse component (in the direction perpendicular to the wave vector $\vec{k}$) of the electric and magnetic field data was used in calculating the $\delta E/\delta B$ ratio. Since we do not have good measurements of the electric field data along the spin axis of the spacecraft, we used the component perpendicular to both the wave vector and the spin axis as the transverse component of the electric field and the component perpendicular to the transverse electric field direction as the transverse component of the magnetic field. The local Alfvén velocity (V_A) is about 2000km/s and $\frac{\delta E_{transverse}}{\delta B_{transverse}}\frac{1}{V_A}$ is 0.14 for the first instability we observed. Regarding the $\delta E/\delta B$ ratio of the ion cyclotron instability from WHAMP results, $\frac{\delta E_{transverse}}{\delta B_{transverse}}\frac{1}{V_A}$ is about 0.16, which matches quite well with the $\delta E/\delta B$ ratio from observation.

In terms of the current-driven kink-like instability, the frequency of the most unstable instability is about 0.02 Ω_{ci} and the second instability we observed has a frequency of about 0.014 – 0.03 Ω_{ci}. Both the second instability we observed and the kink-like instability propagate at the direction parallel to the magnetic field to and they are both righthand polarized.

By comparing these two different types of current-driven instabilities from the WHAMP program and our observations at the boundary layer, we conclude that the first instability we observed at a frequency of about 0.3 Hz is the ion cyclotron instability and the second instability at a much lower frequency is the current-driven kink-like instability.

2.3.4 Comparison with the Simulation Instability

It is not immediately apparent whether either of the two instabilities identified in the THEMIS observations is consistent with the higher frequency instability observed in the Pritchett et al. [2014] simulation. This simulation instability had a very large electron-ion drift of the order of 3.5 V_{ith}(~2400km/s), a frequency comparable to Ω_{ci}, was highly oblique, and had a large ratio $\delta E/\delta B$ approximately 4 V_A. To investigate this question, we repeat the WHAMP analysis but now using plasma parameters corresponding to those in the simulation: A two-component plasma with ion drifting in the direction parallel to the background magnetic field at a velocity of 0.2 V_{ith}(~140km/s) and electron drifting at a velocity of 3.7 V_{ith}(~2500km/s) was used as an input distribution function to WHAMP (Figure 11 in [Pritchett et al., 2014]); mass ratio was changed to be m_i/m_e= 64 and normalized wave vector in the cross-tail direction was $k_y\rho_{ci}$ = 2.6. For the kink-like instability the WHAMP specific parameters used were $k_{||}\rho_{ci}$= 0.46, $k_{\perp}\rho_{ci}$= 2.6, and wave normal angle of 80 degrees, while for the ion cyclotron instability $k_{||}\rho_{ci}$ = 0.22, $k_{\perp}\rho_{ci}$= 2.6, and wave angle of 85 degrees. The resulting frequency was ω/Ω_{ci}= 1.22 for the kink-like instability and ω/Ω_{ci}= 0.8 for the ion cyclotron instability. Both values are roughly consistent with the simulation result of ω/Ω_{ci}= 0.96. However, the agreement for the growth rate and $\delta E/\delta B$ ratio are much better for the kink-like instability (γ/Ω_{ci}= 0.74 and $\frac{\delta E_{\perp}}{\delta B_{||}}$ = 0.65V_A) than for the ion cyclotron instability (γ/Ω_{ci}=0.013 and $\frac{\delta E_{\perp}}{\delta B_{||}}$ = 0.11 V_A). The growth rate of ion cyclotron instability is much too small to have produced the observed instability given that the total simulation run time was only slightly more than one e-folding time for that mode. While the $\delta E/\delta B$ value for the kink-like instability is considerably less than the simulation value of 4 V_A the simulation observed the instability in a strongly nonlinear stage, and this may account for part of the discrepancy. Also, the linear $\delta E/\delta B$

value for the kink-like instability is larger than unity for slightly less oblique propagation angles of $\theta < 60$ degrees. It thus seems likely that the simulation instability is the current-driven kink-like instability. This identification is also consistent with the results of Perraut et al. [2000] that showed that the current-driven kink-like instability is obliquely unstable with frequency near Ω_{ci} when the relative electron-ion drift increases to the order of one-tenth of the electron thermal speed or higher.

2.4. Summary and Discussion

We used observations from two THEMIS satellites to search for electromagnetic instabilities at the boundary layer identified in the Pritchett et al. [2014] simulation. By surveying all dual (Z-separated) satellite observations of dipolarization fronts from 2009 to 2013, we found several cases with clear wave signatures, one of which we examined in greater detail. As expected from the simulation results, we found a parallel current that might excite an instability. Two electromagnetic instabilities were observed at TH–A, which was away from the equator; a dipolarization front was observed by TH–D, which was at the central plasma sheet near the equator. One instability, at a frequency of about 0.3 Hz, is lefthand polarized, and propagating obliquely. The other, at a much lower frequency, exhibits righthand polarization and parallel propagation. The electron distribution function, which was fitted by assuming a cold, tenuous drifting population and two hot, dense, non-drifting populations, shows an antiparallel drift in the low-energy range. The fitted results clearly demonstrate that the antiparallel electron drift coincides with the presence of the instabilities, suggesting that this drift is likely the instability driver. No ion drift was observed at that time. An instability analysis was performed to determine whether the observed instabilities were consistent with the observed free energy source.

By comparing the two instabilities we observed with the two instabilities driven by the current using the linear theory hot plasma dispersion solver (WHAMP), we concluded that: (1) the instability observed at a frequency of about 0.3Hz is the electromagnetic ion cyclotron instability based on similarity in frequency, oblique propagation, lefthand polarization and $\delta E/\delta B$ ratio between the observations and the numerical solution of the dispersion relation; (2) the instability observed at a much lower frequency of about 0.02 Hz is likely the current-driven kink-like instability based on the similarity in wave frequency, wave normal angle, and ellipticity between data and the numerical dispersion relation solution.

We used the plasma parameters in the PIC simulation by Pritchett et al. [2014] as an input to WHAMP to calculate the linear dispersion relation of kink like instability and electromagnetic current driven ion cyclotron instability. The instability found in the simulation is likely to be kink like instability based on several reasons: (1)the consistency in wave frequency (ω/Ω_{ci}) between the kink like instability in WHAMP results and the instability found in PIC simulation; (2)a much better agreement on the growth rate and $\delta E/\delta B$ ratio for the kink-like instability than for the ion cyclotron instability. In result, the instability found in PIC simulation is the current-driven kink-like instability, most relevant to the second instability we observed with much lower frequency.

In our instability analysis, the drift velocity of the cold electron population was set to be 0.7 $V_{eth,c}$ (2900 km/s) (the parallel thermal velocity of cold electrons). The drift velocity from our fitting result is only 0.2 $V_{eth,c}$ (about 830 km/s), however. We did a parametric study to identify the electromagnetic ion cyclotron instability threshold by slowly increasing the drift velocity of cold electrons. The instability started to become unstable when the drift velocity was above 0.6 $V_{eth,c}$, and we found that it had the relatively large growth rate when the drift velocity was at about 0.7 $V_{eth,c}$. Thus, in our instability analysis we used 0.7 $V_{eth,c}$ as the drift velocity of cold electrons, rather than 0.2 $V_{eth,c}$, which we obtained from fitting results. The requirement for a larger drift velocity suggests that the instability might be generated from somewhere else where there was a larger current for the instability to grow unstable. Another possibility is that the low time resolution of the instrument prevents us from obtaining the maximum electron beam speed at the time (it takes 3 seconds for the satellite to acquire a full electron distribution function, and the field line is only sampled for a small fraction of that time). Also noteworthy is that the calculated growth rate of the ion cyclotron instability is very small compared with that of the kink-like instability. The maximum growth rate of ion cyclotron instability is at around $10^{-3}\Omega_{ci}$ and the e-folding time for this wave mode to grow is too long to be realistic. This could also be explained by temporally aliased observations of the electron current.

Among all 131 cases that satisfy the desired satellite configuration (one near the neutral sheet and the other away from the equator), only a few with a clear desired wave signature were found. Thus, this type of wave with monochromatic signatures seems to be quite rare, perhaps because of the large current that the instability needs to become unstable. In the Pritchett et al. simulation, the differential drift between ion and electron is about 3.5 V_{ith} (~2400km/s), quite a large current considering that in the simulation, the entire electron population was drifting. Such a large current is very rare in the magnetotail. Even if such large current exists, we are unlikely to observe it because the fast beam could thermalize very quickly, and the time resolution of the data is insufficiently high to capture the features of those beams. Another explanation for the rarity of observations of this kind of instability is its broadband characteristics. Both the ion cyclotron instability and the kink-like instability are very broadband instabilities, which could be easily mixed up with low-frequency turbulence caused by fast plasma flows, increasing our difficulties in finding good events. Cross-correlation methods between different spacecraft along the magnetic field or ion flow direction may remove low-frequency turbulence, and thus be better able to isolate coherent ion cyclotron and kink-like instabilities related to current-driven instabilities. This may be able to reveal more instability cases and the instabilities' potential importance for energy conversion and other processes near dipolarization fronts.

Table 2.1

	n (cm^{-3})	$T_{\|\|}$ (keV)	$T_{\|\|}/T_{\perp}$	$V_{drift}/V_{thermal}$
Ion	0.24	2.71	1	0
Hot Electron 1	0.127	0.544	1	- 0.015
Hot Electron 2	0.054	1.214	0.98	-0.004
Cold Electron	0.059	0.049	2.06	- 0.20

Table 2.2

Properties of wave	Observation	Numerical
Wave frequency (ω/Ω_{ci})	≈ 0.4	0.47
Wave normal angle	≈ 50°	81°
Ellipticity	Left hand	Left hand
$\frac{\delta E_{transverse}}{\delta B_{transverse}}\frac{1}{V_A}$	0.14	0.16
Growth rate (γ/Ω_{ci})		0.00112
$k_{\|\|}\rho_{ci}$		0.16
$k_{\perp}\rho_{ci}$		1.02

Table 2.3

Properties of wave	Observation	Numerical
Wave frequency (ω/Ω_{ci})	≈ 0.014 – 0.03	0.02
Wave normal angle	≈ 0° - 30°	0°
Ellipticity	Right hand	Right hand
Growth rate (γ/Ω_{ci})		0.2
$k_{\|\|}\rho_{ci}$		0.075
$k_{\perp}\rho_{ci}$		0

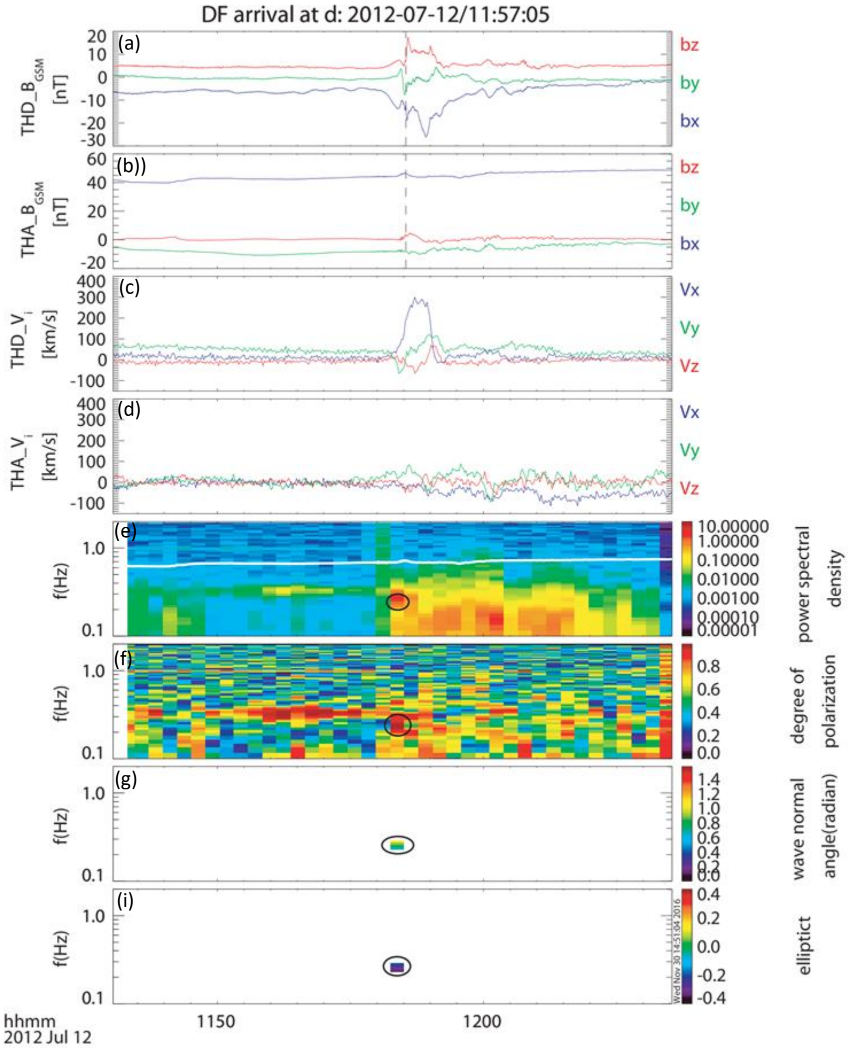

Figure 2.1. Overview plot of 2012 July 12 event and wave polarization analysis. (a) and (c): Magnetic field and ion bulk flow velocity in GSM coordinate at TH-D (at the central plasma sheet); (b) and (d): Magnetic field and ion bulk flow velocity at TH-A (at the boundary layer). The dashed line marks the arrival of DF at TH-D. (e) - (h): Wave polarization analysis of magnetic field at TH-A. Power spectral density, degree of polarization, wave normal angle and elliptic at frequency range of 0.1 – 2 Hz. The instability we are interested in is marked by a circle.

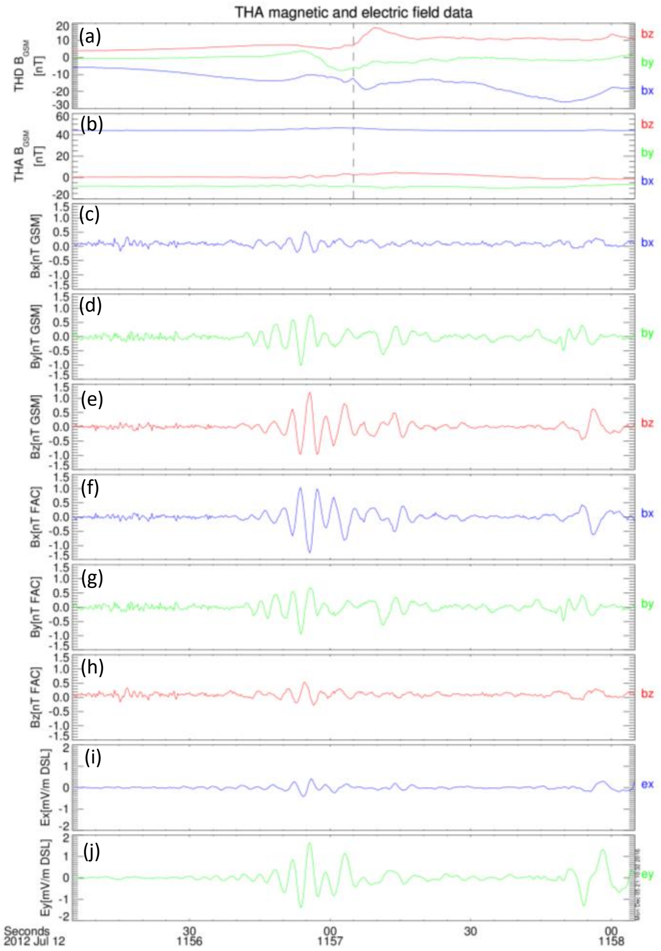

Figure 2.2. Magnetic and electric field plot at THEMIS-A from 11:56:05 to 11:58:05 after filtering with a band range from 0.1 Hz to 2Hz. (a): Raw magnetic field data at TH-D; (b): Raw magnetic field data at TH-A, the dashed vertical line marks the arrival of DF at TH-D; (c) -(e): Bx, By, Bz component in GSM coordinate after filtering; (f) – (h): Bx, By, Bz component in MFA coordinate after filtering; (i) – (j): Ex, Ey component in DSL coordinate after filtering.

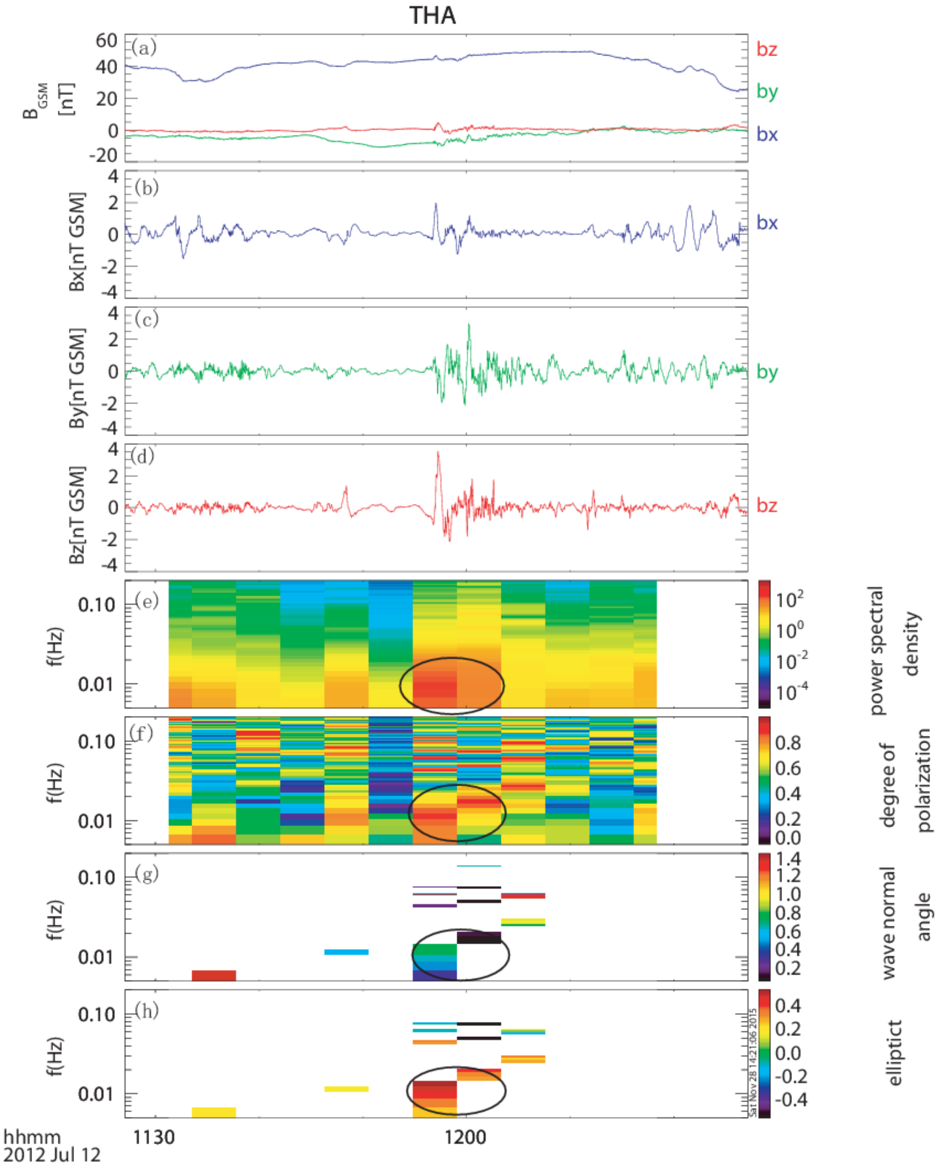

Figure 2.3. Magnetic field plot and wave polarization analysis at TH-A. Time range is from 11:27:05 to 12:27:05. (a): Magnetic field raw data; (b) – (d): Bx, By, Bz component after filtering. The bandpass range is from 5 mHz to 0.2 Hz; (e) – (h): Power spectral density, degree of polarization, wave normal angle and elliptic. The instability we are interested in is marked by a circle.

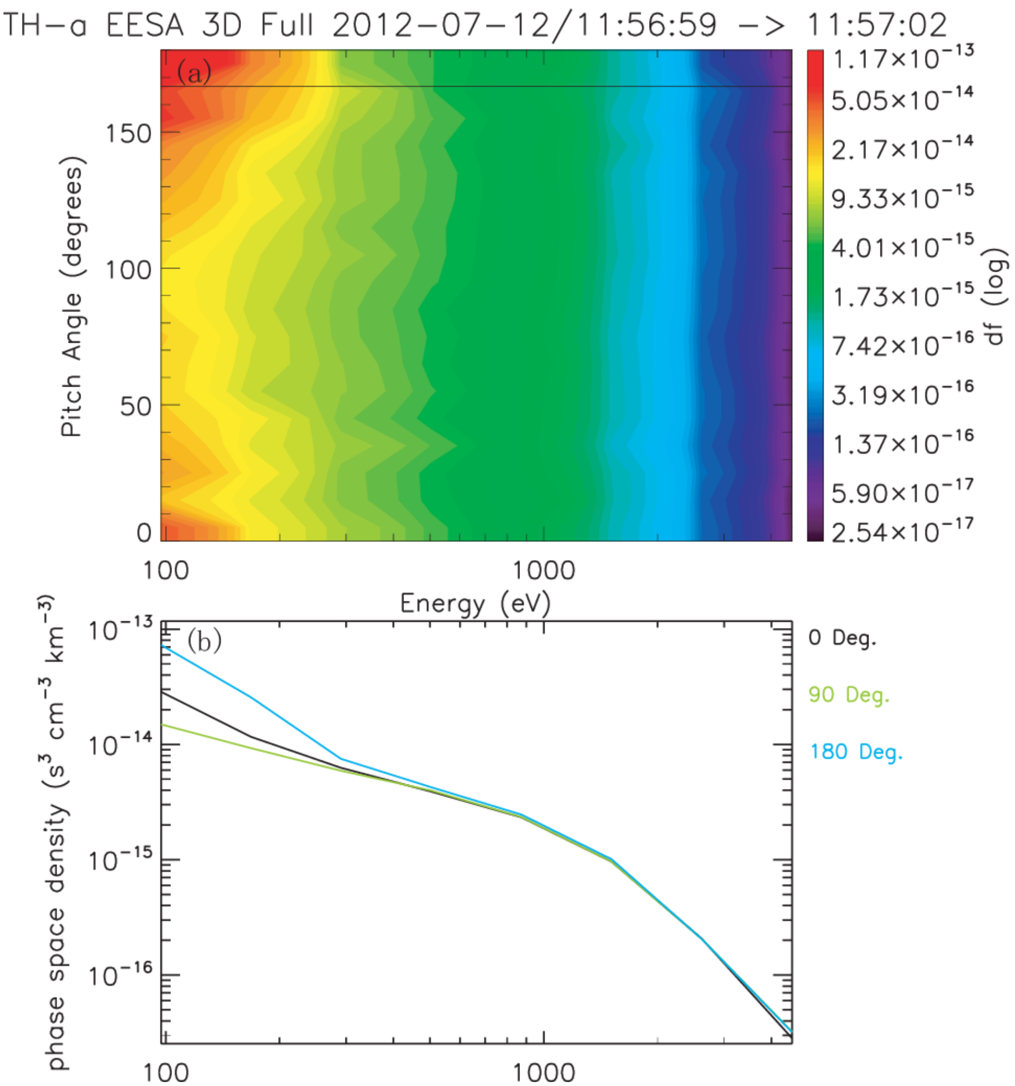

Figure 2.4. Observed electron distribution function in $s^{-3}cm^{-3}km^{-3}$ (a): Pitch angle versus energy; (b): PSD (phase space density) versus energy, black line is when pitch angle is 0 degree, green line is when pitch angle is 90 degree, blue line is when pitch angle is 180 degree

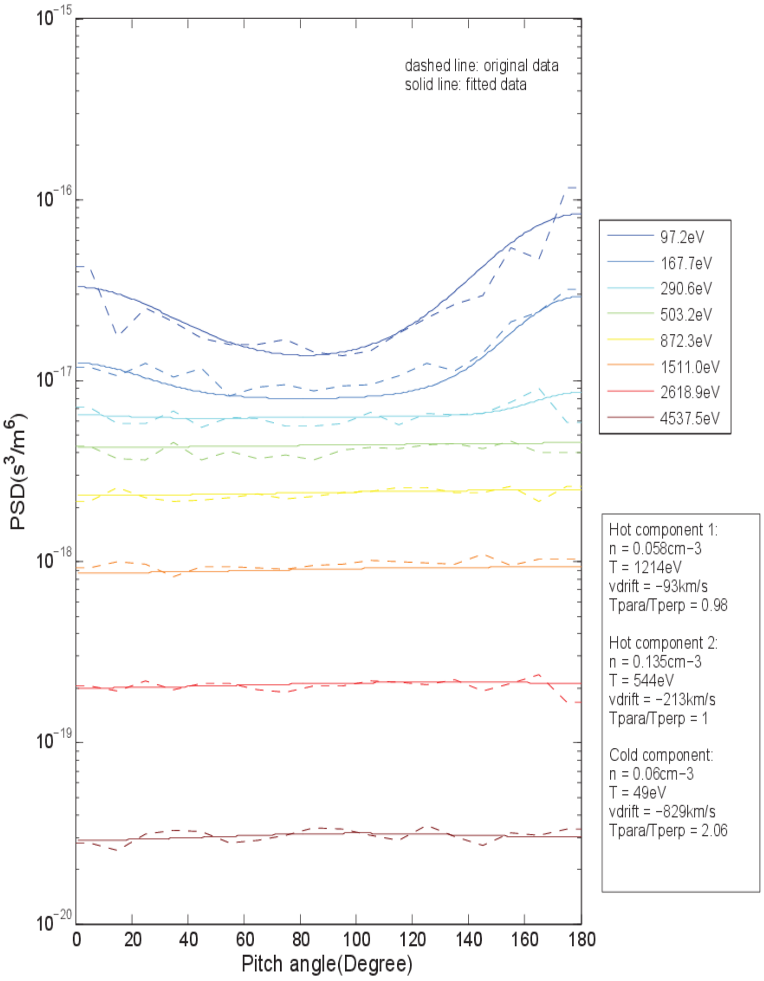

Figure 2.5. Phase space density versus pitch angle. Dashed line is observed PSD and solid line is fitted PSD

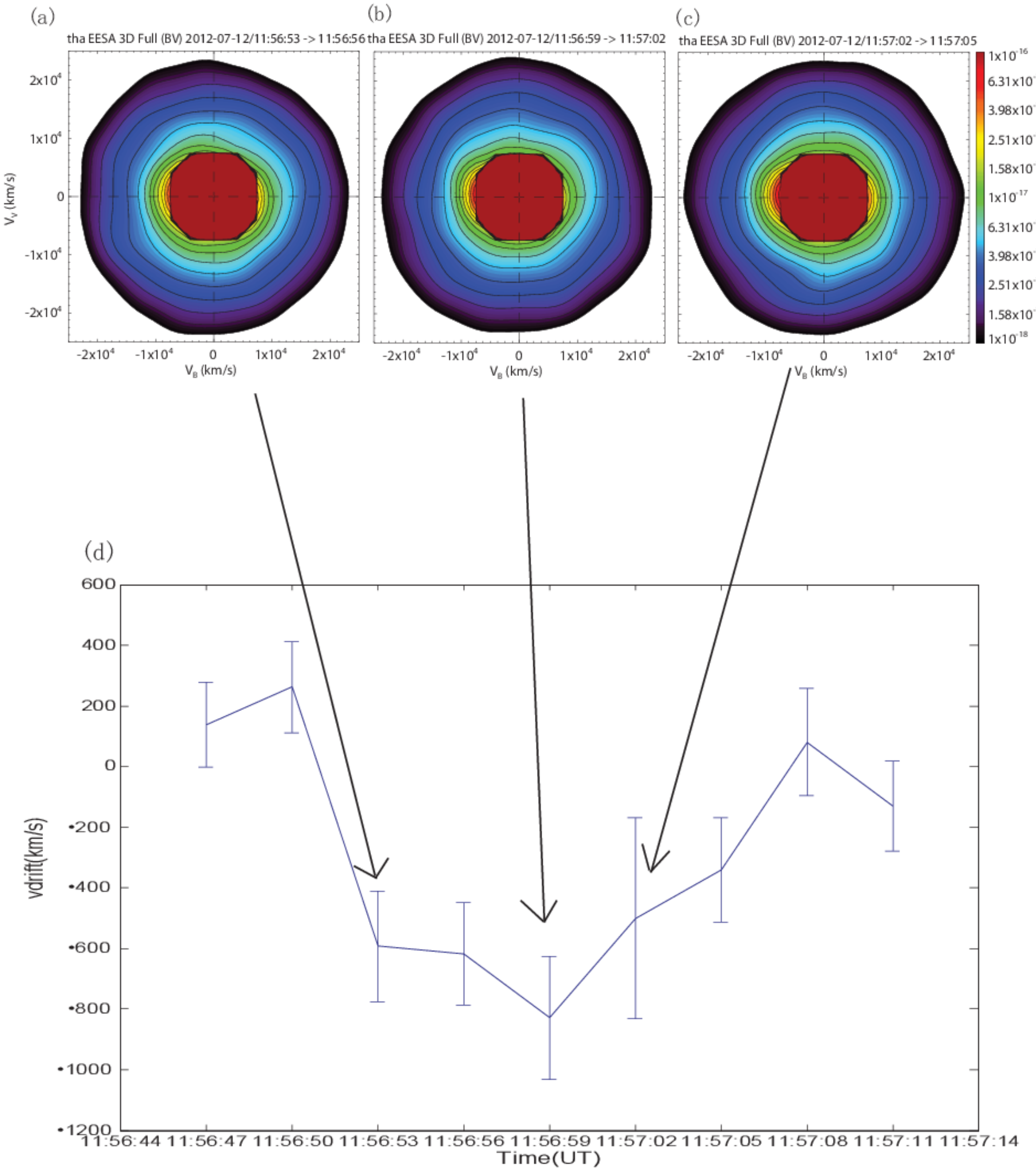

Figure 2.6. (a), (b), (c): observed electron distribution function at TH-A at three different time: 11:56:53 UT; 11:56:59 UT and 11:57:05 UT. The x axis of the slice is parallel to magnetic field and y axis is perpendicular to the magnetic field. The bulk flow velocity defines the x-y plane of the slice. Plot (d) is the fitted drift velocity of the cold electron population versus time (from 11:56:44 UT to 11:57:14 UT). The correspondence between three slices (a), (b), (c) and three different fitted drift velocities is marked by arrows.

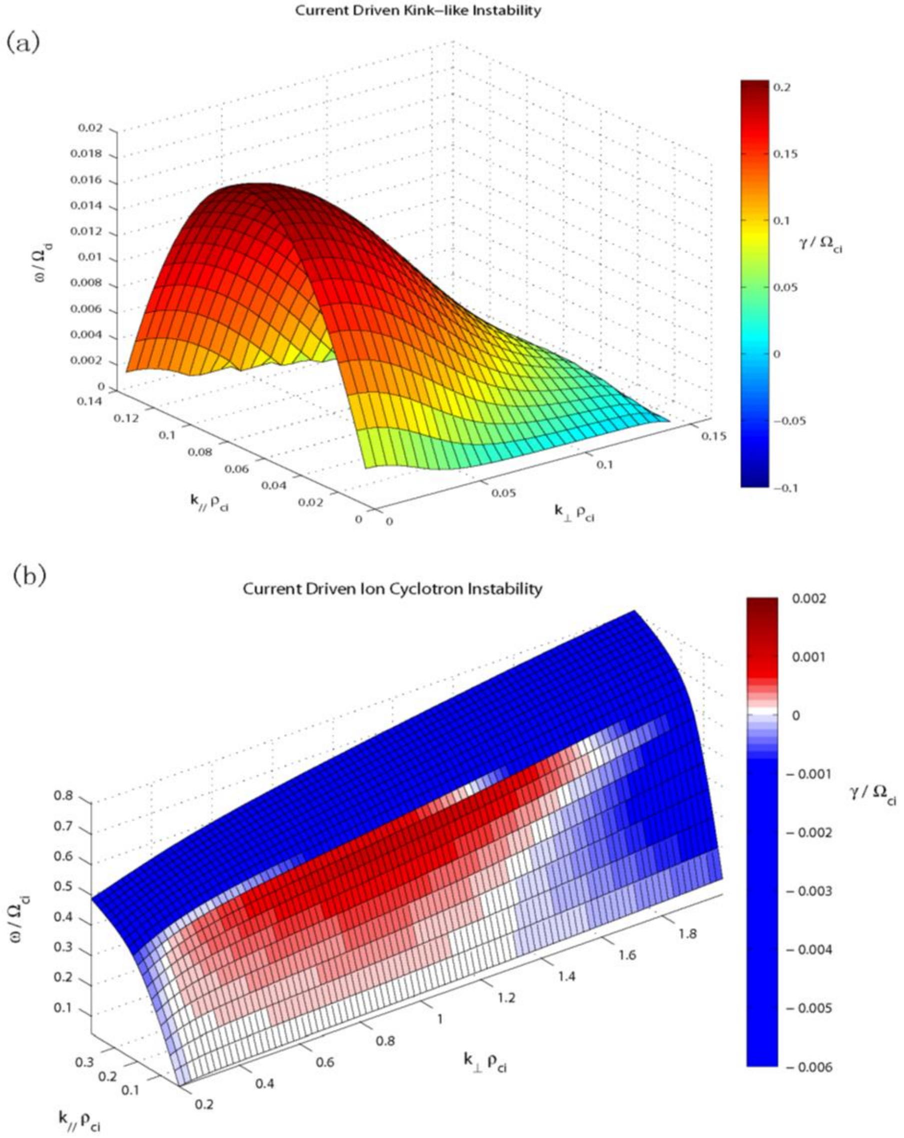

Figure 2.7. Dispersion surface for two different kinds of instabilities. (a) is for current driven kink like instability and (b) is for current driven ion cyclotron instability. The horizontal axes are normalized parallel and perpendicular wave vector ($k_{||}\rho_{ci}$ and $k_{\perp}\rho_{ci}$). The z axis is normalized wave frequency ω/Ω_{ci} . The normalized growth rate γ/Ω_{ci} is indicated by the color using color bar at right. For the current- driven ion cyclotron instability shown in Figure 2.7b, the red color indicates wave growth and the blue color damping.

Chapter 3

Whistler and electron firehose instability control of electron distributions in and around dipolarizing flux bundles

As discussed in Chapter 2, because the parallel current needed to excite current-driven ion cyclotron instability and kink-like instability are intense, these low frequency fluctuations are difficult to observe near dipolarization fronts. In Chapter 3 and Chapter 4, we focus on whistler mode waves, which are more frequently observed near dipolarization fronts. Our goal is to understand the potential effects of whistler waves on electron dynamics near dipolarization fronts. Adiabatic acceleration mechanisms (betatron and Fermi acceleration, as discussed in Section 1.3) have been suggested to energize electrons in the magnetotail. These acceleration mechanisms should result in perpendicular or parallel temperature anisotropy. Electron temperature anisotropies, however, have often been observed to be isotropic or weakly anisotropic and remain nearly unchanged throughout the magnetotail. The relaxation of electron's perpendicular and parallel temperature anisotropies could be caused by whistler instability and oblique electron firehose instability respectively. The effectiveness of these instabilities on regulating electron dynamics through wave scattering process in the magnetotail is investigated.

Utilizing 10 years of THEMIS satellite observations, we identified all whistler wave events near dipolarization fronts. In Section 3.1, we introduce whistler instability and oblique electron firehose instability. In Section 3.2 we describe our event selection criteria. In Section 3.3, we explore the occurrence probability and intensity of whistler instability and oblique electron firehose instability near dipolarization fronts, as function of electron anisotropy and plasma beta. Electron temperature anisotropies are well-constrained by the marginal stability conditions of these instabilities. Section 3.4 is our summary and discussions.

3.1 Introduction

Dipolarization fronts (DFs), transient dipolarizations characterized by a sharp increase in the northward component of the magnetic field, are frequently observed in the magnetotail [Nakamura et al., 2002; Ohtani, 2004; Runov et al., 2009, 2011; Liu et al., 2013a, 2013b, 2014]. They separate ambient plasma sheet plasma from the dipolarizing flux bundles launched by tail reconnection [Angelopoulos et al., 2008; Angelopoulos et al., 2013]. This phenomenon is closely related to substorms [Sergeev et al., 2009; Fu et al., 2013; Liu et al., 2015] and plays a crucial role in global electromagnetic energy conversion [Eastwood et al., 2010; Angelopoulos et al., 2013], where electromagnetic energy is dissipated at the fronts and converted to plasma energy. Adiabatic acceleration (betatron and Fermi acceleration) has been suggested to energize electrons at DFs [Fu et al., 2011; Ashour-Abdalla et al., 2011; Birn et al., 2014; Gabrielse et al., 2016]. These acceleration mechanisms should result in $T_{\perp,e}/T_{\parallel,e} > 1$ ($T_{\perp,e}/T_{\parallel,e} < 1$) due to magnetic field compression (shrinkage of a flux tube). Electron temperatures in the magnetotail, however, are often observed to be isotropic or weakly anisotropic [Walsh et al., 2011; Artemyev et al., 2014b]. The anisotropy relaxation mechanism of these accelerated electron populations near dipolarization fronts in the magnetotail is an open question. Addressing this question is important, because (1) electron populations accelerated at DFs are then transported into inner magnetosphere where their anisotropy generates electromagnetic waves which subsequently accelerate electrons up to MeV energies [Thorne, 2010]; and (2) anisotropic electron populations can significantly modify local currents in the magnetotail current sheet and drive global current instabilities [e.g., Karimabadi et al., 2004; Artemyev et al., 2016].

One of the possible mechanisms of electron temperature relaxation is electron scattering by electromagnetic waves. Indeed, various types of plasma waves are known to be present around DFs, including kinetic Alfvén waves, lower hybrid drift waves, whistler waves, electron cyclotron waves, etc [Le Contel et al., 2009; Zhou et al., 2009; Huang et al., 2012; Zhang et al., 2014; Zhang et al., 2017]. Some of these waves are excited by electron anisotropy instabilities, most notably the whistler instability and the electron firehose instability. Whistler waves, electromagnetic waves driven by energetic electrons with $T_{\perp,e}/T_{\parallel,e} > 1$, have been observed in the magnetotail for decades [Gurnett et al., 1976; Zhang et al., 1999 and references therein]. They have received substantial attention due to their important role in accelerating and scattering electrons [e.g., these waves are believed to contribute significantly in electron scattering to the diffuse aurora from the near-Earth magnetotail, see review by Ni et al., 2016]. The oblique electron firehose instability is excited when $T_{\perp,e}/T_{\parallel,e} < 1$. It is a non-propagating mode with zero real frequency; it resonates with electrons through cyclotron resonance [Li and Habbal, 2000; Camporeale and Burgess, 2008]. Several wave modes can be excited or amplified by this instability and the kinetic Alfvén wave is one candidate [Chen and Wu, 2010]. Both the whistler instability and the electron firehose instability yield growth of relatively short-wavelength enhanced magnetic field fluctuations; both types of fluctuations act to reduce the electron anisotropies through wave-particle scattering, setting boundaries on those anisotropies near the marginal instability thresholds. The general principle that wave-particle scattering due to electron-driven instabilities imposes anisotropy constraints has been demonstrated through particle-in-cell simulations of both the whistler instability [Gary & Wang, 1996; Gary et al., 2000] and the electron firehose instability [Gary and Nishimura, 2003; Hellinger et al., 2013], as well as observations in the magnetosheath [Gary et al., 2005] and the solar wind [Štverák et al., 2008; Bale et al., 2009]. If it is indeed a general result that electron anisotropy instabilities lead to anisotropy constraints throughout the collisionless plasmas of space, it becomes important to study this question in different plasma regimes such as the magnetotail.

3.2 Data and Event selection

THEMIS consists of five identical satellites (TH-A through TH-E) [Angelopoulos, 2008; Sibeck and Angelopoulos, 2008]. THEMIS's fluxgate magnetometer (FGM) [Auster et al., 2008] measures the low frequency magnetic field (<64Hz), and the search coil magnetometer (SCM) [Roux et al., 2008] measures the high frequency magnetic field (a few up to 4 kHz). The Electric Field Instrument (EFI) [Bonnell et al., 2008] measures the low and high frequency electric field (<8 kHz). We use waveform field data from these instruments, whenever available, to construct ground-computed spectra, but also rely on on-board computed spectral products as necessary. Data from SCM and EFI is passed into the Digital Fields Board to calculate the wave power spectral density of magnetic and electric fields using Fast Fourier Transforms (FFTs). They result in Filter Bank (FBK) and FFT data products, transmitted at various time and frequency resolutions [Cully et al., 2009]. Additionally, we use data from the electrostatic analyzer (ESA) that measures <30keV particles and the solid state telescope (SST) that measures >35keV particles to calculate particle moments [McFadden et al., 2008].

Liu et al., [2013a] built a list of DFs from the first few years of operation of the THEMIS mission. The most important criterion for their event identification is a sharp temporal increase in B_z ($\partial B_z/\partial t > 0.5 nT/s$ applied on three-point running averaged spin-fit data, and z is the northward component in geocentric solar magnetospheric, GSM, coordinates). In this paper, using the same methodology, we extended their event list to year 2017. A total of 2285 DF events from 2007 to 2017 were thus incorporated in our statistical study.

We investigated data within ±5 minutes around the DF, where t=0 is the time of B_z minimum preceding the DF-defining B_z rise. Based on the Liu et al. [2013a] and our DF event selection criteria, the time interval prior to the DF arrival must be relatively unperturbed. For all our events, we collected electron moments, including electron anisotropy and electron plasma beta (3s resolution, ESA and SST moment data were combined into a single joint data product) in this 10-minute time interval, regardless of whether waves are observed or not. Enhanced low-frequency magnetic and electric field fluctuations, likely driven by oblique electron firehose instability, are discussed in Section 3. Low-frequency broadband electromagnetic waves, often associated with KAWs, are always observed around DFs [see, e.g., Ergun et al., 2015; Malaspina et al., 2015; Breuillard et al., 2016], therefore the samples within our DF database were sufficient for studies of that phenomenon. However, since emissions of whistler waves are much more transient and narrowband than KAWs we constructed a separate, whistler database, a subset of the DF event samples, consisting of observations of discernible (and often intense) whistlers. In the following, we first concerned ourselves with the identification and properties of such narrowband whistler waves and then the broadband, lower frequency waves likely to be evidence of the firehose instability.

An example of both types of waves near dipolarization fronts is shown in Figure 3.1. The vertical dashed line in Figure 3.1(a) indicates the arrival of a dipolarization front at around 09:24 UT. Multiple fronts arrived at TH-D thereafter. Since dipolarization fronts are not isolated and often observed in groups, we selected only the leading DF of each DF group to construct our database, following the practice of Liu et al., [2013a].

Our whistler wave database selection criteria are as follows:

1. We constructed the magnetic field power spectrum, shown in Figure 3.1(c), using the combination of Fourier spectrum of waveform magnetic field data (128-samples-per-second during particle burst mode) and on-board magnetic field spectrum from FFT data. The former covers the frequency range from 1Hz to 64Hz and the latter lies in the frequency range from 64Hz to 4000Hz.

2. When the integrated magnetic field wave power from f_{lh} (lower hybrid frequency calculated from local magnetic field strength) to 64Hz is greater than $10^{-4}(nT)^2$; or when the integrated magnetic field power from 64Hz to f_{ce} (electron cyclotron frequency) is greater than $10^{-5}(nT)^2$, the sample was selected and included in our whistler wave database. Note that these thresholds are not arbitrary but a compromise between instrument noise and the minimum wave power of natural wave samples detectable in the respective band in our DF event database.

Vertical white bars with red borders on the top of Figure 3.1(c) mark the time intervals when whistler waves were identified, during which there were clear enhancements of magnetic field wave power between f_{lh} and f_{ce}.

We look specifically into two time intervals when wave burst modes (8296-samples-per-second waveform magnetic field data) are available. Between 09:26:15UTC and 09:26:18UTC, the magnetic field power spectrum in Figure 3.1(g) clearly shows a bump in the frequency range between f_{lh} and f_{ce} at around 150Hz. Monochromatic wave signatures with dominant components in the direction perpendicular to the ambient magnetic field shown in Figure 3.1(e), and predominantly right-hand circular or elliptically polarized (not shown) provide additional evidence for the existence of whistler waves in this time interval.

Between 09:26:52UT and 09:26:55UT when an enhancement of magnetic field wave power between f_{lh} and f_{ce} was identified, the magnetic and electric field power spectra in Figure 3.1(h) show no clear bumps between f_{lh} and f_{ce} and the magnetic field waveform in Figure 3.1(f) is rather non-coherent and non-monochromatic. The broadband electromagnetic waves observed here are clearly not whistler waves, despite the fact that the integrated magnetic field wave power is larger than our whistler wave selection threshold and resides in the frequency range f_{lh} and f_{ce}. Doppler-shifted kinetic Alfvén waves (KAWs), frequently observed during intervals of fast plasma sheet flows, could be a candidate for the broadband electromagnetic waves shown here [Chaston et al., 2012]. To explore further this hypothesis, we plot $E_{\perp}/(V_A B_{\perp})$, the ratio of perpendicular electric to magnetic field amplitudes normalized to the local Alfvén velocity, in Figure 3.1(i). The over-plotted solid red line is the theoretical expectation for KAWs, $E_{\perp}/B_{\perp} = V_A(1 + k_{\perp}^2 \tilde{n}_i^2)/\sqrt{1 + k_{\perp}^2(\tilde{n}_i^2 + \tilde{n}_s^2)}$, where $\tilde{n}_i^2$ is the ion gyroradius and $\tilde{n}_s^2$ the ion acoustic gyroradius [Stasiewicz et al., 2000]. To compare the theoretical value with observations, we assumed that the wave frequency observed in the spacecraft frame is mainly due to the Doppler-shift of KAWs by the plasma flows ($\omega_{sc} \approx k v_f$, where ω_{sc} is the observed frequency in the spacecraft frame and v_f is the plasma velocity), a reasonable assumption, since the frequency of KAWs in the plasma frame is much smaller than the ion gyrofrequency. It is evident from Figure 3.1(i) that the E-to-B ratio expected from theory is quite consistent with observations. Thus, Doppler-shifted KAWs are a good candidate for the broadband electromagnetic waves in our DF event database, and even within our whistler wave sample database (when the frequency of KAWs is Doppler-shifted above f_{lh} and wave power is larger than our whistler wave selection threshold). This broadband wave type, associated with KAWs and likely to be evidence for the oblique electron firehose instability is discussed in section 3.3. Our whistler sample database, discussed in next section, assumes that the narrowband waves (those with clear bumps in the magnetic field power spectrum, such as the case shown in Figure 3.1(f)), are likely whistlers. They were detected in 1417 (62%) of the 2285 events in our DF database.

3.3 Results

Figures 3.2(a) and 3.2(b) show the data distribution in electron temperature anisotropy - electron parallel beta space (logarithmic scale), before and after the DFs, respectively. All 3sec data samples at +/- 5min around the DF are included. This distribution of the number of points per unit bin size is proportional to the probability density distribution of the measurements. The two prominent boundaries in this space match well the over-plotted dashed lines, depicting $\frac{T_\perp}{T_{||}} - 1 = \frac{a}{\beta_{||}^{b}}$, the marginal instability thresholds of the whistler instability (top line, for a=0.21 and b=0.58 taken from Gary et al. [2012]) and of the oblique electron firehose instability (bottom line, for a= -1.29 and b=0.97 taken from Gary and Nishimura [2003]). That the probability distributions conform to these boundaries suggests that the electron anisotropy around DFs is well constrained by these instabilities. This implies that electron acceleration at DFs indeed produces electron populations that exceed marginal stability thresholds, converting their free energy to waves, which in turn interact efficiently with the electrons ultimately limiting their anisotropisation. Thus wave-particle interactions shape the electron distributions over a broad region surrounding the DFs and must be accounted for any electron acceleration model by dipolarizing flux bundles.

Next, we employ our whistler wave samples database described in the previous section (a subset of samples of the DF plasma parameter database discussed in the previous paragraph), to study the occurrence rate of those (narrowband) whistlers in the vicinity of DFs. Figures 3.2(c) and 3.2(d) show the occurrence rate of whistler waves in that space (the number of samples where whistlers were detected over the total number of samples in each bin), before and after the DFs, respectively. This rate increases significantly near the marginal instability threshold of the whistler instability, both before and after the DFs. This demonstrates that most narrowband whistlers are observed in plasmas near marginal stability, therefore this mode plays an important role for moderating the anisotropy produced by electron acceleration at DFs. We also note that whistler wave phase speeds exceed both typical DF speeds and electron drift speeds. By depositing some of their wave energy back to the electrons around DFs, whistlers render local electron heating more efficient than in the absence of wave-particle interactions, and wave transport of energy less pronounced. However, it is still possible that DF-generated whistlers can emit significant energy far away from DFs in the form of Poynting flux, similar to the case of shock waves [e.g., Sundkvist et al., 2012; Wilson 2016]. This is something that needs to be investigated in the future.

In order to provide further observational evidence for the operation of the electron firehose instability on the electron temperature anisotropy, we collected magnetic and electric field wave parameters at different frequency ranges and divided them into two datasets: before the DF and after the DF. We calculated the root-mean-squared (RMS) amplitude of magnetic field fluctuations, in the range 0.33Hz - 2Hz, using FGL data (4-samples-per-second) in each spin period (3 seconds), and normalized it to the ambient magnetic field strength, B_0. For B_0 = 10nT, typical in the central plasma sheet near THEMIS's apogees, the ion cyclotron frequency is 0.15Hz and the lower hybrid frequency is 6.5Hz. Thus, the selected frequency range ([0.33Hz, 2Hz]) lies roughly above f_{ci} and well below f_{lh}. Figures 3.3(a) and 3.3(b) show the result in electron anisotropy-parallel beta space. Although the fluctuations near the marginal instability threshold of the whistler instability (top dashed lines) dominate in these plots, especially behind DFs (Figure 3.3(b)), and will be addressed later, it is also evident that fluctuations are enhanced near the marginal instability threshold of the electron firehose instability (bottom dashed lines), in particular before DFs (Figure 3.3(a)) which is evidence that the oblique electron firehose instability is excited and restrains the electron parallel temperature anisotropy when $T_{\perp,e}/T_{\parallel,e} < 1$. Moreover, fluctuations near the marginal instability thresholds of the whistler instability and the oblique electron firehose instability are much stronger after the DFs in Figure 3.3(b) compared with fluctuations before the DFs in Figure 3.3(a).

Figures 3.3(c) and 3.3(d) show the ratio of perpendicular low frequency magnetic field fluctuations to the total magnetic field fluctuations, $\delta B_{\perp}/\sqrt{\delta B_{\perp}^2 + \delta B_{||}^2}$ ($\delta B_{||}$ and $\delta B_{\perp}$ are the magnetic fluctuations along and across the ambient magnetic field). That perpendicular fluctuations dominate near the marginal instability threshold of electron firehose instability is in agreement with the polarization property of this instability [Gary and Nishimura, 2003]. Note that the firehose instability can be responsible for the excitation/amplification of different kinetic wave modes, particularly, kinetic Alfvén waves observed around DFs [Chen and Wu, 2010], consistent with our case-studies (such as that in Section 3.2, showing that the waves can be considered Doppler-shifted KAWs in the range between f_{ci} and f_{lh} examined here).

Figures 3.3(e) and 3.3(f) show the ratio $c\delta B_\perp/\delta E_\perp$ which provides a good estimate for the wave refractive index. For a small wave number and a Doppler-shifted frequency above f_{ci}, $\delta E_\perp/\delta B_\perp$ for KAW is about 10 to 100 times the local Alfvén velocity (see Figure 3.1(i), for instance). Given an Alfvén velocity of about 300km/s, $c\delta B_\perp/\delta E_\perp$ for KAW is on the order of 10 to 100, which agrees with our observational values for the waves near the marginal instability threshold of the firehose instability in Figures 3.3(e) and 3.3(f).

Conversely, compressional magnetic field fluctuations are enhanced near the marginal instability threshold of the whistler instability in this low frequency (f_{ci} - f_{lh}) regime (see Figures 3.3(c) and 3.3(d)). A possible reason could be magnetosonic waves or lower hybrid waves that are excited by other unstable plasma distributions (mostly likely ions), but are further amplified due to resonant interaction with electrons when $T_{\perp,e}/T_{\parallel,e} > 1$. However, we cannot exclude that these compressional waves are exited independent of electrons within the same spatial region as whistler waves (around DFs, see Khotyaintsev et al., 2011), and thus appear only coincidentally in the same region in the anisotropy-beta parameter space as the marginal instability threshold of the whistler instability. This remains an area of future investigation.

Next, we explored the low frequency portion of the whistler range (f_{lh} - f_{ce}) where electric and magnetic field waveforms were routinely available. Specifically, we used search-coil waveform data in Particle Burst mode (128-samples-per-second), high-pass filtered above f_{lh}, and averaged its RMS amplitude in every spin (3s) to obtain δB in the range f_{lh} - 64Hz (normalized to the spin-fit magnetic field, B_0). This frequency range is in the whistler range, but because it is below 64 Hz it can always be produced from ground-processed waveforms which are routinely available in an extended period surrounding DFs (Particle Burst mode lasts 8-12min encompassing the DF). Figures 3.3(g) and 3.3(h) show the normalized magnetic field fluctuations in this frequency range, before and after the DFs. We see that these fluctuations are enhanced significantly near the marginal instability threshold of the whistler instability, as expected from examination of narrowband whistlers (Figure 3.2(c), 3.2(d)). However, the wave power increases over a broad range in $T_{\perp,e}/T_{||,e}$ between the dashed lines, down to the marginal instability threshold of electron firehose instability, and this may be related to low frequency waves driven by the electron firehose instability that have been Doppler-shifted above f_{lh}. The dominant wave power is in the perpendicular direction near both marginal instability curves (both before and after the DFs, Figures 3.3(i) and 3.3(j)), suggesting that both modes can operate in this frequency regime depending on the nature of the electron distributions. In fact, the perpendicularity peaks near the two instability thresholds (both top and bottom curves), providing additional observational evidence for whistler and (likely Doppler-shifted) firehose instabilities in this frequency regime. The refractive index near the whistler marginal instability regime, as shown in Figures 3.3(k) and 3.3(l) agrees well with cold plasma theory ($n = c\delta B/\delta E$) for field-aligned whistler waves which, for typical magnetotail parameters, is on the order of $10 - 10^2$.

3.4 Summary and conclusions

Our results are based on waves observed both before and after DFs from 10 years of THEMIS observational data. The wave data are organized quite well in an electron anisotropy-parallel beta parameter space with sharp boundaries near the marginal instability conditions for whistler and electron firehose instabilities, providing strong evidence of the presence of those waves and their operation on electrons near DFs. Enhancement of the occurrence rates and perpendicular wave power near the marginal stability thresholds of these instabilities, and consistency of the observed refraction index with the theoretical refraction index of those instabilities provide additional supportive evidence for the operation of those instabilities on electron dynamics in the magnetotail near dipolarization fronts.

Dipolarization fronts are boundaries in dynamic environments with various instabilities identified in their vicinity. The effects of these instabilities on particle dynamics, however, are poorly understood. Our findings provide direct observational evidence on the regulation of electron acceleration at dipolarization fronts by wave-particle interactions. Whistler instabilities driven by electrons with $T_{\perp,e}/T_{\parallel,e} > 1$ near the fronts are capable of interacting with electrons effectively, gaining free energy from the temperature anisotropy and constraining electron distributions to the marginal instability threshold of the whistler instability through pitch angle scattering process. Sufficiently large $T_{\perp,e}/T_{\parallel,e} < 1$ favors the excitation of electron firehose instability, which, in turn, interacts with electrons and scatters them to the marginal instability threshold of that instability.

Our results reveal the importance of wave-particle interactions in the magnetotail near dipolarization fronts and potential effects of those interactions on global energy conversion. Despite the short duration of dipolarizing flux bundles (~ 1min), waves are still proven to be capable of interacting with electrons and modulating their distribution functions. Future investigations of electron dynamics near dipolarization fronts should recognize that adiabatic interactions alone are not sufficient to predict electron anisotropy evolution. Rather, wave-particle interactions should be incorporated when modeling electron dynamics in the magnetotail.

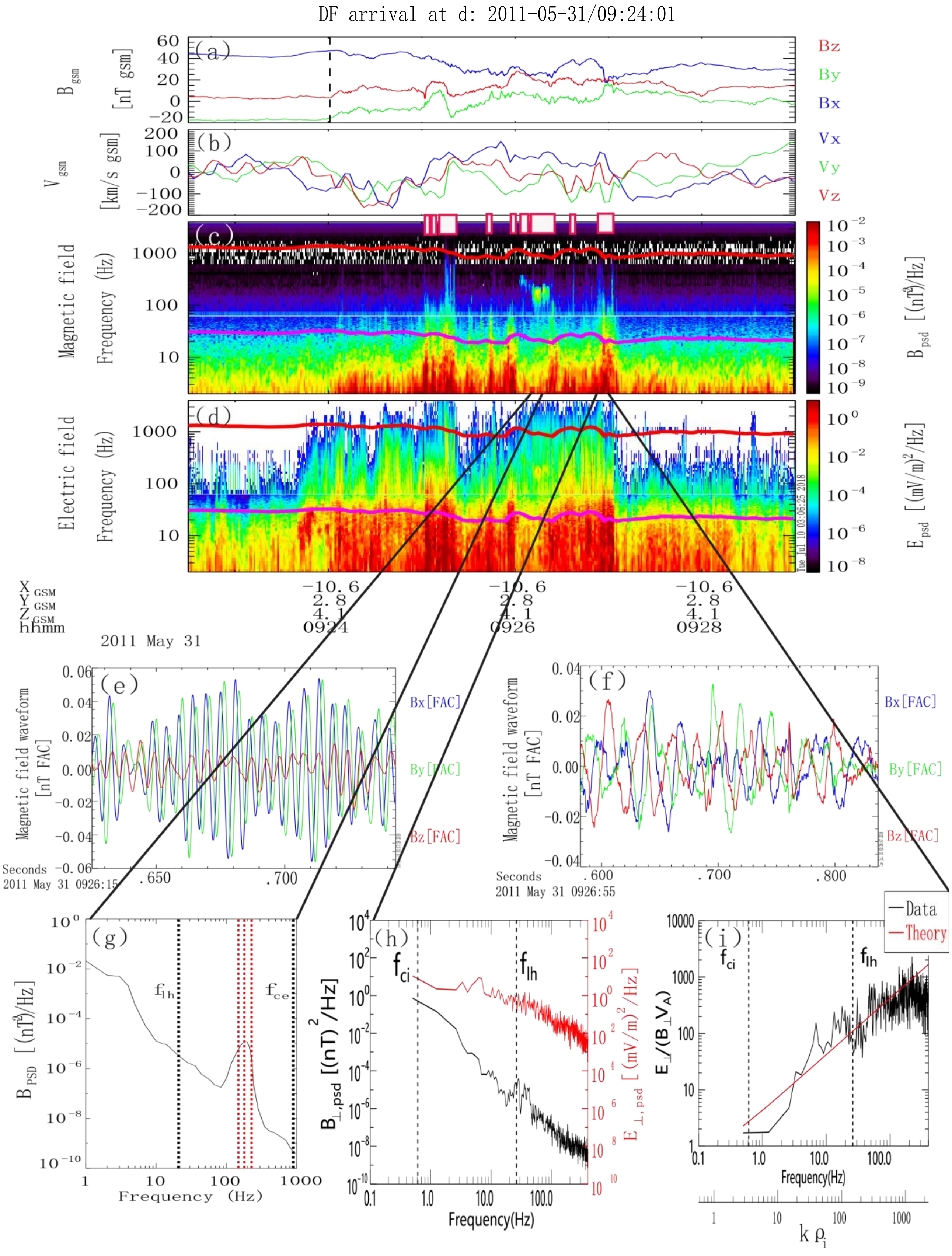
DF arrival at d: 2011-05-31/09:24:01
(a)
B_{gsm} [nT gsm]
Bz
By
Bx
(b)
V_{gsm} [km/s gsm]
Vx
Vy
Vz
(c)
Magnetic field Frequency (Hz)
B_{psd} [(nT)^2/Hz]
(d)
Electric field Frequency (Hz)
E_{psd} [(mV/m)^2/Hz]
X_{GSM} -10.6 -10.6 -10.6
Y_{GSM} 2.8 2.8 2.8
Z_{GSM} 4.1 4.1 4.1
hhmm 0924 0926 0928
2011 May 31
(e)
Magnetic field waveform [nT FAC]
Bx[FAC]
By[FAC]
Bz[FAC]
Seconds 2011 May 31 0926:15
(f)
Magnetic field waveform [nT FAC]
Bx[FAC]
By[FAC]
Bz[FAC]
Seconds 2011 May 31 0926:55
(g)
B_{PSD} [(nT)^2/Hz]
f_{lh}
f_{ce}
Frequency (Hz)
(h)
$B_{\perp,psd}$ [(nT)^2/Hz]
$E_{\perp,psd}$ [(mV/m)^2/Hz]
f_{ci}
f_{lh}
Frequency(Hz)
(i)
Data
Theory
$E_{\perp}/(B_{\perp}V_A)$
f_{ci}
f_{lh}
Frequency(Hz)
k ρ_i

Figure 3.1: Overview plot to illustrate whistler wave selection criteria. Figure 3.1(a) and 3.1(b): Magnetic field and ion velocity measurements in GSM (geocentric solar magnetospheric) coordinate system; Black dashed line in Figure 3.1(a) marks the time when dipolarization front arrived at TH-D; Figure 3.1(c) and 3.1(d): Magnetic field power spectrum and electric field power spectrum. Magenta line indicates the lower hybrid frequency (f_{lh}) and red line indicates the electron cyclotron frequency (f_{ce}). Vertical white bars with red borders on top of Figure 3.1(c) indicate the time intervals when whistler waves are identified. Figure 3.1(e) and 3.1(g) focus on the time interval between 09:26:15UT and 09:26:18UT: Figure 3.1(e) shows the magnetic field waveform data after bandpass filtering between f_{lh} and f_{ce}. The magnetic field data is in FAC (field-aligned coordinate system) while Z_{FAC} points to the direction parallel to the ambient magnetic field. Figure 3.1(g) shows the magnetic field power spectrum during this time interval. Two black vertical dashed lines indicate f_{lh} and f_{ce}. Three red vertical dashed lines indicate the central frequency of whistler emission, lower and upper frequency of whistler emission (when magnetic field power spectral density, PSD, drops to a half of its the peak value). Figures 3.1(f), 3.1(h) and 3.1(i) focus on the time interval between 09:26:52UT and 09:26:55UT. Figure 3.1(f) shows the magnetic field in FAC after bandpass filtering between f_{lh} and f_{ce}. Figure 3.1(h) shows the magnetic field PSD in perpendicular direction in black and electric field PSD in perpendicular direction in red. Figure 3.1(i) shows the ratio of perpendicular electric field fluctuations to perpendicular magnetic field fluctuations, normalized to local Alfvén velocity. Black line is from observational data and red line is from theoretical values for KAWs.

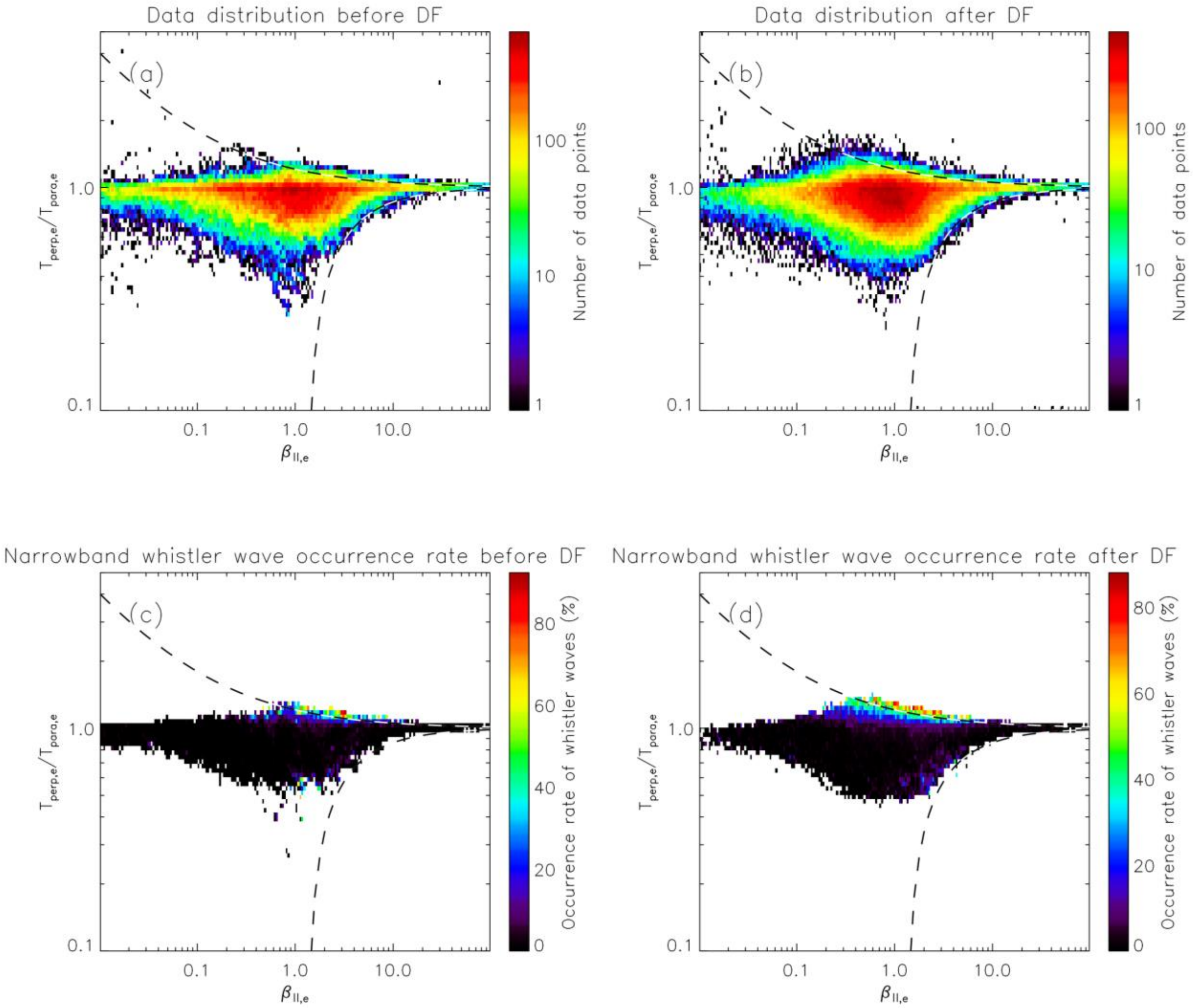

Figure 3.2: Horizontal axis is log electron parallel beta and vertical axis is log electron temperature anisotropy ($T_{\perp,e}/T_{||,e}$) in all four panels. Two dashed lines in each panel indicate the marginal instability threshold of the whistler instability (top, $T_{\perp,e}/T_{||,e} > 1$) and electron firehose instability (bottom, $T_{\perp,e}/T_{||,e} < 1$). (a) and (b): Number of data points in each log-log bin before dipolarization fronts and after dipolarization fronts, respectively. (c) and (d): Occurrence rate (%) of narrowband whistlers before DF and after DF, respectively. Bins with fewer than 10 data points are suppressed to avoid large statistical errors stemming from small numbers.

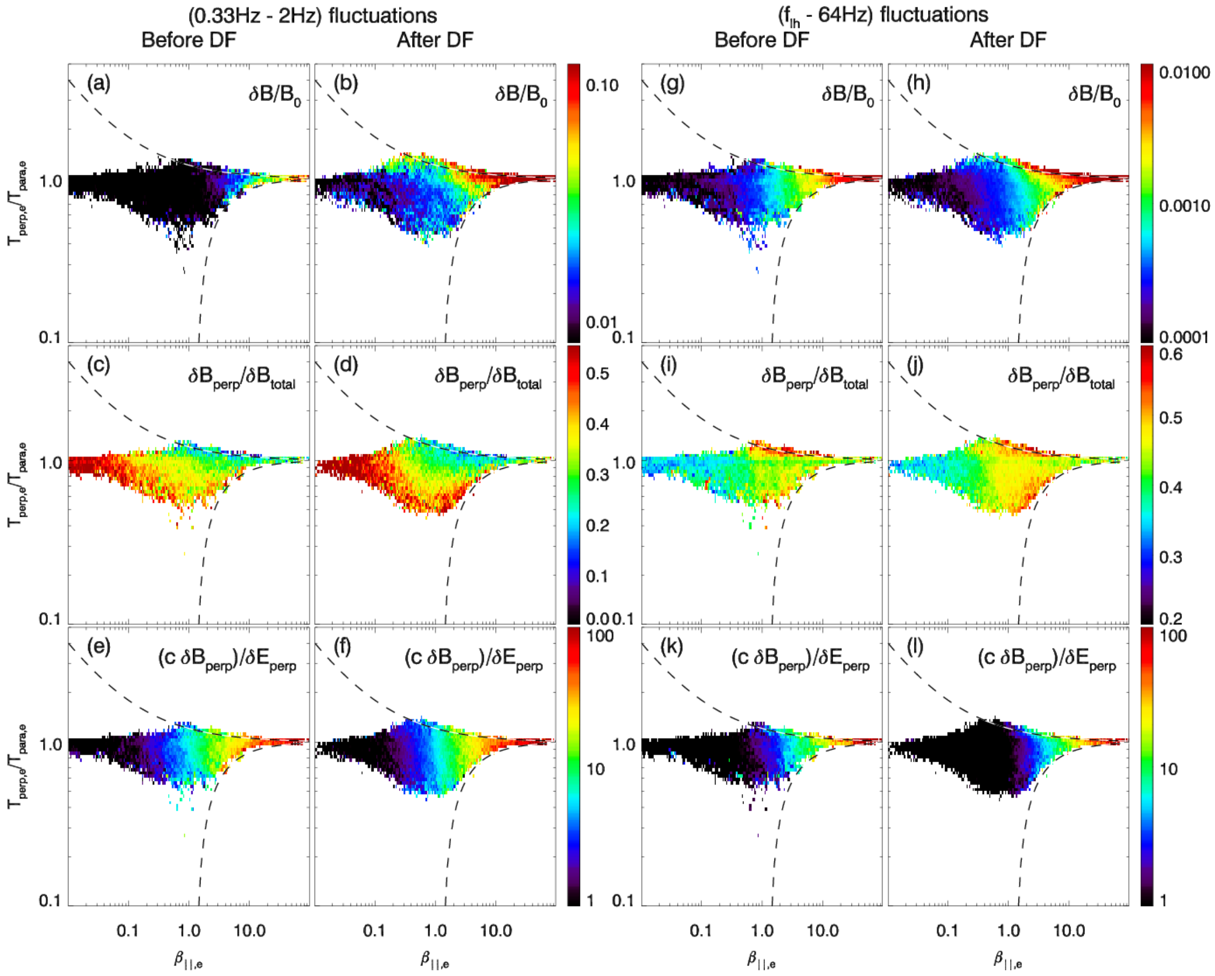

Figure 3.3: Horizontal and vertical axes are same as in Figure 3.2. Panels (a - f) at left: fluctuations at frequency range: (0.33-2Hz); Panels (g-l) at right: fluctuations at frequency range: (f_{lh}-64Hz). Plotted quantities are self-explanatory and discussed further in text. Data bins with fewer than 10 data points have been suppressed to avoid noise from statistics of small numbers.

Chapter 4

Energy transport by whistler waves around dipolarizing flux bundles

During the earthward transport of electrons to more dipolar regions by DFBs, electrons should gain more perpendicular energy than parallel energy, resulting in larger perpendicular electron temperature anisotropy closer to Earth. Electron temperature anisotropies, however, have often been observed to remain nearly unchanged, slightly field aligned, throughout the magnetotail. The dissipation of electron perpendicular energy during the earthward transport remains an open question. In previous chapter, we emphasize the importance of whistler waves in reducing electron perpendicular temperature anisotropies through wave-particle scattering process. In this chapter, we reveal the importance of whistler waves energetically by radiating perpendicular electron energy flux in the form of Poynting flux. Combining the results in Chapter 3 and in this chapter, we demonstrate that whistler waves play an important role in electron dynamics in the magnetotail by significantly modifying the otherwise adiabatically-shaped electron distributions.

Using the whistler wave event database established in Chapter 3, we performed a statistical study of electron observations associated with whistler waves near DFBs and whistler wave Poynting flux. In Section 4.1, we briefly introduced whistler waves. In Section 4.2 we describe the instrumentation and event selection criteria used. In Section 4.3 our results are presented in two parts. Part 1 is an investigation of the electron population that generates whistler waves. Part 2 is an evaluation of the relative importance of whistler wave Poynting flux and the energy contained in the electron distributions, which are potentially in cyclotron resonance with these waves. Section 4.4 summarizes our findings and discusses their implications.

4.1 Introduction

Rapid earthward plasma flows known as bursty bulk flows (BBFs) play an important role in earthward transport of mass, energy, and magnetic flux through the magnetotail plasma sheet [Baumjohann et al., 1990; Angelopoulos et al., 1992, 1994; Ohtani, 2004]. Dipolarized flux tubes referred to as dipolarizing flux bundles (DFBs) [Liu et al., 2013a, 2013b, 2014] or flux pileup region [Khotyaintsev et al., 2011; Fu et al., 2012c] are frequently observed within BBFs. A sharp rise in the northward component of the magnetic field, characteristic of an intense current sheet ahead of an approaching DFB, is referred to as a dipolarization front (DF) [Nakamura et al., 2002; Runov et al., 2009, 2011; Fu et al., 2012b]. Observations and simulations have shown that DFBs contain much hotter, more energetic electrons than the ambient plasma sheet [Fu et al., 2011, 2019; Liu et al., 2013b; Birn et al., 2014; Lu et al., 2016]. These energetic electrons could be hot, anisotropic electrons injected toward the inner magnetosphere [Sergeev et al., 1999; Gabrielse et al., 2014, 2016; Xu et al., 2018]. Because the electron temperature increases within DFBs are proportional to the ambient magnetic field, B_z [Runov et al., 2015], adiabatic acceleration caused by magnetic compression could be a major mechanism for DFB electron heating [Fu et al., 2011; Birn et al. 2014]. If this process operates during DFBs' earthward transport of electrons to more dipolar regions, electrons should gain more perpendicular energy than parallel energy, resulting in larger perpendicular electron temperature anisotropy closer to Earth. Electron temperature anisotropies, however, have often been observed to remain nearly unchanged, slightly field aligned, throughout the magnetotail [Walsh et al., 2011; Artemyev et al., 2013]. So how is perpendicular electron energy dissipated during earthward electron transport? It is important to investigate this because at their final stage of interaction with Earth's dipolar region, these pre-accelerated electrons can be a source population for electromagnetic wave generation in the inner magnetosphere, affecting the radiation belts [Thorne, 2010].

Dissipation of perpendicular electron energy and reshaping of the electron distributions are thought to be caused both by electromagnetic wave generation [e.g., Gary 1993; and references therein] and by nonadiabatic particle scattering due to field-line curvature [see investigation of this mechanism for DFBs in e.g., Eshetu et al., 2018]. Here we provide observational evidence supporting electromagnetic wave generation as an important mechanism around DFBs. Dipolarization fronts are very dynamic environments with different types of waves identified within them, including lower hybrid drift waves, whistler waves, and electron cyclotron waves. [Le Contel et al., 2009, 2017; Sergeev et al., 2009; Zhou et al., 2009; Zhang and Angelopoulos, 2014; Yang et al., 2017]. Whistler waves, which scatter electrons in velocity space, can also reduce electron perpendicular temperature anisotropy and thus evacuate available electron free energy from the environment surrounding the DFBs. Simulations and observations have shown that electron perpendicular temperature anisotropy ($T_{\perp,e}/T_{\parallel,e} > 1$, where $\perp$ and $\parallel$ denote directions perpendicular and parallel to the ambient magnetic field) is a significant free energy source for whistler wave excitation [Vedenov and Sagdeev, 1961; Kennel, 1966; Li et al., 2009a; Santolík et al., 2010a]. In the linear stage of excitation, whistler waves grow rapidly, and perpendicular electron energy decreases after being transferred from the electrons to the waves. Eventually, electron distributions relax to a marginal stability state [Gary & Wang, 1996; Gary et al., 2000; Fu et al., 2012a; Yue et al., 2016; An et al., 2017; Tao et al., 2017]. In our previous statistical study

(Zhang et al., [2018]), we showed that whistler waves, which are frequently observed near DFBs, are likely capable of regulating electron dynamics very effectively, because the simultaneously observed electron perpendicular anisotropies are constrained at or below the marginal stability threshold. After their excitation, those whistler waves will likely transport their electromagnetic energy in the form of Poynting flux along the magnetic field and away from the central plasma sheet towards the ionosphere. Because whistler waves occur frequently and reduce electron perpendicular anisotropy near DFBs very effectively, their role in evacuating electron perpendicular energy near DFBs is likely important.

4.2 Data and Methodology

THEMIS consists of five identical satellites (TH-A through TH-E) equipped with field and plasma instruments [Angelopoulos, 2008; Sibeck and Angelopoulos, 2008]. The THEMIS Fluxgate Magnetometer (FGM) measures direct-current magnetic field data [Auster et al., 2008]. The Search Coil Magnetometer (SCM) and Electric Field Instrument (EFI) measure magnetic and electric field waveforms [Bonnell et al., 2008; Roux et al., 2008]. Data from SCM and EFI processed onboard the satellites by the Digital Fields Board (DFB) provide Filter Bank (FBK) and Fast Fourier Transform (FFT) quantities [Cully et al., 2008]. The THEMIS electrostatic analyzer (ESA) measures particle distributions at energies lower than 30 keV [McFadden et al., 2008]. The Solid State Telescope (SST) measures plasma data at energies higher than 30 keV [Angelopoulos, 2008]. From a combination of waveform magnetic and electric field data and FFT data, we identified whistler waves and calculated their Poynting flux. Using combined ESA and SST data with 3-second time cadence and full angular resolution, we did a statistical study of electrons that could be responsible for whistler wave generation.

Using all THEMIS observations from 2007 through 2017, we augmented the DFB event list of Liu et al. [2013a] (with identical selection criteria) to incorporate magnetotail crossings from 6 additional years of operation, a 2.5 times increase of the original database. The most important characteristic of DFB events is a sharp increase in B_z ($\partial B_z/\partial t > 0.5\ nT/s$) associated with the DF that precedes them. The DF convective velocity, used later in this paper, is calculated as the average of $\boldsymbol{V}_{DF} = \boldsymbol{E} \times \boldsymbol{B}/B^2$ over the DF thickness. (Details on how to calculate the convective velocity for each DF event can be found in Liu et al. [2013a].)

We identified all whistler wave events in the extended DFB event list (Zhang et al., [2018]); the same wave event database is used here. For completeness, we outline the main principles of our wave selection procedure. When the magnetic field wave power integrated from f_{lh} (the lower hybrid frequency calculated from the local magnetic field strength) to f_{ce} (the electron cyclotron frequency) was greater than a threshold value, the datum was included in our whistler wave database. The upper and lower frequencies in each whistler wave data sample were selected from frequencies in which the magnetic field power spectral density fell below one half its peak. Using magnetic and electric field waveforms (128-samples-per-second in “particle burst” data collection mode), we calculated the spectral density of the three components of the Poynting vector **S** in a field-aligned coordinate system in which Z is the magnetic field direction and X and Y are orthogonal to Z and to each other [Santolík et al., 2010b; Li et al., 2013]. After integrating the power spectral density of the Z-component of the Poynting vector from its lower to its upper frequency for each whistler wave data sample, we obtained the whistler wave parallel Poynting flux for further use in our statistical study.

4.3 Results

Figure 4.1 illustrates the calculated whistler wave Poynting flux and electron energy flux related to anisotropy (associated with the electron free energy) at different energies. The arrival of a dipolarization front measured by TH-D at 03:04:56 UT (Figure 4.1(a)) is accompanied by fast, predominantly earthward plasma sheet flows (Figure 4.1(b)). The dipolarization front's convective velocity in the X_{GSM} and Y_{GSM} directions is 98 km/s and -132 km/s, respectively. Figure 4.1(c) shows the magnetic field power spectrum (a ground-processed Fourier spectrum of waveform magnetic field data and an onboard magnetic field spectrum from FFT data combined). White boxes with red borders indicate the time intervals during which whistler waves were identified. Figure 4.1(d) illustrates the power spectral density of the Poynting vector parallel to the ambient magnetic field in the 2 Hz to 64 Hz frequency range. Figure 4.1(e) shows the electron phase space density anisotropy, $f_{\perp}/f_{||}$ (where $f_{\perp}$ is the electron phase space density in the direction perpendicular to the magnetic field and $f_{||}$ is the phase space density parallel to the magnetic field) at energies from tens of eV to hundreds of keV. The solid black line in Figure 4.1(e), the minimum resonant energy, is calculated from the cyclotron resonance condition below:

$$\omega - k_{\parallel} v_{\parallel} = \frac{|\Omega_{ce}|}{\gamma} \tag{4.1}$$

where ω is the wave frequency, Ω_{ce} is the electron cyclotron frequency calculated from the local magnetic field strength, and $\gamma = (1 - v^2/c^2)^{1/2}$ is the relativistic factor. After obtaining the wave frequency ω and the wave normal angle from observations (wave normal angle is calculated by performing wave polarization analysis on magnetic field data), we calculated the wave vector

$k_{\parallel}$ using the cold plasma dispersion relation [Stix 1962]. The electron velocity parallel to the magnetic field is calculated using equation (4.1), and we obtained the minimum resonant energy $E_{min,res}$ shown in Figure 4.1(e). That energy, several keV in this DFB event, is clearly associated with the energy boundary of the perpendicularly anisotropic (red in Figure 4.1(e)) electron population observed simultaneously with whistler waves behind the DF.

Figure 4.1(f) compares the whistler wave parallel Poynting flux (blue) with the electron energy flux (red). The latter is defined as the product of δP_e and V_{DF}. The difference between the electron perpendicular pressure and the parallel pressure above the minimum resonant energy, δP_e , is calculated using the equation below:

$$\delta P_e = \int_{E_{min,res}} f(v_{\perp}, v_{\parallel})\, v_{\perp} v_{\perp} dv_{\perp} dv_{\parallel} - \int_{E_{min,res}} f(v_{\perp}, v_{\parallel})\, v_{\parallel} v_{\parallel} dv_{\perp} dv_{\parallel} \qquad (4.2)$$

where $v_{\perp}$ and $v_{\parallel}$ are electron velocities perpendicular and parallel to the magnetic field, and $f(v_{\perp}, v_{\parallel})$ is the electron phase space density. The amount of free energy available for whistler wave generation is δP_e; the DF convective velocity is V_{DF}. The whistler wave Poynting flux $S_{\parallel}$ is highly correlated with the electron energy flux $\delta P_e \cdot V_{DF}$ in Figure 4.1(f). Figure 4.1(g) shows the ratio between $S_{\parallel}$ and $\delta P_e \cdot V_{DF}$, which can be up to 10% in this event.

Now let us reveal which electron population generated the whistler waves that transported so significant an amount of free energy. Figure 4.2 is a superposed epoch analysis of the whistler wave parallel Poynting flux (Figure 4.2(a)) and the median values of electron phase space density anisotropy, $f_{\perp}/f_{||}$, as a function of energy (Figure 4.2(b)) or normalized energy (Figure 4.2(c-e)) when whistler waves were observed. Only samples taken within 5 minutes before and after DF arrival were included. (We used electron measurements only when they exceeded the one-count level and the electrons' energies were higher than twice the spacecraft potential.) The Poynting flux increased significantly after DF arrival. The median minimum resonant energy for the observed whistler waves (black line in Figure 4.2(b)) was consistently around 7keV throughout the interval of interest. Immediately above that energy, at around 10-20 keV, the perpendicular anisotropy of electrons was large (>1.1). Thus, we conclude that this perpendicular anisotropy is the free energy source for whistler wave generation in and around DFBs. In Figure 4.2(c), energies are normalized to this minimum resonant energy, showing that the anisotropy peak is around 2 to 3 times the whistler minimum resonant energy. The median anisotropy organized by energy normalized to the electron temperature is shown in Figure 4.2(d). In that figure, although the thermal population of electrons remains isotropic or field-aligned anisotropic, the suprathermal electron population (which is likely predominantly responsible for whistler wave generation) exhibits significant perpendicular anisotropy. Such a multicomponent electron population explains why electrons that are marginally stable for fluid plasma parameters (temperature anisotropy $T_{e,\perp}/T_{e,||}$) can generate very intense whistler waves [see also Zhang et al., 2018]. Figure 4.2(e) shows the median anisotropy organized according to energy normalized to the energy of the maximum phase space density anisotropy. The intent here is to reveal the peak anisotropy value, which otherwise is masked by the superposed epoch analysis from numerous events. The maximum perpendicular anisotropy, ~2 throughout the interval of interest, is consistent with that in electron populations observed to be associated with whistler wave generation in the radiation belts [see, e.g., Agapitov et al., 2016; Li et al., 2016]. This consistency strongly suggests that this perpendicular anisotropy is the free energy source of the observed whistlers.

We next compare the relative magnitudes of whistler wave Poynting flux $S_{\|}$ and electron energy flux $\delta P_e \cdot V_{DF}$ (associated with the free energy for wave generation) in Figure 4.3. Figures 4.3(a) and 4.3(b) compare $S_{\|}$ and $\delta P_e \cdot V_{DF}$ before and after DF arrival (ahead of and within DFBs), respectively. The median values for the ratio of the two quantities are 0.03% and 0.08%, before and after the DFs, respectively. Even though the median values of the ratio are not very large, the data samples with ratio larger than 1% account for 11% of the data sampled before DFs and 18% of the data sampled after DFs, suggesting that a significant portion of the perpendicular electron energy flux above the minimum resonant energy is directed away from the central plasma sheet in the form of whistler wave Poynting flux. Additionally, the data distribution in this parameter space appears to conform to the 100% line boundary near the upper left corner of Figures 4.3(a) and 4.3(b), suggesting that the whistler wave parallel Poynting flux never exceeds the electron energy flux.

The energetic electron energy flux $\delta P_e \cdot V_{DF}$ is the total amount of free energy associated with the electron anisotropy, i.e., some portion of this energy can be contained in a locally stable electron distribution. Because the wave generation is related to anisotropic electron acceleration, i.e., to shaping of the unstable electron distribution, the wave Poynting flux collected during Δt should be compared with $d\delta P_e/dt \cdot \Delta t \cdot V_{DF}$, where $d\delta P_e/dt$ is the electron energy flux change caused by electron transport across an increasing B_z. To better understand the contribution of whistler waves to electron energy dissipation during earthward transport of electrons, we estimated the perpendicular electron energy gain as a function of equatorial B_Z value. The rate of change of δP_e (difference between perpendicular and parallel electron pressure above the minimum resonant energy) is expressed as:

$$\frac{d\delta P_e}{dt} = \frac{\partial}{\partial B_z}\left(n(T_{e,\perp} - T_{e,||})\right)\frac{dB_z}{dt} \tag{4.3}$$

where n is the electron number density, herein assumed to be proportional to B_Z due to conservation of mass in a flux tube; $T_{e,\perp}$ is the electron perpendicular temperature, which also scales with B_Z due to betatron acceleration (although, such scale does not necessary cover the entire energy range, see Liu and Fu, 2019); and $T_{e,||}$ is the electron parallel temperature, which is proportional to $(B_Z)^{2/5}$ due to conservation of the second adiabatic invariant in a contracting flux tube [Tverskoy 1969; Lyons, 1984; Zelenyi et al., 1990; Artemyev et al., 2011]. The rate of change in equatorial B_z (dB_z/dt) when DFBs are moving earthward can be expressed as $\partial B_z/\partial x \cdot V_{DF}$; the B_z profile as a function of radial distance along the magnetotail can be obtained from Artemyev et al. [2013]. Therefore, we can roughly estimate the energization rate of electrons during their earthward transport by DFBs and calculate the rate of change of δP_e using the equation below:

$$\frac{d\delta P_e}{dt} = n(T_{e,\perp} - T_{e,\parallel})\left(\frac{\frac{\partial n}{\partial B_Z}}{n} + \frac{\frac{\partial T_{e,\perp}}{\partial B_Z} - \frac{\partial T_{e,\parallel}}{\partial B_Z}}{T_{e,\perp} - T_{e,\parallel}}\right)\frac{\partial B_z}{\partial x} V_{DF} \tag{4.4}$$

$\delta\acute{P}_e$ is thus calculated as:

$$\delta\acute{P}_e = \frac{d\delta P_e}{dt} \cdot \Delta t \tag{4.5}$$

where Δt, one second in our analysis, is the time window for each of our whistler wave data samples. Using this alternative approach, the electron energy flux is defined as $\delta\acute{P}_e \cdot V_{DF}$. Figures 4.3(c) and 4.3(d) compare $S_\parallel$ and $\delta\acute{P}_e \cdot V_{DF}$ before and after DFs.

Comparing the two different approaches to computing the electron energy flux (the one used in 4.3(a) and (b) and the one used in 4.3(c) and (d)), we find that using the first approach, the energy density δP_e is the total free energy source for wave generation; using the second approach, $\delta\acute{P}_e$ is the free energy source associated with electron energization during earthward transport of the DFB. The median ratios of $S_\parallel$ to $\delta\acute{P}_e \cdot V_{DF}$ are 1.5% and 3.7% before and after the DFs, respectively. During earthward transport of electrons by DFBs, the perpendicular electron energy gain from betatron acceleration is much larger than the parallel electron energy gain. However, a significant portion of this perpendicular energy gain appears to be evacuated by whistler waves in the form of electromagnetic energy throughout the region affected by the DFB (within and immediately outside it). Since electron energy gain occurs across the region of B_Z increase, whereas Poynting flux transport can occur across a wide region of space surrounding the fronts, electromagnetic energy transport integrated over the DFB interaction region may, in fact, be comparable to the energetic electron energy gain.

4.4 Summary and Discussion

Using ten years of THEMIS magnetotail observations of whistler waves within and around dipolarizing flux bundles, we investigated the electron population responsible for whistler wave generation near them and the role of whistler wave Poynting flux in the evacuation of anisotropic electron energy released through wave generation. We find that because of its perpendicular anisotropy, the suprathermal electron population (10-20keV) above the minimum resonant energy is the major free energy source for whistler wave generation. The thermal electron population is not responsible for whistler wave generation because it is either isotropic or exhibits an opposite, field-aligned anisotropy. This suggests that whistler wave excitation near DFs is a kinetic process involving multi-component electrons exhibiting different anisotropy levels as a function of energy. Fluid plasma parameters such as temperature anisotropy ($T_{e,\perp}/T_{e,||}$) are insufficient to characterize generation of whistler waves near DFBs. Therefore, full kinetic consideration of whistler wave generation is required to describe energy release during electron injection into inner magnetosphere [previous observations of fine structure of whistler wave packets in DFBs support this conclusion, see Fu et al., 2014].

Dipolarizing flux bundles are capable of transporting significant amount of energy earthward, including kinetic energy, thermal energy and electromagnetic energy [Angelopoulos et al., 1994]. The total energy flux in the flow (on the order of $10^2 \mu W/m^2$) is much larger than whistler wave Poynting flux (on the order of $10^{-4} \mu W/m^2$) [Angelopoulos et al., 2002; Eastwood et al., 2013]. However, in this work, we mainly focus on the suparthermal electron population related to whistler wave excitation. We find that whistler waves can occasionally radiate up to several percent of the energy flux of the suprathermal electron population. When electrons are transported earthward by DFBs, a significant portion of the perpendicular energy gain will therefore be directed away from the current sheet towards the ionosphere as electromagnetic energy of whistler waves. Our previous work emphasized the importance of whistler waves in scattering electrons in velocity space and constraining their temperature anisotropy. Here we reveal the importance of whistler waves energetically from the point of view of radiating electron energy flux. In addition, we note that the overall $S_{\parallel}$ to $\delta P_e \cdot V_{DF}$ ratio, while not very high, is not entirely sufficient to characterize the flow of energy from the magnetic field to electron heating to waves. Betatron acceleration leading to electron perpendicular heating occurs at magnetic field temporal or spatial gradients, which are limited spatially. Poynting flux transport, however, occurs over a large region of space ahead of and within DFBs, suggesting that geometrical considerations must also be included in this comparison. Even so, alternative approaches of dissipating perpendicular electron energy, such as current sheet scattering, may also exist [Sergeev et al., 1983; Millan et al., 2007; Eshetu et al., 2019].

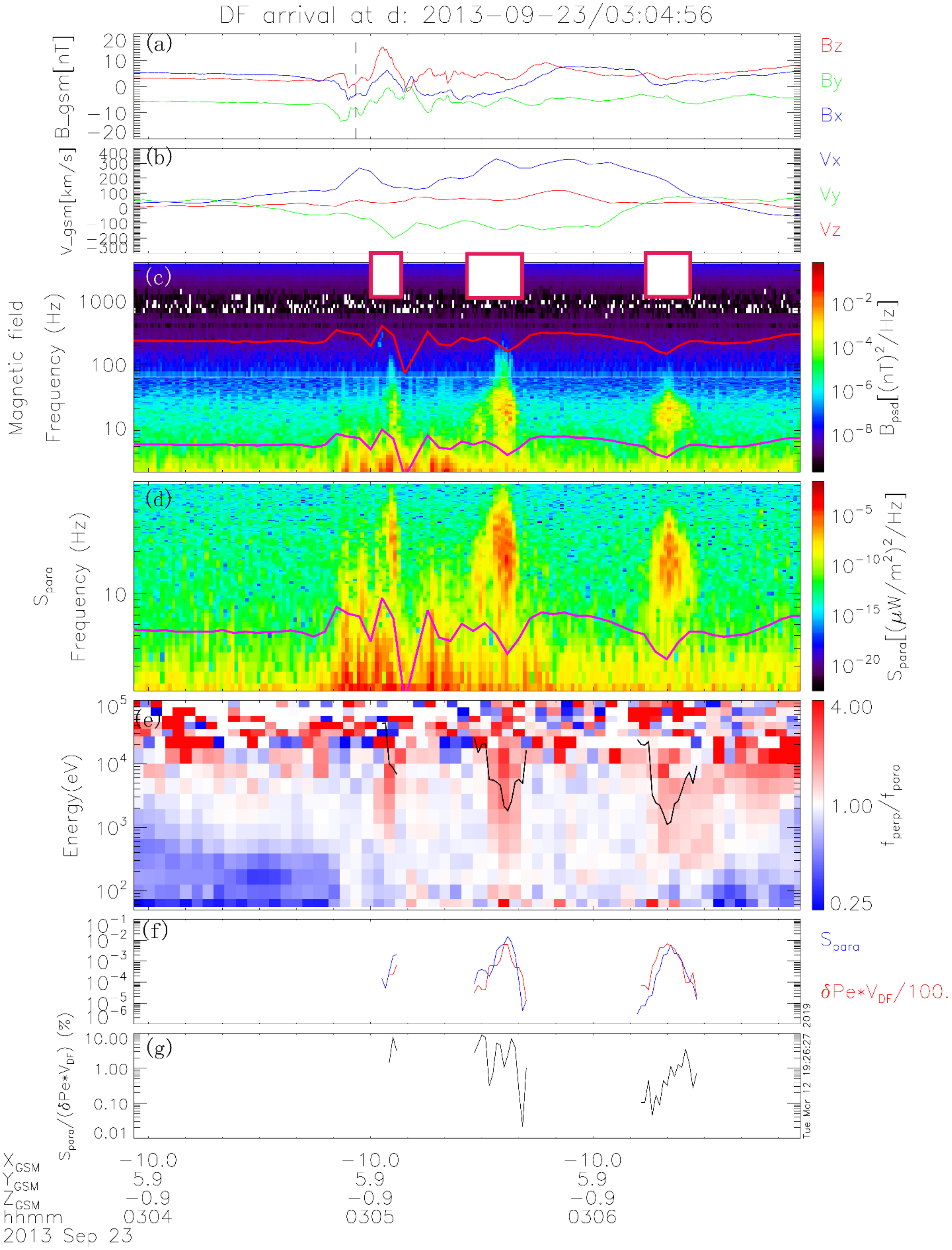
DF arrival at d: 2013-09-23/03:04:56
(a)
B_gsm[nT]
20
10
0
−10
−20
Bz
By
Bx
(b)
V_gsm[km/s]
400
300
200
100
0
−100
−200
−300
Vx
Vy
Vz
(c)
Magnetic field
Frequency (Hz)
1000
100
10
$B_{psd}[(nT)^2/Hz]$
10^{-2}
10^{-4}
10^{-6}
10^{-8}
(d)
S_{para}
Frequency (Hz)
10
$S_{paral}[(\mu W/m^2)^2/Hz]$
10^{-5}
10^{-10}
10^{-15}
10^{-20}
(e)
Energy(eV)
10^5
10^4
10^3
10^2
4.00
1.00
0.25
f_{perp}/f_{para}
(f)
10^{-1}
10^{-2}
10^{-3}
10^{-4}
10^{-5}
10^{-6}
S_{para}
$\delta Pe*V_{DF}/100.$
(g)
$S_{para}/(\delta Pe*V_{DF})$ (%)
10.00
1.00
0.10
0.01
Tue Mar 12 19:26:27 2019
X_{GSM}
Y_{GSM}
Z_{GSM}
hhmm
2013 Sep 23
−10.0
5.9
−0.9
0304
−10.0
5.9
−0.9
0305
−10.0
5.9
−0.9
0306

Figure 4.1: Whistler wave Poynting flux and energetic electron energy flux density. Figure 4.1(a) and 4.1(b): Magnetic field and ion velocity measurements in the GSM (geocentric solar magnetospheric) coordinate system; the black dashed line in Figure 4.1(a) marks the time when the dipolarization front arrived at TH-D; Figure 4.1(c): Magnetic field power spectrum. The magenta line indicates the lower hybrid frequency (f_{lh}); the red line indicates the electron cyclotron frequency (f_{ce}). Vertical white bars with red borders on top of Figure 4.1(c) indicate the intervals during which whistler waves were identified. Figure 4.1(d): Power spectral density of Poynting flux in the direction parallel to the ambient magnetic field at the 2Hz to 64Hz frequency range. Figure 4.1(e): Electron phase space density anisotropy $f_{\perp}/f_{||}$ ($f_{\perp}$ is the electron phase space density averaged over pitch angles in the range (75°, 105°), and $f_{||}$ is the electron phase space density averaged over pitch angles smaller than 30° or larger than 150°) at the energy range from 50eV to 200keV; red indicates perpendicular anisotropy and blue indicates parallel anisotropy. Figure 4.1(f): Comparison between whistler wave parallel Poynting flux (blue) and energetic electron energy flux density (divided by 100 shown in red and defined in text); Figure 4.1(g): Ratio of $S_{\parallel}$ to $\delta P_e \cdot V_{DF}$ in percentage.

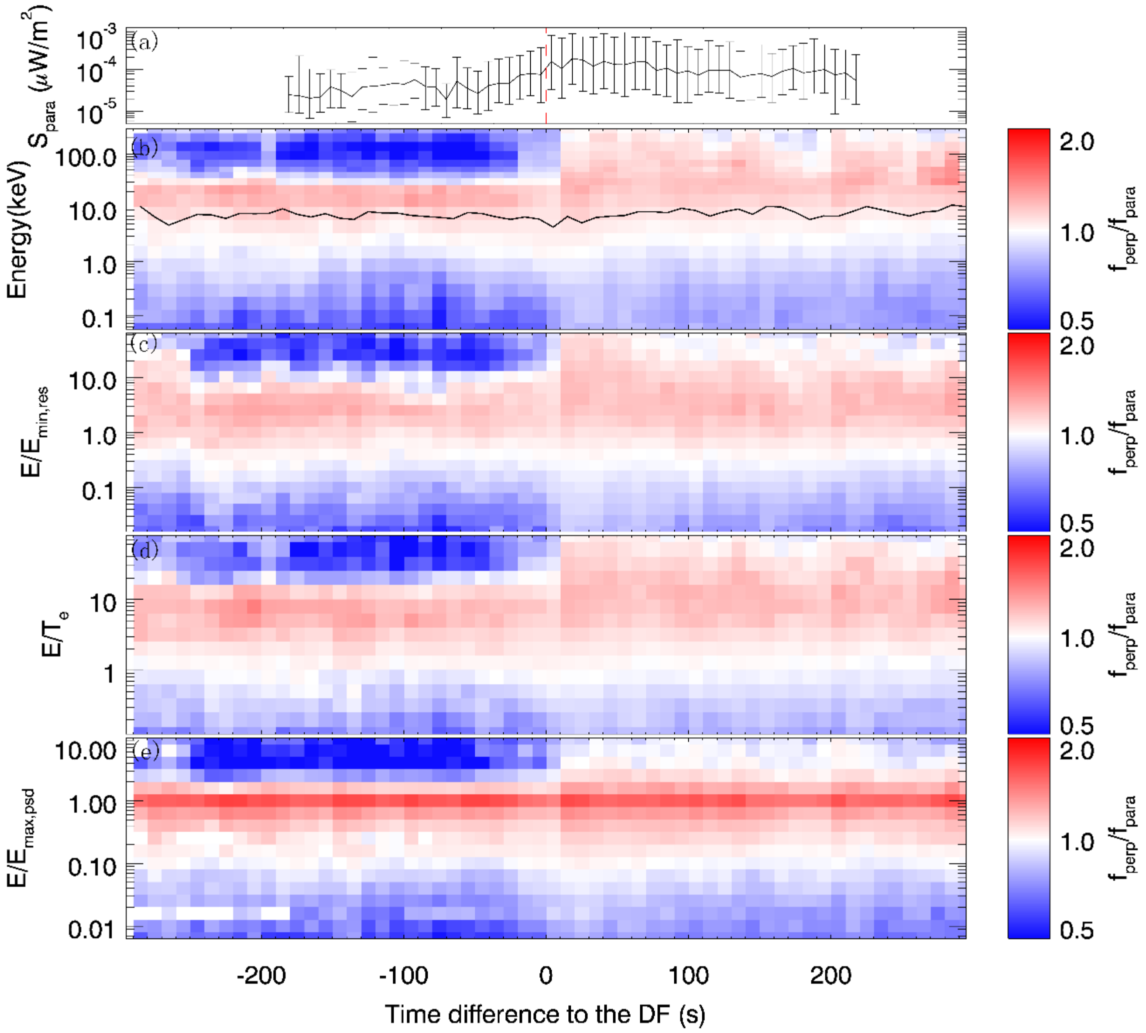

Figure 4.2: Superposed epoch analysis of electron phase space density anisotropy as a function of energy. Zero epoch time is when the DF arrives. Figure 4.2(a): Median value of whistler wave Poynting flux; error bars are the upper and lower quartiles. Figure 4.2(b): Median value of electron phase space density anisotropy as a function of energy. The black solid line is the median value of the minimum resonant energy for the observed whistler waves. Figure 4.2(c): Energy is normalized to minimum resonant energy. Figure 4.2(d): Energy is normalized to electron temperature. Figure 4.2(e): Energy is normalized to the energy that corresponds to the maximum phase space density anisotropy.

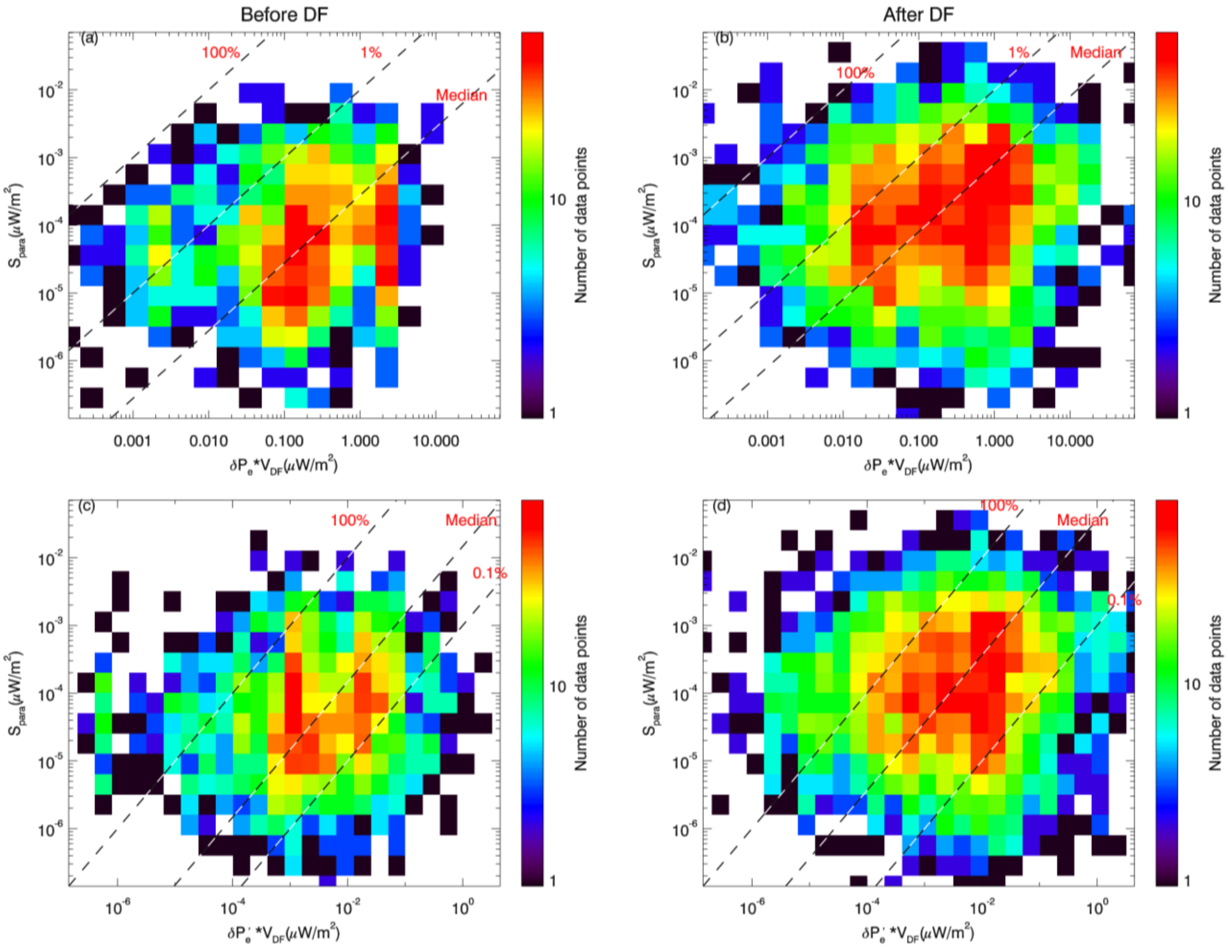

Figure 4.3: Horizontal axis is the energetic electron energy flux density $\delta P_e \cdot V_{DF}$,; the vertical axis is the whistler wave Poynting flux in the parallel direction. Figure 4.3(a), 4.3(c) is the wave data point distribution before DFs, and Figure 4.3(b), 4.3(d) is the wave data point distribution after DFs. The three diagonal dashed lines indicate where the ratios between $S_{\parallel}$ and $\delta P_e \cdot V_{DF}$ are 100%, 1% and median values in Figures 4.3(a) and 4.3(b); 100%, median values and 0.1% in Figures 4.3(c) and 4.3(d). Horizontal axis for Figure 4.3(c) and 4.3(d) is energetic electron energy flux density $\delta\acute{P}_e \cdot V_{DF}$ calculated in an alternative approach discussed in the text.

Chapter 5

Beam-driven electron cyclotron harmonic waves in Earth’s magnetotail

Another electron-driven instability that is frequently observed near dipolarization fronts is electron cyclotron harmonics wave. Zhang et al. [2014] demonstrated that more than 70% of ECH waves in the magnetotail are correlated with energetic electron injections and more than 50% of ECH waves are correlated with dipolarization fronts. High amplitude ECH waves can be observed more frequently upon the arrival of fast plasma sheet flows. Therefore, it is natural for us to investigate ECH waves observed near dipolarization fronts in this chapter. ECH waves have long been thought to be excited by the loss cone anisotropy (velocity-space gradients) of hot plasma sheet electrons in the presence of a cold electron component. There has been very little reconsideration of the excitation mechanism of ECH waves since then. In this chapter, we explore alternative excitation mechanisms for ECH waves in the magnetotail. Using ten years of THEMIS satellite observations, we identify all ECH waves near dipolarization fronts and investigate their properties. ECH waves driven by loss-cone distributions are usually unstable at very large wave normal angles (around 88^o~ 89^o). To our surprise we find that more than 30% of ECH waves observed near dipolarization fronts have moderately oblique ($\sim 70^0$) wave normal angles. The excitation mechanism of these moderately oblique ECH waves is investigated in this chapter.

The outline is as follows. In Section 5.1, we introduce generation mechanism of ECH waves. In Section 5.2, we illustrate our ECH wave event selection criteria. In Section 5.3, we report the first observations of ECH waves at moderately oblique wave normal angles behind dipolarization fronts in the magnetotail. Our statistical results demonstrate that these waves are frequently observed and that they carry a strong field-aligned electric field. In Section 5.4, we confirm theoretically that ECH waves with moderately oblique wave normal angle can be excited by electron beams under plasma sheet conditions. Section 5.5 summarizes our results.

5.1 Introduction

Dipolarizing flux bundles (DFBs) are flux tubes with magnetic field that is more dipolar than the magnetic field of the ambient plasma sheet in the magnetotail [Liu et al., 2013a, 2013b, 2014]. The leading edge of a DFB, characterized by a sharp increase in the northward component of the magnetic field, is referred to as a dipolarization front (DF) [Nakamura et al., 2002; Ohtani et al., 2004; Runov et al., 2009, 2011]. Often observed within fast earthward plasma flows [Baumjohann et al., 1990; Angelopoulos et al., 1992; 1994], DFBs are capable of transporting both magnetic flux and energy flux through the magnetotail toward the inner magnetosphere [Angelopoulos et al., 2013; Liu et al., 2014; Gabrielse et al., 2016, 2019]. Various types of waves have been identified near dipolarization fronts [Le Contel et al., 2009, 2017; Zhou et al., 2009; Khotyaintsev et al., 2011; Viberg et al., 2014] and have been proven to be very effective in regulating electron dynamics near dipolarization fronts [Zhang et al., 2018, 2019]. ECH (electron cyclotron harmonic) wave is one of these wave modes. An ECH wave is an electrostatic emission in the $\mathrm{n}f_{ce}$ (electron cyclotron frequency) to $(n+1)f_{ce}$ frequency range with the strongest wave power in the first harmonic frequency band [Kennel et al., 1970; Meredith et al., 2009]. Because such a wave can scatter plasma sheet electrons into the loss cone through wave-particle interaction, it acts as a potential driver for diffuse auroral precipitation in the magnetotail [Kennel et al., 1970; Lyons, 1974; Belmont et al., 1983; Horne and Thorne, 2000; Ni et al., 2011a, 2011b, 2012, 2016; Zhang et al., 2013, 2014, 2015]. Previous work has demonstrated that more than 70% of ECH waves in the magnetotail are correlated with energetic electron injections and more than 50% of them are correlated with dipolarization fronts [Zhang and Angelopoulos, 2014]. High-amplitude ECH waves excited in the equatorial region tend to expand to a greater latitudinal range in a dipolarized flux tube. Such ECH waves can be observed more easily after DFs, suggesting that DFs are important in driving and intensifying ECH waves in the magnetotail [Zhang et al., 2014]. How ECH waves are correlated with dipolarization fronts is still unclear, however. Understanding the relationship between ECH waves and dipolarization fronts is important because it can reveal how ECH waves are excited near DFs, and it can provide further insight into the potential roles of ECH waves in regulating electron dynamics in the magnetotail and their potential roles in driving diffuse auroral precipitation at higher latitudes.

Previous theoretical work has attributed ECH wave excitation to loss-cone instability of hot plasma sheet electrons in the presence of a cold electron component [Ashour-Abdalla and Kennel, 1978; Ashour-Abdalla et al., 1979; Horne, 1989]. In most work regarding ECH waves, an unstable electron loss-cone distribution is assumed, and the hot plasma dispersion relation is solved [e.g., Horne et al., 2003; Ni et al., 2012; Xu et al., 2018, 2020]. Electron cyclotron harmonic waves driven by such a loss-cone distribution are usually unstable at very large (around $88^o \sim 89^o$) wave normal angles and heavily damped at smaller wave normal angles due to Landau resonance [Horne and Thorne, 2000; Horne et al., 2003; Ni et al., 2011b, 2012]. Such theoretical results are very sensitive to assumed electron plasma parameters, such as loss-cone size, cold electron density and cold electron temperature [Liu et al., 2018, 2020]. Because of the lack of electron distribution function measurements of sufficient angular resolution to reveal the properties of the loss cone (usually less than 1° in the magnetotail) and of the cold electron population, however, such an excitation mechanism has never been proven directly. The loss-cone distribution may not be the only free energy source for ECH wave excitation in disturbed plasma environments near DFs. Modifications of the electron distribution near the resonant energy by an electron beam, enhanced electron temperature anisotropy, or gradients near the loss cone could also result in generation or intensification of ECH waves near DFs [Zhang and Angelopoulos, 2014].

Another excitation mechanism for electrostatic electron cyclotron waves was proposed by Menietti et al. [2002]. The POLAR spacecraft located over the polar cap observed electrostatic waves at frequencies around 1.1 ~ 1.2 f_{ce} and electron beams at energies of tens of eV simultaneously. By solving the hot plasma dispersion relation using Waves in Homogeneous, Anisotropic Multi-component Plasmas (WHAMP, see Ronnmark 1982), Menietti et al. [2002] demonstrated that electrostatic waves above the electron cyclotron frequency can be excited by a low-energy electron beam even in the absence of a loss-cone anisotropy and be unstable at moderately oblique (about 70°) wave normal angles. This is of potential importance because it is an excitation mechanism for ECH waves that has rarely been considered before. Whether that mechanism can operate under plasma conditions (beta, density and magnetic field) in the magnetotail and whether electron beams exist near DFs in the magnetotail and can provide a free energy source for ECH wave generation there are unknown. Because ECH waves excited by loss-cone distributions are unstable at very large wave normal angles, it may be possible to distinguish between beam-driven and loss-cone driven waves observationally using the wave normal angle of ECH waves. Moderately oblique angles would suggest the presence of beam-driven waves that could then be potentially investigated further using linear theory to present evidence for this excitation mechanism in the plasma sheet.

5.2 Data and event selection

The THEMIS Mission consists of five identical probes (TH-A through TH-E) with near-equatorial orbits [Angelopoulos, 2008; Sibeck and Angelopoulos, 2008]. Its fluxgate magnetometer (FGM) measures the direct-current magnetic field and its low-frequency fluctuations (<64Hz) [Auster et al., 2008]. Its Search Coil Magnetometer (SCM) and Electric Field Instrument (EFI) measure magnetic and electric field waveforms in three orthogonal directions [Bonnell et al., 2008; Roux et al., 2008]. Electric field waveform data are calibrated properly and do not affect our results. Data from its SCM and its EFI are passed into the Digital Fields Board to calculate the wave power spectral density of magnetic and electric fields, producing Filter Bank (FBK) and Fast Fourier Transform (FFT) data products [Cully et al., 2008]. These waveform data and onboard spectral data enable us to identify ECH waves and analyze their properties. We also use data from THEMIS electrostatic analyzer (ESA), which measures <30keV particles and its solid state telescope (SST), which measures >35keV particles to achieve our statistical results [McFadden et al., 2008].

We use the DFB event list in Zhang et al. [2018], which was first compiled for years 2007 - 2011 by Liu et al. [2013a] and then extended to year 2017 using identical selection criteria and data from THEMIS magnetotail crossings. Our event database comprises 2285 DFB events that were included in our statistical study. In each DFB event in this extended DFB event list, we identified all ECH waves ±5 minutes from the dipolarization front. Figure 5.1 shows an example of ECH waves observed near dipolarization fronts and illustrates our ECH wave selection criteria. As indicated by the vertical dashed line in Figure 5.1(a), the dipolarization front arrived at TH-D at around 11:08 UT.

Our ECH wave selection criteria are as follows:

1. Using the electric field power spectrum shown in Figure 5.1(c), we integrate the electric field power spectral density from f_{ce} (electron cyclotron frequency calculated from the local magnetic field strength) to $2f_{ce}$. When the integrated electric field power in a data sample is larger than $6 \times 10^{-4}(mV/m)^2$, that sample is included in our ECH wave event database.

2. To exclude broadband emissions with maximum power spectral density at low frequencies (for example, solitary waves [Mozer et al., 1977, 2015; Temerin et al., 1982; Ergun et al., 1998, 2001, 2014; Artemyev et al., 2014a; Vasko et al., 2017]), we require that the peak electric field power spectral density between f_{ce} and $2f_{ce}$ be at least two times larger than the peak electric field power spectral density between $0.6f_{ce}$ and f_{ce}.

The white bars with red borders on the top of Figure 5.1(c) indicate the intervals during which ECH waves are identified. Most wave electric field power is contained in the first harmonic band between f_{ce} and $2f_{ce}$; sometimes, however, these emissions have wave power at higher harmonic bands. Therefore, we were able to select each ECH wave sample in our DFB event database and such waves were detected in 2089 (91%) of the total 2285 DFB events. ECH waves were most frequently observed in the radial distance between 6Re and 10Re and located in the midnight and dawn MLT sector, consistent with the spatial distribution of occurrence rates of ECH waves reported in Ni et al. [2011a].

5.3 Observational Results

5.3.1 Case study

We investigate the interval between 11:12:19 UTC and 11:12:22 UTC (indicated by the black arrow on the top of Figure 5.1(c)) when wave-burst data (8296-samples-per-second waveform electric field data) are available. An example case of ECH waves with a moderately oblique wave normal angle is shown in Figure 5.2. Figure 5.2(a) shows the wave electric field in a field-aligned coordinate system (where E_z is the component parallel to the ambient magnetic field), and Figure 5.2(c) shows the power spectral density of parallel electric field. Considering that ECH waves are electrostatic waves with almost no magnetic field wave power, a large parallel wave electric field compared with total wave electric field suggests that ECH waves propagated at moderately oblique WNA during this interval. Figure 5.2(d) shows the electric field power spectrum. We calculated the root-mean-squared amplitude of the total wave electric field (E_{tot}) and the parallel wave electric field ($E_{\parallel}$). The root-mean-squared amplitude of E_{tot} and $E_{\parallel}$ was calculated using the formula below:

$$E_w = \sqrt{2 * E_{peak,psd} * \Delta f}$$

where $E_{peak,psd}$ is the maximum power spectral density between f_{ce} and $2f_{ce}$. When the power spectral density falls below half its peak, the corresponding frequencies are denoted as upper and lower frequency of ECH waves at the first harmonic frequency band. The difference between these frequencies is Δf. The wave normal angle of an ECH wave is then derived from $\theta = \operatorname{acos}(\frac{E_{\parallel}}{E_{tot}})$. For this event, the value is around 73°, much smaller than previously reported values.

5.3.2 Statistical study

Our next step is to perform a statistical survey of wave normal angles of ECH waves near dipolarization fronts using the ECH wave sample database we established in section 5.2. We first collected ECH waveform data when wave burst modes were available and then calculated the wave normal angles of ECH waves based on the method introduced in section 5.3.1. Our statistical results in the following sections were collected only for wave-burst modes, and we have 2610 wave-burst periods in our DF event database in total. Because wave-burst modes are most likely triggered under active conditions, most of our data samples are from behind dipolarization fronts. Figure 5.3 shows the probability distribution of ECH wave normal angles for different wave intensities. When wave amplitudes are below 5 mV/m, ECH waves with moderately oblique wave normal angles were frequently observed behind dipolarization fronts, suggesting that the event presented in section 5.3.1 is not uncommon. Our statistical results further demonstrate that ECH waves with wave normal angles smaller than 80° account for 34.6% of the total ECH wave samples behind dipolarization fronts, a significant fraction (~one third) of the entire database.

5.3.3 Electron distribution functions

That ECH waves with moderately oblique wave normal angles are frequently observed behind dipolarization fonts suggests that the electron loss-cone distribution is not the only free energy source for wave excitation in the magnetotail. Alternative excitation mechanisms, such as a beam-driven instability, may also operate. To explore such free energy sources for excitation of the observed waves, we investigate electron distribution functions collected when ECH waves were observed, typically behind dipolarization fronts. Statistical results on electron distribution functions are shown in Figure 5.4 and Figure 5.5. Figure 5.4 illustrates electron plasma parameters as a function of wave normal angle and wave amplitude. Moderately oblique wave normal angle ECH waves are often observed when the electron density is high and when the electron temperature is low. Statistical results in Figure 5.4(d) also demonstrate that moderately oblique wave normal angle events are more likely to be observed away from the equatorial current sheet than large wave normal angle events. We also collected electron phase space density f in different directions and at energies from 50eV to 200keV when ECH waves were observed. Figure 5.5 shows electron phase space density anisotropy $f_{\parallel}/f_{\perp}$ as a function of energy and wave normal angle. Clear parallel electron flux enhancements in the subthermal energy range (around a few hundred eV) are correlated with these moderately oblique wave normal angle events, suggesting the presence of low-energy electron beams parallel to the magnetic field when moderately oblique wave normal angle ECH waves were observed (electron flux enhancements at around tens of keV are likely related to injections but not to ECH wave generation [Fu et al., 2011, 2012c]). These beams, which might be associated with ionospheric outflows, are frequently observed in the magnetotail [Hada et al., 1981; Walsh et al., 2013; Artemyev et al., 2014b]. Considering that electrostatic waves above f_{ce} at around 70° may be excited by electron beams [Menietti et al., 2002], it is likely that moderately oblique wave normal angle ECH waves observed behind dipolarization fronts are generated by low-energy electron beams.

5.3.4 Extent of ECH waves

To further characterize the generation mechanism and properties of moderately oblique wave normal angle ECH waves, we used dual-spacecraft observations to estimate the spatial extent of ECH waves inside dipolarizing flux bundles. We first identify ECH waves at two probes for which wave-burst modes are available and calculate the wave normal angle of these waves. A conjunction event is defined as: (1) dipolarization fronts observed at two probes (TH-A, TH-D, or TH-E) within 1 minute and (2) wave-burst modes available at two probes at the same time. There are 284 pairs of conjunction events in our database. Figures 5.6(a) and 5.6(d) show the number of data samples in our conjunction events as a function of spatial separation between two probes in the X_{GSM} and Y_{GSM} directions. Figure 5.6(g) shows the number of data points as a function of difference in B_x/B_{lobe} between two probes. Assuming pressure balance in the vertical direction, B_{lobe} is the estimated lobe magnetic field strength. Both B_x and B_{lobe} are averaged over the time range between 3 minutes prior to the DFs and 1 minute prior to the DFs. The B_x/B_{lobe} ratio represents the vertical distance to the central plasma sheet, and the difference in B_x/B_{lobe} between two probes indicates the vertical separation. Figures 5.6(b), 5.6(e), and 5.6(h) show the occurrence rate when both probes observed ECH waves simultaneously. The occurrence rate when the wave normal angle is smaller than 80° (larger than 85°) is defined as the ratio of the number of data samples from both probes' simultaneous observation of ECH waves with wave normal angles smaller than 80° (larger than 85°) to the total number of data samples in this bin. The normalized occurrence rates are shown in 5.6(c), 5.6(f) and 5.6(i). The normalized occurrence rate for a moderately oblique wave normal angle event (large wave normal angle event) drops below 50% when ΔX is around 1.4 ~ 1.8 Re (1 Re), ΔY is 0.5 Re (0.5 Re), and $\Delta(B_x/B_{lobe})$ is around 0.25 ~

0.45 (0.55). We conclude that moderately oblique wave normal angle ECH waves inside dipolarizing flux bundles have a larger X-extent and a smaller Z-extent than large wave normal angle ECH waves.

5.4 Instability analysis

In this section, we investigate generation of moderately oblique wave normal angle ECH waves by electron beams under plasma sheet conditions. Table 5.1 lists the plasma parameters for the electron distribution, which consists of four populations: one hot population, one cold population, and two beam populations. For the hot population, the temperature is 1 keV and the density is 0.5 cm^{-3}, typical plasma parameter values in the plasma sheet. The background magnetic field strength is 50nT and electron plasma beta ($\beta_e = \frac{n_e k_B T_e}{\frac{B^2}{2\mu_0}}$) is 0.08 (we consider conditions far from the equatorial plane, consistent with the conclusion drawn from Figure 5.4d that moderately oblique ECH waves are likely to be observed away from the equatorial plasma sheet). The electron plasma frequency is 6.96 kHz, and the ratio between the electron plasma frequency and the electron cyclotron frequency $\frac{\omega_{pe}}{\omega_{ce}}$ is 4.7. The temperature of the electron beams, 100 eV, is consistent with observations shown in Figure 5.5(b). Electron beams stream separately in directions parallel and antiparallel to the magnetic field, with a drift velocity of $V_d = 3V_{th}$ (V_{th} is the thermal velocity of an electron beam). No electron populations have loss-cone distributions. Therefore, we rule out the possibility of wave excitation by loss-cone instabilities.

Electron distributions listed in Table 5.1 are used as input parameters to solve the dispersion relation using Waves in Homogeneous Anisotropic Magnetized Plasma (WHAMP) [Ronnmark, 1982]. The dispersion surfaces are shown in Figure 5.7. The wave, which is electrostatic with no magnetic field power and has a frequency between f_{ce} and $2f_{ce}$, is unstable at wave normal angles between 60^o and 70^o and most unstable at 66^o, consistent with our observations. We further confirmed that the excitation of such waves can be attributed to cyclotron resonance with electron beam populations. Low-energy electron beams, therefore, are capable of providing the free energy source for ECH wave generation at moderately oblique wave normal angles under conditions at the edge of the plasma sheet.

5.5 Summary and Discussion

Using ten years (2007-2017) of THEMIS observational data, we established a database of ECH waves in and around dipolarizing flux bundles. By analyzing periods when time-series fields data are available (wave-burst mode data collections), we found the surprising evidence that wave normal angles of ECH waves are sometimes much smaller than previously reported. These moderately oblique ECH waves are most often observed behind dipolarization fronts. They are also observed concurrently with a colder, denser electron population than large wave normal angle waves and they are often located away from the equatorial plasma sheet. As shown in Figure 5.5, field-aligned electron fluxes in the subthermal energy range are enhanced when ECH wave normal angles are moderately oblique, suggesting that these waves might be driven by cold electron beams. We also showed that these moderately oblique wave normal angle ECH waves had a spatial extent of 1.6 Re in the X_{gsm} direction and 0.5 Re in the Y_{gsm} direction inside dipolarizing flux bundles. To explore possible excitation mechanisms of such waves, we performed an instability analysis using WHAMP. Electron distribution functions listed in Table 5.1 were used as input parameters to solve the plasma dispersion relations. We found that ECH waves driven by cold electron beams are most unstable at WNA~66° under conditions at the edge of the plasma sheet.

Electron cyclotron harmonic waves have long been thought to be driven by loss-cone instabilities. Because spacecraft observations of the electron distributions that excite ECH waves have been limited, such an excitation mechanism has never been proven directly. ECH waves excited by loss cone mechanism are unstable only at very large wave normal angles. Even though what excites ECH waves is still an open question, there has been very little reconsideration of the free energy sources of ECH waves since the 1970s. Our work shows both observationally and theoretically that ECH waves can be driven by low-energy electron beams behind dipolarization fronts under plasma conditions prevailing near the edge of the plasma sheet. From observations of ECH waves at moderately oblique wave normal angles, we suggest that an alternative excitation mechanism, excitation by electron beams, might exist behind dipolarization fronts in the plasma sheet. Such a mechanism is confirmed by solving linear dispersion relations as shown in Figure 5.7. Thus, the loss-cone distribution is not the only free energy source for ECH waves in the plasma sheet: ECH waves at moderately oblique wave normal angles are most likely electron beam driven. These ECH waves likely relax by heating low-energy electron beams, transferring energy from the waves to electrons. Because wave normal angle is a very important parameter controlling the scattering rate of plasma electrons into loss cones [see review by Ni et al., 2016; and references therein], it is also possible that these waves play a role in electron scattering into the loss cone. Under certain plasma conditions, wave normal angles of beam-driven ECH waves might even be close to 90°, making it difficult to distinguish loss-cone driven waves from beam-driven waves. We plan to carry out a more detailed parametric study of beam-driven ECH waves in the next step. Future investigation of these moderately oblique wave normal angle ECH waves will significantly improve our understanding how ECH waves are generated and how they affect plasma sheet electron dynamics.

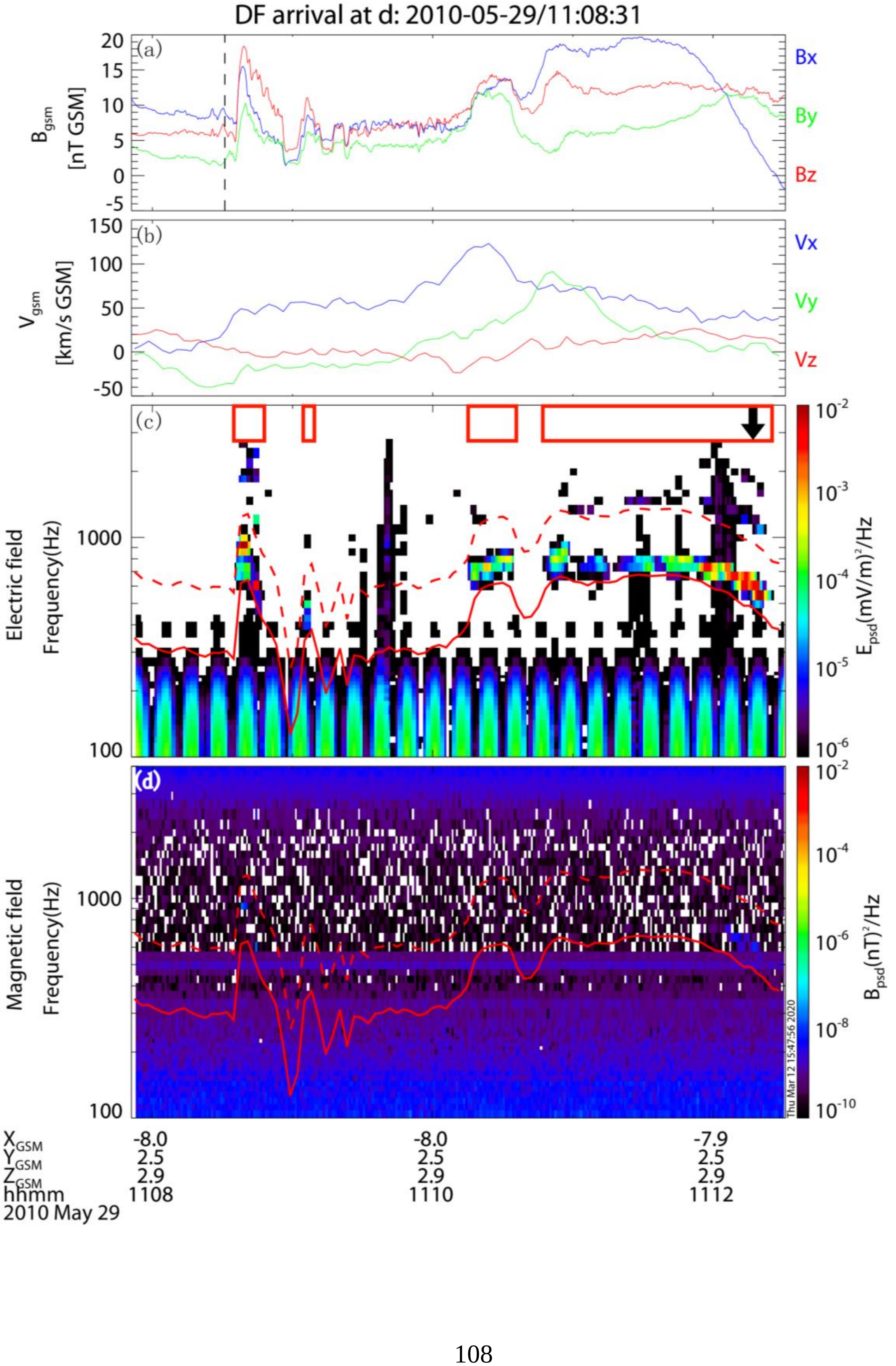
DF arrival at d: 2010-05-29/11:08:31
(a)
B_{gsm} [nT GSM]
Bx
By
Bz
(b)
V_{gsm} [km/s GSM]
Vx
Vy
Vz
(c)
Electric field Frequency(Hz)
$E_{psd}(mV/m)^2/Hz$
(d)
Magnetic field Frequency(Hz)
$B_{psd}(nT)^2/Hz$
Thu Mar 12 15:47:56 2020
X_{GSM} -8.0 -8.0 -7.9
Y_{GSM} 2.5 2.5 2.5
Z_{GSM} 2.9 2.9 2.9
hhmm 1108 1110 1112
2010 May 29

Figure 5.1: Overview plot to illustrate ECH wave selection criteria. Figure 5.1 (a): Magnetic field in GSM (geocentric solar magnetospheric) coordinates. The vertical dashed line indicates arrival of a dipolarization front at TH-D; (b): Ion velocity in GSM coordinates; (c) and (d): Electric field power spectrum and magnetic field power spectrum. The solid red line is f_{ce} (electron cyclotron frequency calculated from the local magnetic field strength) and the dashed red line is $2f_{ce}$. The white bars with red borders on the top of (c) indicates the time intervals during which ECH waves were identified. The black arrow on upper right side of (c) indicates the time interval shown in Figure 5.2.

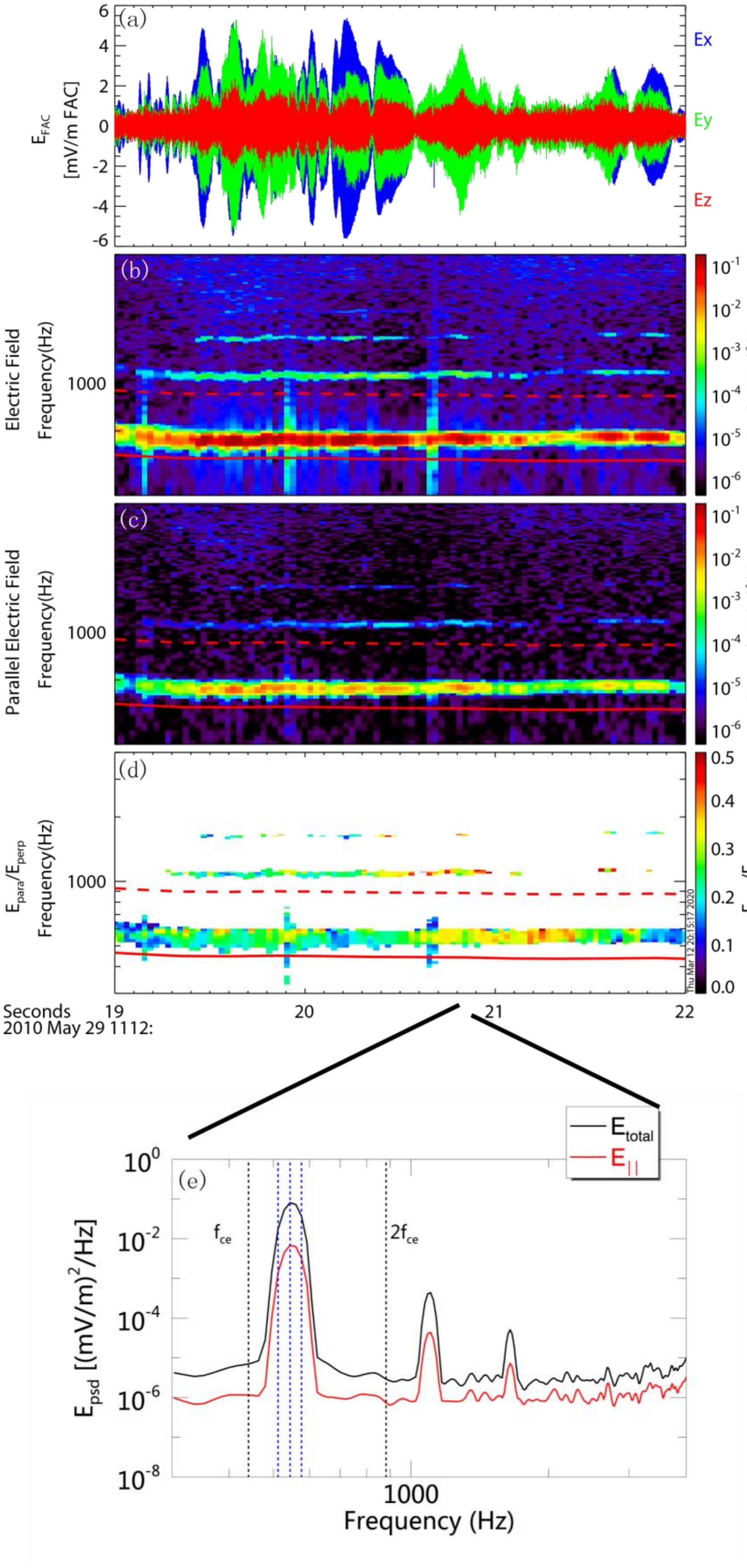
(a)
6
4
2
0
-2
-4
-6
E_FAC [mV/m FAC]
Ex
Ey
Ez
(b)
Electric Field Frequency(Hz)
1000
10^-1
10^-2
10^-3
10^-4
10^-5
10^-6
E_psd(mV/m)^2/Hz
(c)
Parallel Electric Field Frequency(Hz)
1000
E_para,psd(mV/m)^2/Hz
(d)
E_para/E_perp Frequency(Hz)
1000
0.5
0.4
0.3
0.2
0.1
0.0
E_para/E_perp
Thu Mar 12 20:15:17 2020
Seconds 19 20 21 22
2010 May 29 1112:
(e)
E_total
E_||
10^0
10^-2
10^-4
10^-6
10^-8
E_psd [(mV/m)^2/Hz]
f_ce
2f_ce
1000
Frequency (Hz)

Figure 5.2: An example case to demonstrate ECH waves at moderately oblique wave normal angles. (a): Electric field waveform data in the field-aligned current (FAC) system and Z_{FAC} points in the direction parallel to the ambient magnetic field; (b): Electric field power spectrum. The solid red line represents f_{ce} and the dashed red line represents $2f_{ce}$; (c): Electric field power spectral density in the parallel direction; (d): Ratio of electric field power spectral density in the parallel direction to electric field power spectral density in the perpendicular direction. Only data points when total electric field power spectral density is greater than $10^{-4}(mV/m)^2/Hz$ are plotted; 2(e): Total electric field power spectral density (black line) and parallel electric field power spectral density (red line) as a function of frequency. The three dashed blue lines indicate lower frequency, central frequency, and upper frequency of ECH waves in its first harmonic band.

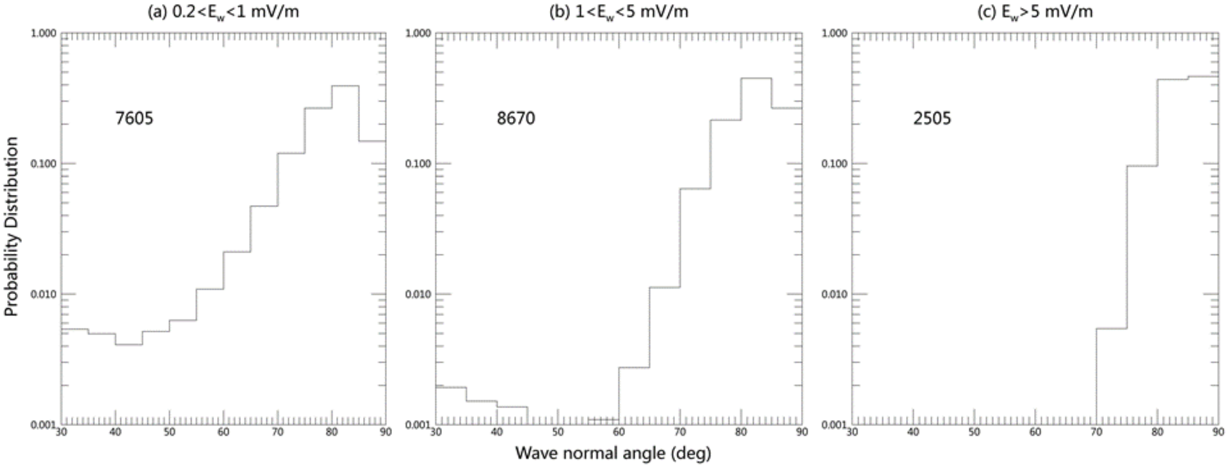

Figure 5.3: Probability distribution of ECH wave normal angles for different wave intensities. Figure 5.3(a): $0.2 < E_w < 1mV/m$; Figure 5.3(b): $1 < E_w < 5mV/m$; Figure 5.3(c): $E_w > 5mV/m$. Total number of data points in each category are marked in each panel.

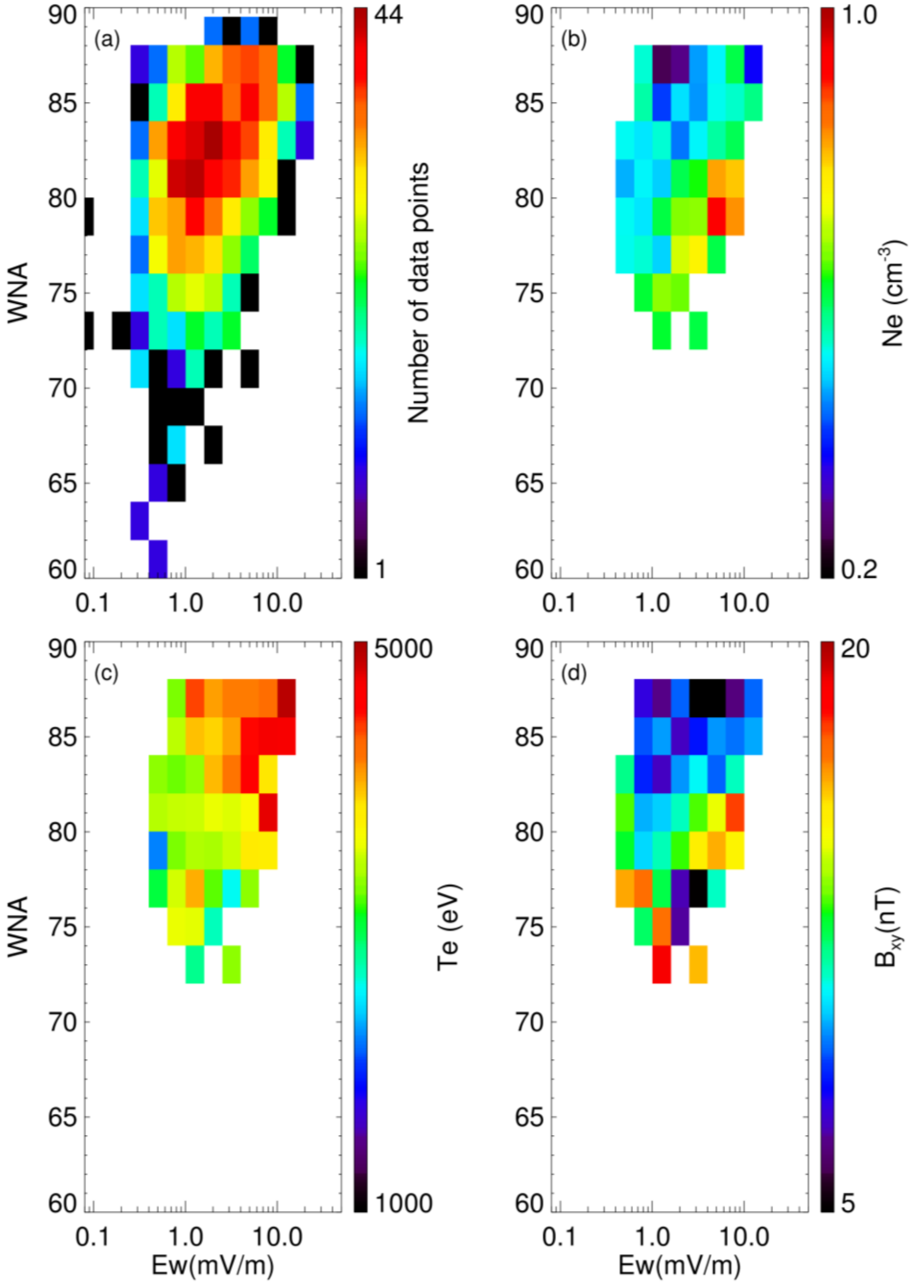

Figure 5.4: Figure 5.4(a): Number of data points as a function of wave normal angle and wave amplitude; Figure 5.4(b)-5.4(d) show the median values in each bin. Figure 5.4(b) and 5.4(c): Electron number density and electron temperature; Figure 5.4(d): $B_{xy} = \sqrt{B_x^2 + B_y^2}$ as an indication of vertical distance to the central current sheet. Only bins with number of data points greater than 10 are shown in panels b-d.

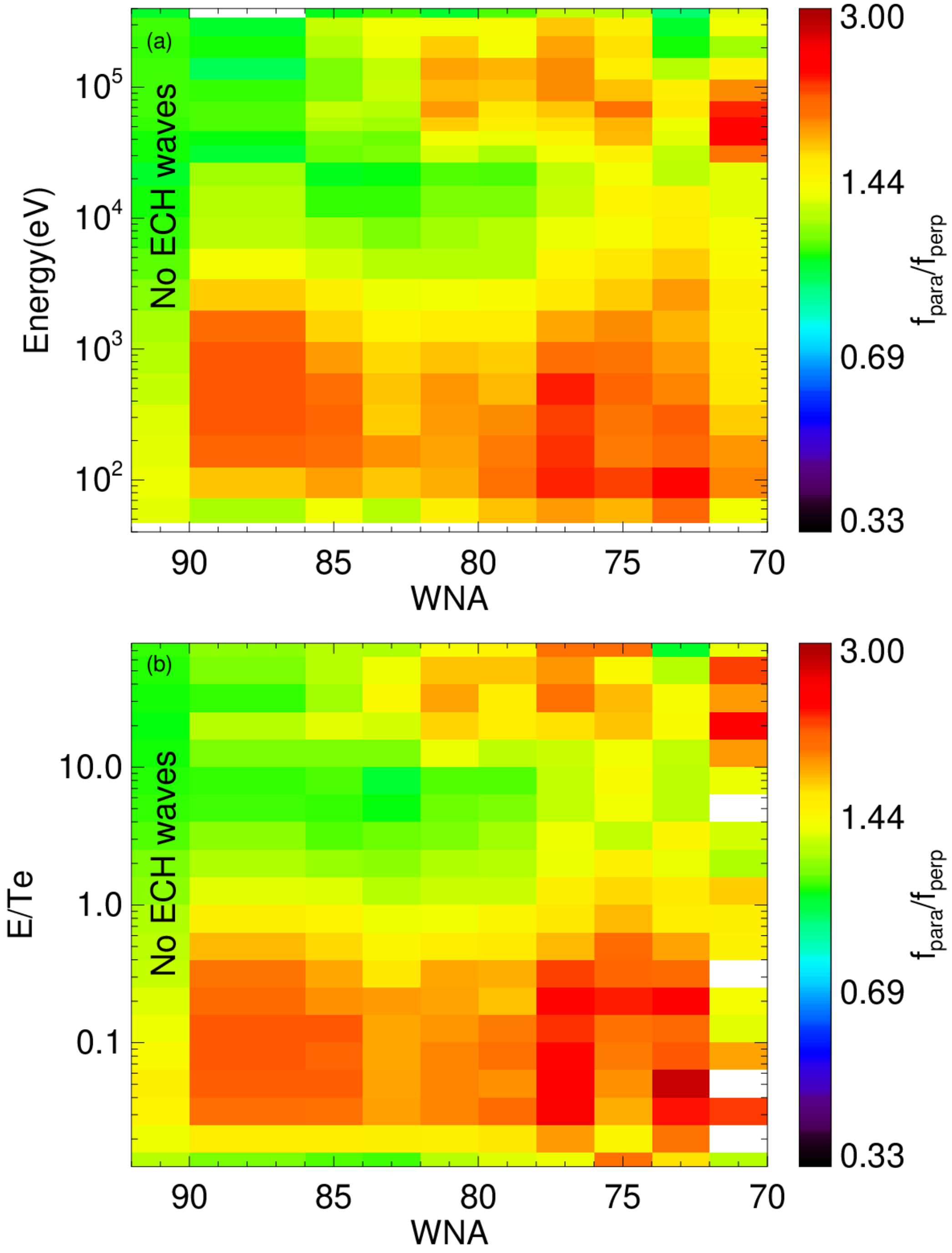
(a)
No ECH waves
Energy(eV)
10^5
10^4
10^3
10^2
90
85
80
75
70
WNA
3.00
1.44
0.69
0.33
f_{para}/f_{perp}
(b)
No ECH waves
E/Te
10.0
1.0
0.1
90
85
80
75
70
WNA
3.00
1.44
0.69
0.33
f_{para}/f_{perp}

Figure 5.5: Electron phase space density anisotropy as a function of energy and wave normal angle. Figures 5.5(a) and 5.5(b) show the median values in each bin. Figure 5.5(a): Electron phase space density anisotropy is defined as $f_{\parallel}/f_{\perp}$ ($f_{\parallel}$ is electron phase space density in the parallel direction, $f_{\perp}$ is electron phase space density in the perpendicular direction). The leftmost column shows the median values of electron phase space density anisotropy when ECH waves are not present. Red color indicates parallel anisotropy and blue color indicates perpendicular anisotropy; Figure 5.5(b): Electron phase space density anisotropy as a function of normalized energy and wave normal angle. Energy is normalized to electron temperature. The leftmost column shows the median values of electron phase space density anisotropy when ECH waves are not present. Only bins with number of data points greater than 10 are plotted. To avoid poor statistics due to the lack of sufficient data points, we average two columns when wave normal angle is from 86° to 90°.

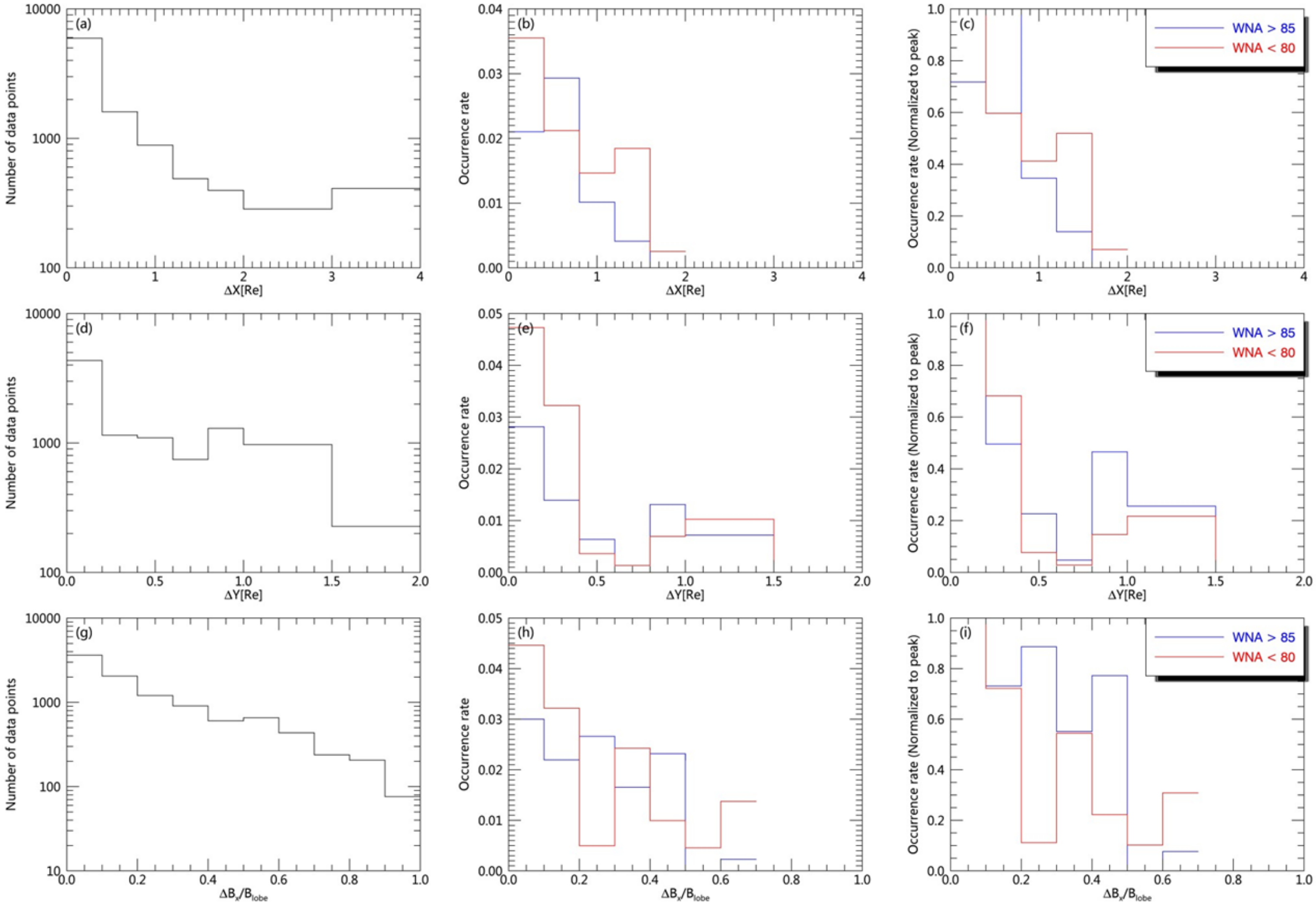
(a)
(b)
(c)
(d)
(e)
(f)
(g)
(h)
(i)
Number of data points
Occurrence rate
Occurrence rate (Normalized to peak)
ΔX[Re]
ΔY[Re]
ΔB_x/B_lobe
WNA > 85
WNA < 80
10000
1000
100
10
0.00
0.01
0.02
0.03
0.04
0.05
0.0
0.2
0.4
0.6
0.8
1.0
0
1
2
3
4
0.5
1.5
2.0

Figure 5.6: Spatial extent of ECH waves inside dipolarizing flux bundles in three different directions Figure 5.6(a): Number of data points at a function of ΔX (spatial separation between two probes in X_{gsm} direction); Figure 5.6(b): ECH wave occurrence rate (ratio between number of data points when both probes observe ECH waves at the same time and total number of data points in each bin) as a function of ΔX. Red color indicates data samples when wave normal angles are smaller 80^{o} and blue color indicates data samples when wave normal angles are larger than 85^{o}; Figure 5.6(c): Normalized occurrence rate as a function of ΔX; Figure 5.6(d), 5.6(e), 5.6(f): Number of data points, ECH wave occurrence rate and normalized occurrence rate as a function of ΔY (spatial separation between two probes in Y_{gsm} direction); Figure 5.6(g), 5.6(h), 5.6(i): Number of data points, ECH wave occurrence rate and normalized occurrence rate as a function of $\Delta(B_x/B_{lobe})$ (difference in B_x/B_{lobe} between two probes).

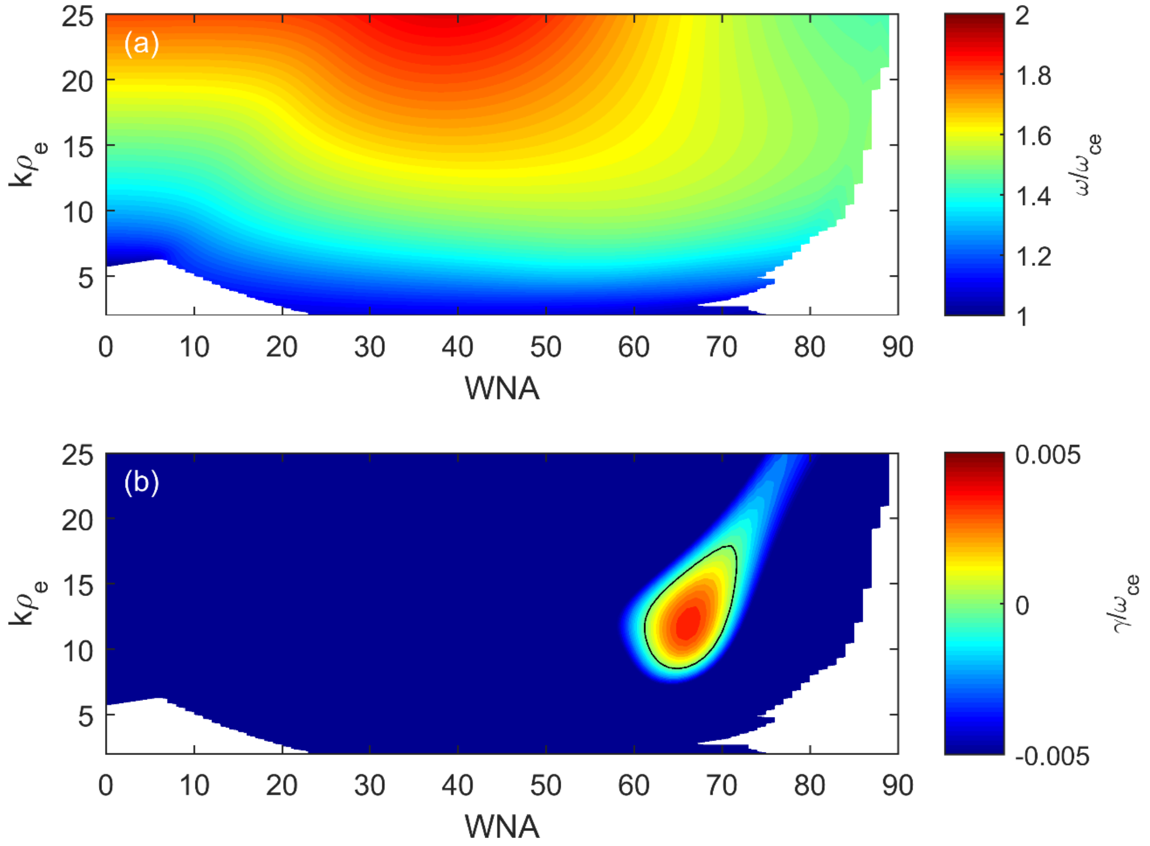

Figure 5.7**:** Dispersion surface for ECH waves. Background magnetic field strength is 50nT. Figure 5.7(a): Normalized wave frequency (f/f_{ce}) as a function of normalized wave number and wave normal angle. Wave number is normalized to the gyroradius of thermal electron population (electron component 1 in Table 5.1); Figure 5.7(b): wave growth rate as a function of normalized wave number and wave normal angle. Solid black line indicates the contour of zero growth rate.

Table 5.1 Electron distribution function

Component	n (cm^{-3})	$T_{\|\|}$ (keV)	$T_{\|\|}/T_{\perp}$	$V_{drift}/V_{thermal}$
1	0.5	1	0.85	0
2	0.05	0.001	1	0
3	0.025	0.1	0.85	3
4	0.025	0.1	0.85	-3

Chapter 6

Beam-driven ECH waves: A parametric study

ECH waves in magnetospheric plasmas have long been thought to be excited predominantly by the loss cone anisotropy (velocity-space gradients) that arises naturally in a planetary dipole field. There has not been too much reconsideration of the free energy sources of ECH waves other than loss cone distributions. In previous chapter, however, we presented observational evidence for ECH wave excitation by low-energy electron beams in the magnetotail using THEMIS observational data. The ambient and beam plasma conditions under which electron beam excitation can take place still remain unknown. Knowledge of such conditions would allow us to further explore the relative contribution of this excitation mechanism to ECH wave scattering of magnetospheric electrons at Earth and the outer planets. We extend our work in Chapter 5 by evaluating the growth rates of beam-driven ECH waves and the plasma conditions under which beam-driven ECH waves can be excited.

The outline of this chapter is as follows. In Section 6.1, we briefly introduce beam-driven ECH waves. In Section 6.2, we calculate the individual contributions of Landau resonance and cyclotron resonances to the growth rate. We also explore excitation of an ECH wave by electron beams at its second harmonic band. In Section 6.3, we evaluate the dependence of dispersion relations and the growth rate of beam-driven ECH waves on various plasma parameters, including density, drift velocity, temperature and temperature anisotropy of electron beams, density and temperature of the hot electron population, and density and temperature of the cold electron population. Section 6.4 summarizes our results.

6.1 Introduction

An electron cyclotron harmonic (ECH) wave is an electrostatic emission in the $\mathrm{n}f_{ce}$ (electron cyclotron frequency; $n = 1,2,3$ ...) to $(n+1)f_{ce}$ frequency range with the strongest wave power in its first harmonic band, $n = 1$ [Fredricks and Scarf, 1973; Shaw and Gurnett, 1975; Roeder and Koons, 1989; Meredith et al., 2009; Zhang and Angelopoulos, 2014]. First observed by the OGO 5 satellite, such electrostatic waves have wave power centered around $(n+1/2)f_{ce}$ [Kennel et al., 1970]. They have since been observed over a large range of radial distances in both Earth's inner magnetosphere [Meredith et al., 2009; Ni et al., 2011a, 2017] and its magnetotail [Liang et al., 2011; Zhang et al., 2014]. The most intense ECH waves in Earth's magnetosphere, which are often within a few degrees in latitude relative to the magnetic equator, have been frequently observed between 2100 and 0600 magnetic local time, i.e. in the night-side magnetosphere [Roeder and Koons, 1989; Meredith et al., 2009; Ni et al., 2017]. They have also been observed in the magnetospheres of other planets, such as Jupiter [Kurth et al., 1980; Menietti et al., 2012] and Saturn [Gurnett et al., 2005; Tao et al., 2010], and in active space experiments [Mourenas et al., 1989]. In Saturn's magnetosphere, ECH waves tend to intensify and have more harmonic bands during injection events [Menietti et al., 2008; Tao et al., 2010]. Because both ECH waves and whistler-mode waves can resonate with electrons over the broad energy range from hundreds of eV to tens of keV, the relative importance of these waves in driving diffuse aurora had been controversial for decades [Kennel et al., 1970; Lyons, 1974; Belmont et al., 1983; Horne and

Thorne, 2000; Horne et al., 2003; Meredith et al., 2000, 2009; Thorne et al., 2010]. Recently, however, it was recognized that ECH waves play an important role in scattering plasma electrons into the loss cone and in driving diffuse aurora in the outer magnetosphere, beyond eight Earth radii in the magnetotail [Ni et al., 2011b, 2012, 2016, Zhang et al., 2013, 2015].

Previous theoretical work demonstrated that ECH waves can be excited by the loss-cone distribution with a positive phase space density slope perpendicular to the ambient magnetic field ($\partial f/\partial v_{\perp} > 0$) [Young et al., 1973; Karpman et al., 1975; Ashour-Abdalla and Kennel, 1978; Ashour-Abdalla et al., 1979]. Assuming an unstable loss-cone distribution of a hot electron component in the presence of a cold electron component, Ashour-Abdalla and Kennel [1978] demonstrated that when the density and temperature ratios of cold to hot electrons are small enough, ECH waves are unstable. Electron cyclotron harmonic waves driven by loss-cone distributions usually propagate at very large (around 88°~ 89°) wave normal angles with respect to the background magnetic field and are heavily damped at smaller wave normal angles by Landau resonance [Horne, 1989; Mourenas and Beghin 1991; Horne and Thorne, 2000; Horne et al., 2003; Ni et al., 2011b, 2012; Liu et al., 2018]. Because measuring electron distribution functions around and within the loss cone (from a few degrees to less than one degree in pitch-angle space) is difficult, excitation of ECH waves by loss-cone instability has never been demonstrated directly using space measurements. Despite this lack of direct observational evidence of their excitation mechanism, there has been very little questioning or reconsideration of this mechanism since the theoretical work on loss-cone instability of many decades ago mentioned earlier. Whether there are other mechanisms for excitation of ECH waves apart from the loss cone instability had been unknown, until very recently.

The first observational evidence for ECH wave excitation in the magnetosphere by means other than the loss-cone instability was presented by Zhang et al. [2021]. Using data from the THEMIS mission [Angelopoulos, 2008] they found that ECH waves in the magnetotail can also be excited by low-energy electron beams. In the absence of loss-cone distributions, ECH waves driven by electron beams are unstable at moderately oblique wave normal angles (~70^0) [Menietti et al., 2002]. According to Zhang et al. [2021], such ECH waves, which have a strong wave electric field parallel to the magnetic field, can be quite frequently observed in the magnetotail behind sharp fronts of dipolarizing magnetic flux populated by hot plasma and embedded within fast flows (so-called dipolarization fronts; see, e.g., Runov et al. 2009). That these waves are correlated with parallel electron flux enhancement in the subthermal energy range suggests that they are likely driven unstable by low-energy electron beams. In Zhang et al. [2021], the authors also provided theoretical evidence for excitation of ECH waves by such beams in Earth's magnetotail. Using electron distribution functions with electron beams with realistic, plasma-sheet-like input parameters, the authors solved the dispersion relation and demonstrated that ECH waves can indeed by driven unstable by low-energy electron beams.

Even so, the generation mechanism of ECH waves driven by electron beams and the beam and ambient plasma conditions that favor excitation of beam-driven ECH waves still remain unclear. In this paper we extend the Zhang et al. [2021] instability analysis in two ways. First, we analyze the generation mechanism of beam-driven ECH waves by evaluating their dispersion relations and growth rates. We emphasize the relative importance of different resonances in a straightforward approach. Second, we perform a comprehensive parametric survey to quantify the dependence of these waves on various plasma parameters. We investigate the plasma conditions under which ECH waves might be driven unstable by electron beams. Our results could greatly improve our understanding of the growth and damping of beam-driven ECH waves under different plasma conditions and provide theoretical guidance for future work regarding beam-driven ECH waves in many space plasma environments.

6.2 Excitation of beam-driven ECH waves

In this section, we solve the hot plasma dispersion relations using the Waves in Homogeneous, Anisotropic Multi-component Plasmas code (WHAMP, see Ronnmark 1982) and analyze the growth rate of beam-driven ECH waves. The electron distribution function is represented as the sum of bi-Maxwellians:

$$f(v_\perp, v_\parallel) = \sum_i f_i = \sum_i \frac{n_i}{\pi^{2/3}\alpha_{\perp i}^2 \alpha_{\parallel i}} \exp\,(-(\frac{v_\parallel - v_{di}}{\alpha_{\parallel i}})^2) \cdot \exp\left(-\frac{v_\perp^2}{\alpha_{\perp i}^2}\right) \tag{6.11}$$

where the subscript *i* is the *i*th component of the electron distribution function, n_i is the electron number density, and $\alpha_{\parallel i}$ and $\alpha_{\perp i}$ are the thermal velocity of electrons in directions parallel and perpendicular to the magnetic field.

Table 6.1 lists the components of the electron distribution function: one hot component, one cold component, and two beam components. The temperature of the ion population is 5keV (typical temperature of magnetotail plasma) with no temperature anisotropy, and the ion population remains unchanged. The background magnetic field strength is 50nT and the electron plasma beta ($\beta_e = (\sum n_e k_B T_e)/(B^2/2\mu_0)$) is 0.08. The ratio of the electron plasma frequency to the electron cyclotron frequency ω_{pe}/ω_{ce} is 5, and the ratio of the upper hybrid frequency to the electron cyclotron frequency ω_{uh}/ω_{ce} is 5.1. These parameters are typical of the ECH wave generation region in Earth's plasma sheet. The two electron beam components drift in directions parallel and antiparallel, respectively, to the magnetic field. No electron component has loss-cone distributions. We modified systematically the density and temperature of the cold electron population starting from those in the electron distribution function used in Zhang et al. [2021]. These changes, which will be explained later, will benefit the parametric study in Section 6.3. The input parameters in the distribution function in Table 6.1 are used to calculate the results shown in Figure 6.1 and Figure 6.2.

Before embarking on the parametric study, we investigate how electrons resonate with ECH waves in velocity space in order to gain insight into the nature of the waves' excitation mechanism. The resonance condition for the nonrelativistic case is expressed as:

$$\omega - k_{\parallel} v_{\parallel} = n|\omega_{ce}| \tag{6.12}$$

where ω is the wave frequency, $k_{\parallel}$ is the wave vector in the direction parallel to the magnetic field, and *n* is the resonance harmonic number. Figure 6.1 shows the dispersion relation of beam-driven ECH waves in wave number space and the individual growth rate contributions from different resonance harmonic numbers *n*. As illustrated in Figures 6.1(a) and 6.1(b), electron cyclotron harmonic waves driven by electron beams at a temperature of 100eV are most unstable at wave normal angles of 55^0 and at wave frequency of $1.1 f_{ce}$. To calculate growth rate contributions from Landau and cyclotron resonances, we modified the WHAMP program based on Equations (6.3) to (6.11). The dispersion relation for electrostatic waves can be simplified as below:

$$\mathcal{D} = k_{\perp}^2 \varepsilon_{xx} + k_{\perp} k_{\parallel} (\varepsilon_{xz} + \varepsilon_{zx}) + k_{\parallel}^2 \varepsilon_{zz} = 0 \tag{6.13}$$

where $k_\parallel$ and $k_\perp$ are wave vectors parallel and perpendicular to the magnetic field, and ε_{xx}, ε_{xz}, ε_{zx} and ε_{zz}, different elements in the dielectric tensor used when solving the hot plasma dispersion relation, are defined as:

$$\varepsilon_{xx} = 1 + \sum_i \frac{\omega_{pi}^2}{\omega^2} \sum_n \int \frac{v_\perp (n/\Lambda_i)^2 J_n^2(\Lambda_i)}{\omega - k_\parallel v_\parallel - n\Omega_{ci}} U d^3 v \tag{6.14}$$

$$\varepsilon_{xz} = \sum_i \frac{\omega_{pi}^2}{\omega^2} \sum_n \int \frac{v_\perp (n/\Lambda_i) J_n^2(\Lambda_i)}{\omega - k_\parallel v_\parallel - n\Omega_{ci}} W d^3 v \tag{6.15}$$

$$\varepsilon_{zx} = \sum_i \frac{\omega_{pi}^2}{\omega^2} \sum_n \int \frac{v_\parallel (n/\Lambda_i) J_n^2(\Lambda_i)}{\omega - k_\parallel v_\parallel - n\Omega_{ci}} U d^3 v \tag{16.6}$$

$$\varepsilon_{zz} = 1 + \sum_i \frac{\omega_{pi}^2}{\omega^2} \sum_n \int \frac{v_\parallel J_n^2(\Lambda_i)}{\omega - k_\parallel v_\parallel - n\Omega_{ci}} W d^3 v \tag{6.17}$$

with

$$\Lambda_i = \frac{k_\perp v_\perp}{\Omega_{ci}} \tag{6.18}$$

$$U = (\omega - k_\parallel v_\parallel) \frac{\partial f_{0i}}{\partial v_\perp} + v_\perp k_\parallel \frac{\partial f_{0i}}{\partial v_\parallel} \tag{6.19}$$

$$W = (\omega - n\Omega_{ci}) \frac{\partial f_{0i}}{\partial v_\parallel} + \frac{n\Omega_{ci} v_\parallel}{v_\perp} \frac{\partial f_{0i}}{\partial v_\perp} \tag{6.20}$$

The subscript i is the ith component of the electron distribution function, ω_{pi} is the plasma frequency of the ith component, n is the resonance harmonic number in Eq. (6.2), Ω_{ci} is the cyclotron frequency of the ith component, J_n is the Bessel function of the first kind, and f_{0i} is the phase space density of the ith component. Assuming weak growth or damping of the waves, the growth rate is calculated from the equation below:

$$\gamma = -Im(\mathcal{D})/(\partial(Re(\mathcal{D}))/\partial\omega) \tag{6.21}$$

where $\mathcal{D}$ refers to the dispersion relation in Eq. (6.3), $Im(\mathcal{D})$ is the imaginary part of $\mathcal{D}$, and $Re(\mathcal{D})$ is the real part of $\mathcal{D}$.

From Eqs. (6.3) to (6.11), we can isolate different resonance harmonic numbers n and calculate contributions to the growth rate from isolated resonances. The results are shown in Figures 6.1(d)-6.1(f). Both Landau and cyclotron resonances contribute to the unstable region of beam-driven ECH waves in wave number space. The major contributors to wave growth are cyclotron resonance at n = -1 and cyclotron resonances at higher resonance harmonic numbers.

Figure 6.2 is a geometric interpretation of wave-particle interaction in the velocity space of the electron distribution function. Considering an isolated resonance with resonance harmonic number n, when analyzing the particle equation of motion for the non-relativistic case using a Hamiltonian approach, we obtain that quantity C_n in Eq. (6.12) is a constant [Shklyar and Matsumoto, 2009]

$$C_n = nW - \mu\omega = \text{constant} \tag{6.22}$$

where W is the particle kinetic energy ($W = \frac{1}{2}m(v_\perp^2 + v_\parallel^2)$), μ is $(\frac{1}{2}mv_\perp^2)/\omega_{ce}$, and ω is the wave frequency. In terms of Landau resonance, when n = 0, Eq. (6.12) reduces to $v_\perp = \text{constant}$. Taking into account cyclotron resonance when n = 1 and the resonance condition described by Eq. (6.2), we obtain the "diffusion curve" or "resonance curve" discussed in many papers [Gendrin, 1968, 1981; Summers et al., 1998; Thorne et al., 2005]. When electrons interact with waves at the resonance velocity, they diffuse along the curve corresponding to constant C_n, and the net transport in phase space is towards regions with lower phase space density. If this direction is towards smaller particle kinetic energy, particles will lose energy when interacting with waves, resulting in wave generation. When calculating the curve corresponding to the constant C_n in Figure 6.2 and the resonance velocity with n = 0, -1, -2, we used wave parameters corresponding to the maximum growth rate in Figure 6.1. The plasma parameters for the electron distribution function in Figure 6.2 are the same as in Figure 6.1, as shown in Table 6.1. Taking into account Landau resonance when n = 0 and cyclotron resonances when n = -1 and n = -2, Figure 6.2 depicts the curves corresponding to constant phase space density, constant C_n, and constant energy, where magenta lines with arrows indicate the directions in which particles diffuse. The stability of the wave can only be determined after the combined effects from all perpendicular velocities have been accounted for, which is accomplished by integration along the vertical line for a fixed resonant (parallel) velocity. However, it is evident from Figure 6.2 that when n = 0 (Landau resonance) and when n = -1 and -2 (cyclotron resonances) electrons will lose energy and waves will gain energy due to the overwhelming contribution from the normalized perpendicular velocities of 0.2-0.5, where the downward gradient in phase space density points towards lower energies.

Next, we investigate the excitation of an ECH wave by low-energy electron beams at its second harmonic frequency band (between $2f_{ce}$ and $3f_{ce}$). When the electron distribution functions in

Table 6.1 are used, ECH waves at the second harmonic band are stable. Therefore we increased the drift velocity of electron beam components and used the electron distribution functions listed in Table 6.2 to solve the dispersion relation for the second harmonic. The background magnetic field strength is 50nT. Figure 6.3 shows the wave frequency and growth rate in wave number space for the second harmonic band; we can see that growth (within the black contour) can occur over a significant portion of the frequency-wave number space. The most unstable solution at the second harmonic frequency band for the choice of parameters in Table 6.2 is at wave frequency of $2.12f_{ce}$ and at wave normal angle of 76^{o}. We conclude that ECH waves at higher harmonic frequency bands can also be driven unstable by electron beams.

6.3 Parametric study of beam-driven ECH waves

Before presenting the results from our parametric study of beam-driven ECH waves, we would like to discuss electron acoustic waves which can also be driven unstable by cold beams in a warm plasma. During our search for ECH waves with maximum growth rate, we sometimes found that the most unstable wave is in the propagation direction parallel to the magnetic field (see the case in supporting information). We confirmed these to be electron acoustic waves driven unstable through Landau resonance with electron beams [Gary & Tokar, 1985; Singh and Lakhina, 2001; Lu et al., 2005]. Electron acoustic waves often overlap with ECH waves in frequency, making it difficult for us to distinguish between them from their dispersion relations alone. By changing the density and temperature of the cold electron population, we can vary the frequency of an electron acoustic wave and avoid an overlap of the two waves in real frequency. In this parametric survey, electron acoustic waves are not excited or do not appear in the f_{ce} to $2f_{ce}$ frequency range. A wider parameter regime, allowing for both waves to be excited simultaneously needs to be considered in the future.

In this section, we conduct a parametric survey of beam-driven ECH waves using the plasma components listed in Table 6.1: a hot electron component, a cold electron component, and two electron-beam components streaming in opposite directions. To better understand the dependence of the beam-driven ECH wave growth rate on various plasma parameters, we plot the electron distribution functions as a function of parallel velocity with zero perpendicular velocity for different plasma parameters in Figure 6.4. The total electron distribution function is defined as

$$\begin{aligned} f(v_\perp, v_\parallel) &= \frac{n_H}{\pi^{2/3}\alpha_{\perp H}^2 \alpha_{\parallel H}} \exp\left(-\frac{{v_\parallel}^2}{{\alpha_{\parallel H}}^2}\right) \cdot \exp\left(-\frac{{v_\perp}^2}{{\alpha_{\perp H}}^2}\right) \\ &+ \frac{n_c}{\pi^{2/3}\alpha_{\perp c}^2 \alpha_{\parallel c}} \exp\left(-\frac{{v_\parallel}^2}{{\alpha_{\parallel c}}^2}\right) \cdot \exp\left(-\frac{{v_\perp}^2}{{\alpha_{\perp c}}^2}\right) \\ &+ \sum \frac{n_b}{\pi^{2/3}\alpha_{\perp b}^2 \alpha_{\parallel b}} \exp\left(-\frac{(v_\parallel - v_b)^2}{{\alpha_{\parallel b}}^2}\right) \cdot \exp\left(-\frac{{v_\perp}^2}{{\alpha_{\perp b}}^2}\right) \end{aligned} \tag{6.23}$$

where the subscript H is the hot electron population, subscript c is the cold electron population, and subscript b is the electron beam population. We will use this figure during the section to explain the evolution of the phase space gradient magnitude at the various resonant frequencies, as the parameters of the distribution function are modified.

Each figure in this section (Figures 6.5 through 6.8) shows the dependence of wave properties on two different sets of plasma parameters. The plasma parameters represented by the horizontal axis and the vertical axis consist of 50 different values, respectively, and there are 50x50 grid points in each figure. For every grid point, we solve the hot plasma dispersion relation for the first harmonic band of beam-driven ECH waves in wave number space, with wave vector $k\rho_e$ ranging from 0 to 30 and wave normal angle ranging from 0^0 to 90^0. We search for an ECH wave with maximum growth rate in the wave number space, and every grid point in these figures represents a solution corresponding to the most unstable ECH wave in the first harmonic frequency band.

6.3.1 Dependence on beam density and beam velocity

Figure 6.5 illustrates the dependence of the wave growth rate, wave frequency, and wave normal angle of the most unstable wave on the beam density and beam velocity (beam density refers to the density of one electron beam component rather than the total density of two electron beam components). We vary the beam density from 0 to $0.1cm^{-3}$ and the normalized beam velocity (normalized to the thermal velocity of the beam) from 0 to 5 keeping all the other plasma parameters in Table 6.1 unchanged. Only grids with maximum growth rate greater than 0 (unstable wave) are plotted. At fixed beam velocity, the ECH wave growth rate increases with beam density; at fixed beam density, the ECH wave growth rate increases with beam velocity. This is because when beam density or beam velocity decrease, the electron distribution function “flattens” with subtler beam characteristics and gentler gradients (see Figure 6.4(b) and Figure 6.4(c) for illustrations). Therefore, ECH waves stabilize. The wave frequency decreases slightly with beam density. The most unstable ECH waves become more oblique when beam velocity increases and less oblique when beam density increases.

6.3.2 Dependence on beam temperature and beam temperature anisotropy

Next, in Figure 6.6, the parallel beam temperature is varied from 10eV to 1keV, and the beam temperature anisotropy (defined as the ratio of perpendicular beam temperature to parallel beam temperature) from 0.15 to 0.9 (we change the temperature anisotropy of the beam by varying its perpendicular temperature while keeping its parallel temperature unchanged). All the other plasma parameters remain the same as in Table 6.1. At fixed beam temperature anisotropy, as the beam temperature increases from 10eV up to ~30eV, the growth rate of ECH wave increases because the waves resonate with a steeper part of the phase space density gradient. When the beam temperature further increases from 30eV to 1keV, the growth rate contributed from cyclotron resonances decreases. This is because the distribution function broadens (see Figure 6.4(d) for illustrations) and ECH waves stabilize. At fixed beam temperature in the parallel direction, the growth rate of ECH waves decreases when electron beams become more perpendicularly anisotropic. For the most unstable wave, the wave normal angle of ECH waves increases with beam temperature and decreases with beam temperature anisotropy.

6.3.3 Dependence on temperature and density of hot electrons

We vary the temperature of the hot electron population (the first component in Table 6.1) from about 60eV to 16keV as shown in the horizontal axis in Figure 6.7. The density of the hot electron population on the vertical axis ranges from 0.05cm^{-3} to 5cm^{-3}; the ratio of the electron plasma frequency to the electron cyclotron frequency ω_{pe}/ω_{ce} ranges from 2.6 to 14.5. The electron plasma beta in this parametric space ranges from 0.002 to 13. At fixed hot electron temperature, the growth rate of the ECH wave decreases as the hot electron density increases. This is because the electron distribution function flattens with a smaller phase space density gradient in the parallel direction when the density of hot electrons increases (see Figure 6.4(f) for illustration). The growth rate contributed from cyclotron resonances decreases, and ECH waves are thus damped by Landau resonance with the hot electron component. When the hot electron temperature decreases at fixed hot electron density, the electron distribution function broadens and the growth rate of ECH waves decreases (see Figure 6.4(g) for illustration). Towards the regions of lower growth rate with larger hot electron density and lower hot electron temperature in the parametric space, ECH wave normal angles for the most unstable waves become larger.

6.3.4 Dependence on temperature and density of cold electron

Next we vary the density and temperature of the cold electrons (the second component in Table 6.1) leaving the other plasma parameters the same as in Table 6.1 (beam density is changed to $0.025cm^{-3}$). We vary the density of the cold electron component from $0.005\mathrm{cm}^{-3}$ to $0.5\mathrm{cm}^{-3}$, and the temperature of the cold electron component from 0.1eV to 10eV. When the temperature of the cold electron component becomes too high, ECH waves stabilize because ECH waves are Landau damped due to their interaction with cold electrons (as illustrated in Figure 6.4(h)). When the density of the cold electron component is too large (> 0.1 cm^{-3}) (or too small (< 0.01 cm^{-3})), the frequency of a beam-driven ECH wave gets close to f_{ce} (or to $2f_{ce}$) and the resonance velocity in Eq. (6.2) for $n = +1$ ($n = +2$) becomes too small. Under those conditions, ECH waves are damped by cyclotron resonance with the $n = +1$ (or n = +2) resonance. Notably, we find that the wave frequency of ECH waves at their first harmonic changes from $1.1f_{ce}$ to $1.9f_{ce}$ when the density of the cold electron component changes. When we vary the plasma parameters for electron beams and hot electrons, however, the frequency of ECH waves remains nearly unchanged. Therefore, electron density is a very important parameter in determining the frequency of beam-driven ECH waves. Conversely, wave frequency measurements are an important diagnostic of cold electron density, which is often poorly constrained.

6.4 Summary and Discussion

Using an electron distribution function with a hot component, a cold component, and two beam components as input parameters, we solved the hot plasma dispersion relation for ECH waves and investigated wave generation and wave properties under different plasma conditions. Our primary findings are summarized below:

1. At moderately oblique wave normal angles, ECH waves driven by low-energy electron beams are unstable. The growth rate of beam-driven ECH waves is mainly controlled by cyclotron resonance when the resonance harmonic number *n* is -1 and by cyclotron resonances when *n* is between -2 and -5.

2. Electron cyclotron harmonic waves at their second harmonic frequency band can also be driven unstable by electron beams.

3. The maximum growth rate of a beam-driven ECH wave increases with electron beam density and electron beam drift velocity. The wave normal angle of a beam-driven ECH wave increases with beam velocity and decreases with beam density.

4. The maximum growth rate of a beam-driven ECH wave decreases with beam temperature and beam temperature anisotropy. The wave normal angle increases with beam temperature and decreases with beam temperature anisotropy.

5. When the hot electron density is higher, the growth rate of a beam-driven ECH wave is lower and its wave normal angle is larger. When the hot electron temperature is higher, the growth rate of a beam-driven ECH wave is higher and its wave normal angle is smaller.

6. A beam-driven ECH wave is stabilized when the temperature of the cold electron component is too large and when the density of the cold electron component is either too large or too small. The cold electron density controls the frequency of the most unstable beam-driven ECH waves.

Our results reveal the nature of the beam-driven ECH wave excitation mechanism and demonstrate the dependence of wave properties on various plasma parameters. The loss-cone distribution is not the only free energy source for ECH waves: they can also be driven unstable by electron beams for a wide range of ambient plasma parameters that encompass the magnetotail plasma sheet. Such an excitation mechanism has been confirmed observationally in Zhang et al [2021] and further explored theoretically here. Therefore, our work improves our understanding of this previously unknown excitation mechanism.

From our parametric survey, we found that electron acoustic waves can also be excited by low-energy electron beams in a similar frequency range as ECH waves, but they propagate mostly parallel to the magnetic field (see supporting information). Excited by beam-plasma instability, electron acoustic waves may coexist with beam-driven ECH waves in observations [Roeder et al., 1991] and may also compete with beam-driven ECH waves by relaxing electron beams upon saturation [Omura and Matsumoto, 1987; An et al., 2017; Agapitov et al., 2018].

Beam-driven ECH waves with wave frequency ranging from $1.1f_{ce}$ to $1.9f_{ce}$ and wave normal angles ranging from 40^0 to 80^0 are unstable under a wide range of plasma conditions in electron plasma betas from as small as 0.003 and as large as 12.9 (as shown in Figure 6.7). Excitation of beam-driven ECH waves under such a wide range of plasma parameters suggests that they might exist not only in the magnetotail but also in many other regions of Earth’s magnetosphere. Likely to originate in the ionosphere, low-energy electron beams could be (1) secondary electrons produced by precipitating plasma sheet electrons [Khazanov et al., 2014; Artemyev et al., 2020]; (2) upward electron beams accelerated by an electric field parallel to the magnetic field and near downward field-aligned currents [Carlson et al., 1998; Hull et al. 2020]. Such low-energy ionospheric electron beams have been observed in both the magnetotail [Walsh et al., 2013; Artemyev et al., 2015] and the outer radiation belt [Kellogg et al., 2011; Mourenas et al., 2015]. Therefore, we would expect beam-driven ECH waves to exist not only near dipolarization fronts in the plasma sheet, as shown by Zhang et al. [2021], but also in the magnetotail and in the inner magneotosphere, even during quiet times.

Electron cyclotron harmonic waves driven unstable by a loss-cone distribution resonate with electrons through cyclotron resonance when the resonance harmonic number, *n*, is 1; beam-driven ECH waves are driven unstable through cyclotron resonance with electron beams when *n* is -1 and of higher order. Excited by a totally different mechanism from the one that excites loss cone-driven ECH waves, beam-driven ECH waves would interact with electrons in a completely different way. During the excitation of beam-driven ECH waves, energy is transferred from electron beams to ECH waves and ECH waves saturate by slowing down electron beams. The electron distribution function would eventually flatten and form a plateau in the velocity space. Additionally, beam-driven ECH waves are characterized by a moderately oblique wave normal angle. Because wave normal angle is an important parameter in evaluating the pitch-angle diffusion coefficients for ECH waves, the pitch-angle diffusion coefficient profile as a function of equatorial pitch angle and energy for beam-driven ECH waves would be different from the profile for loss cone-driven ECH waves. Evaluating the effects of beam-driven ECH waves on electron dynamics is thus important to explore in future studies.

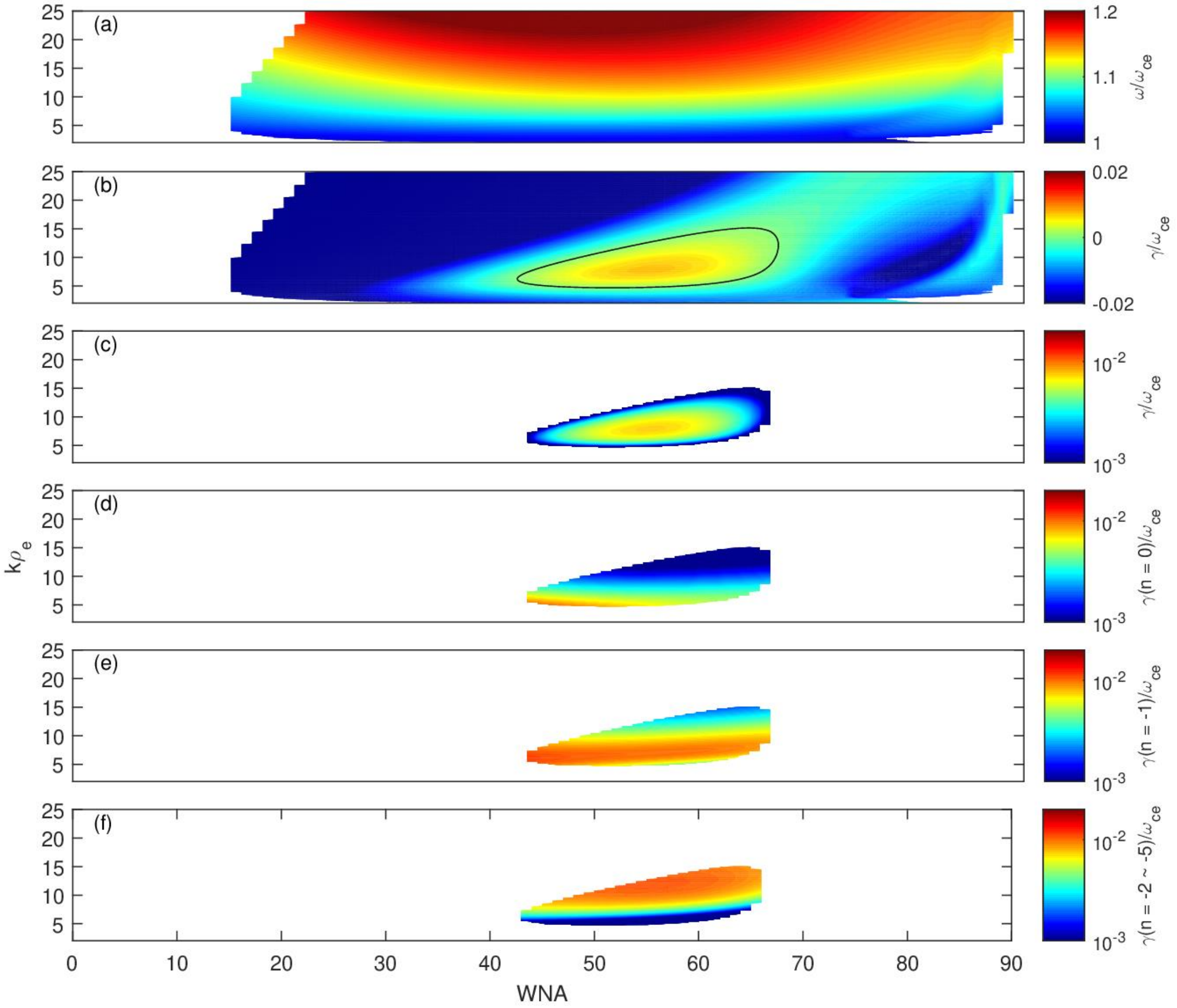

Figure 6.1: Dispersion relations and contributions to the growth rate from different resonance harmonic numbers for beam-driven ECH waves. The horizontal axis is the wave normal angle, and the vertical axis is the wave vector normalized to the gyroradius of the hot electron component (the first component in Table 6.1). (a): Wave frequency normalized to the electron cyclotron frequency; (b): Growth rate normalized to the electron cyclotron frequency (the black line indicates the zero growth rate contour); (c): Growth rate in log scale; (d): Growth rate contributed by the Landau resonance when *n* = 0. Only data points with positive growth rate are plotted; (e): Growth rate contributed by the cyclotron resonance when *n* = -1; (f): Growth rate contributed by the cyclotron resonances at higher orders (summation of *n* = -2,-3,-4,-5)

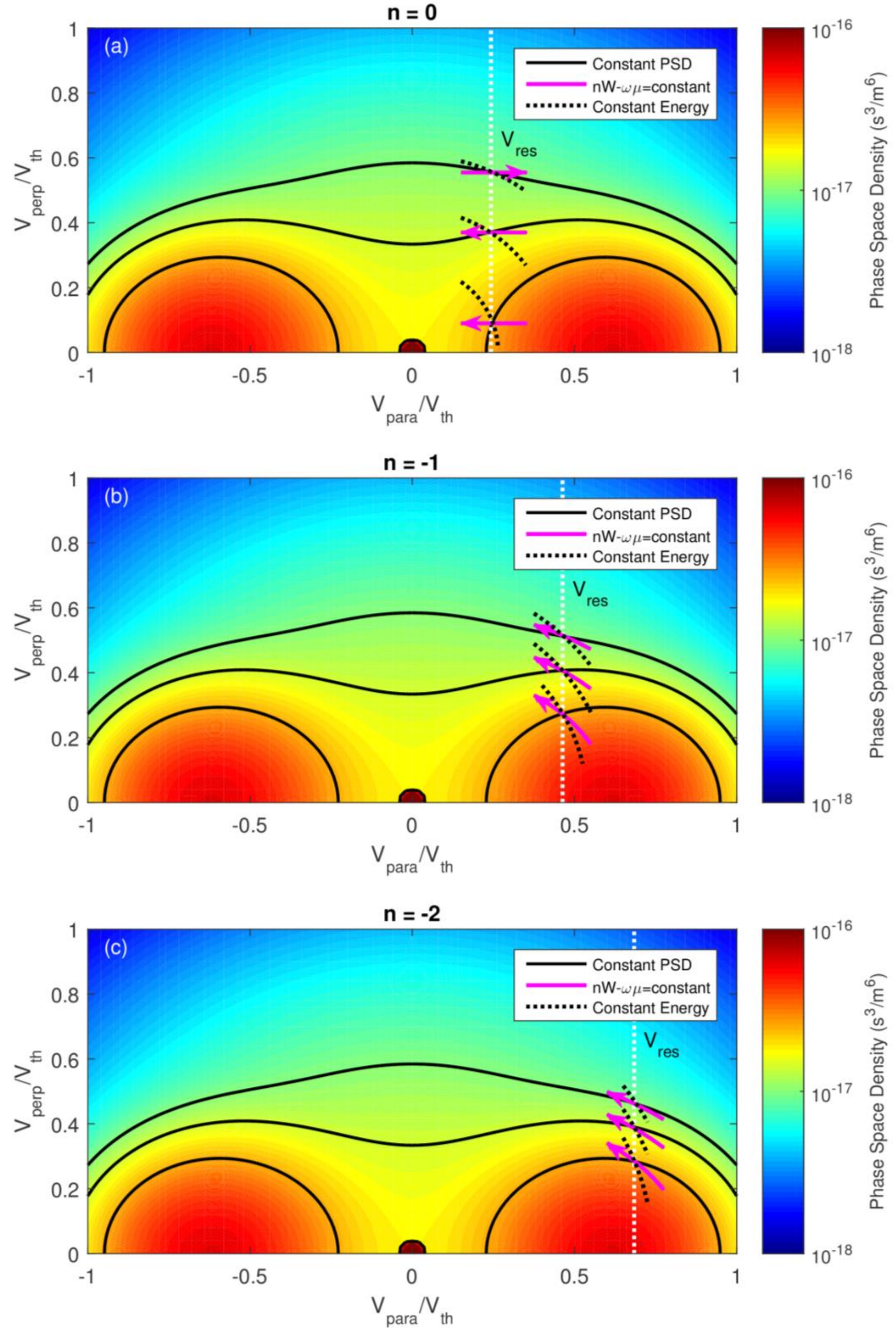
n = 0
(a)
Constant PSD
nW-$\omega\mu$=constant
Constant Energy
V_{res}
V_{perp}/V_{th}
V_{para}/V_{th}
0
0.2
0.4
0.6
0.8
1
-1
-0.5
0
0.5
1
10^{-16}
10^{-17}
10^{-18}
Phase Space Density (s^3/m^6)
n = -1
(b)
Constant PSD
nW-$\omega\mu$=constant
Constant Energy
V_{res}
V_{perp}/V_{th}
V_{para}/V_{th}
10^{-16}
10^{-17}
10^{-18}
Phase Space Density (s^3/m^6)
n = -2
(c)
Constant PSD
nW-$\omega\mu$=constant
Constant Energy
V_{res}
V_{perp}/V_{th}
V_{para}/V_{th}
10^{-16}
10^{-17}
10^{-18}
Phase Space Density (s^3/m^6)

Figure 6.2: The electron distribution function plotted using the plasma parameters listed in Table 6.1. Parallel velocity on the horizontal axis and perpendicular velocity on the vertical axis are normalized to the thermal velocity of the first component in Table 6.1. The solid black lines represent constant phase space density, and the dotted black lines represent constant particle energy. Using the wave properties corresponding to the maximum growth rate in Figure 6.1, we plot the contours of Eq. (6.12), indicated by solid magenta lines with arrows, and the resonance velocity, indicated by dotted white lines. Figures 6.2(a), 6.2(b), and 6.2(c) demonstrate the case when $n = 0, -1$, and -2 respectively.

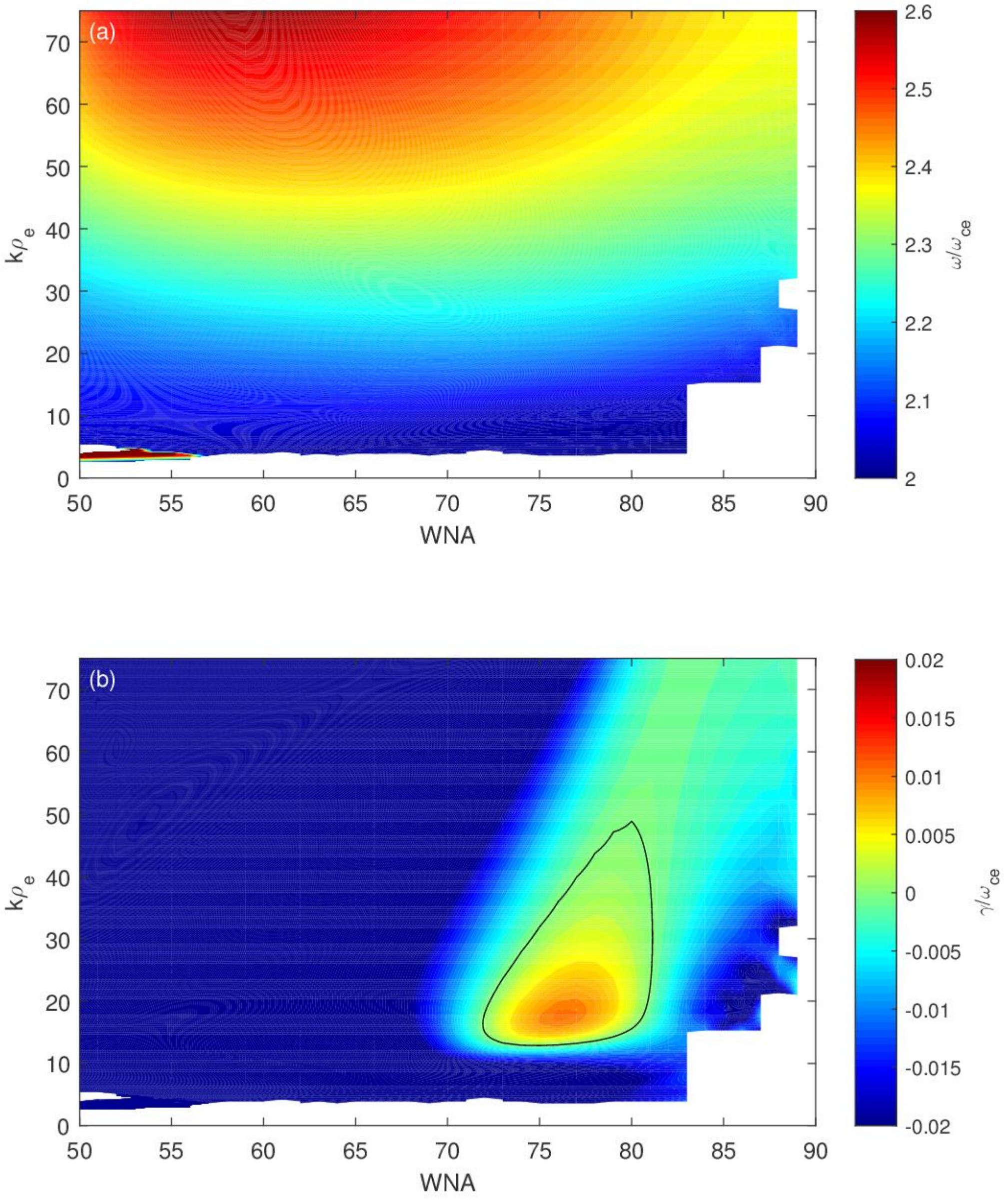

Figure 6.3: Dispersion relations and the growth rate for beam-driven ECH waves at the second harmonic frequency band. Input plasma parameters are listed in Table 6.2. The horizontal axis is the wave normal angle; the vertical axis is the wave vector normalized to the gyroradius of the first component in Table 6.2. Figures 6.3(a) and 6.3(b) show the wave frequency and growth rate normalized to the electron cyclotron frequency.

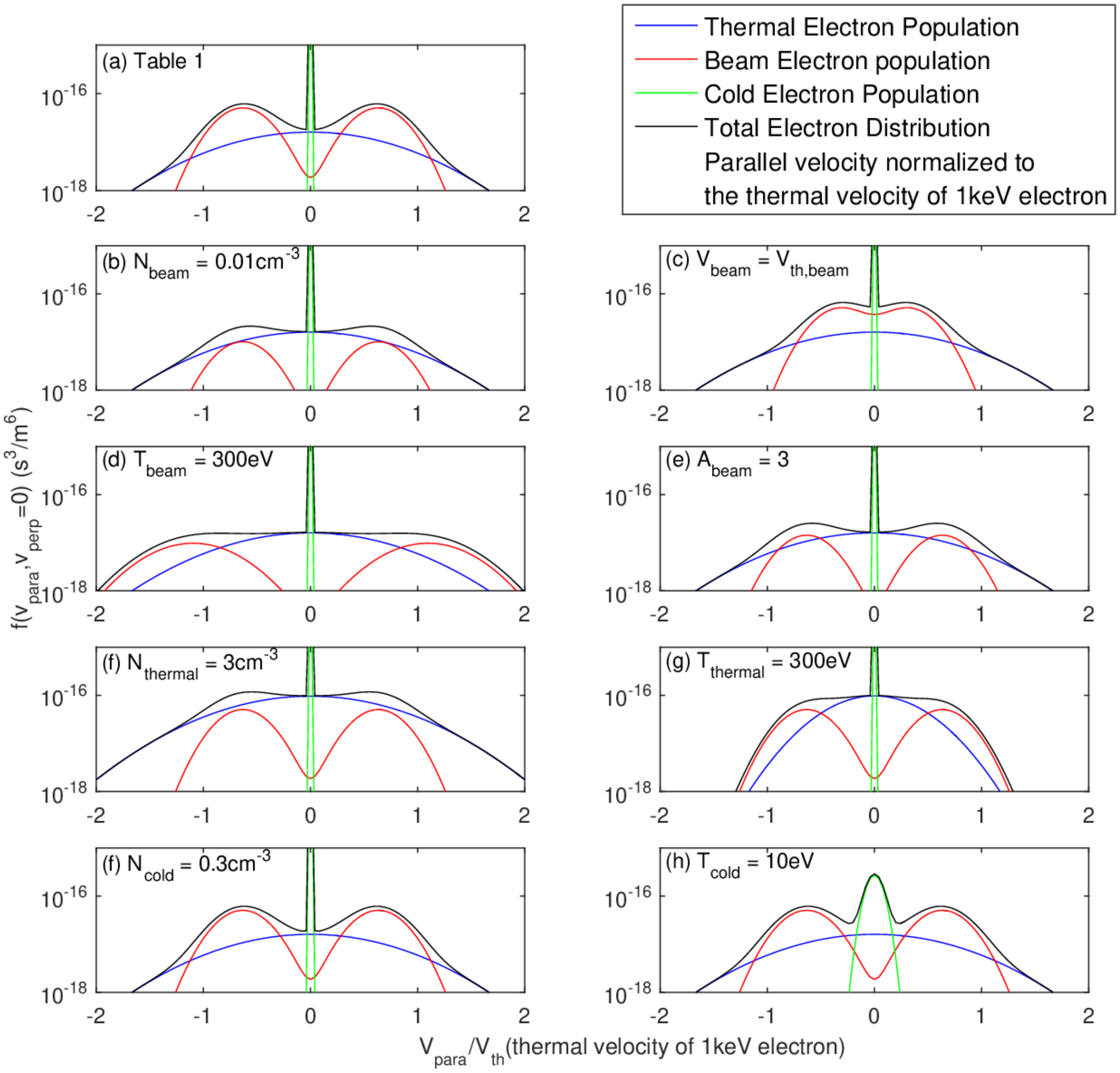

Figure 6.4: The electron phase space density as a function of parallel velocity with zero perpendicular velocity. The parallel velocity is normalized to the thermal velocity of a 1keV electron. We use the electron plasma parameters listed in Table 6.1 and vary a parameter at one time for each figure. (a): Plasma parameters in Table 6.1; (b): The beam density is changed to $0.01cm^{-3}$; (c): The normalized beam velocity is changed to 1; (d): The beam temperature is changed to 300eV; (e): The temperature anisotropy is changed to 3; (f): The hot electron density is changed to $3cm^{-3}$; (g): The hot electron temperature is changed to 300eV; (f): The cold electron density is changed to $0.3cm^{-3}$; (h): The cold electron temperature is changed to 10eV.

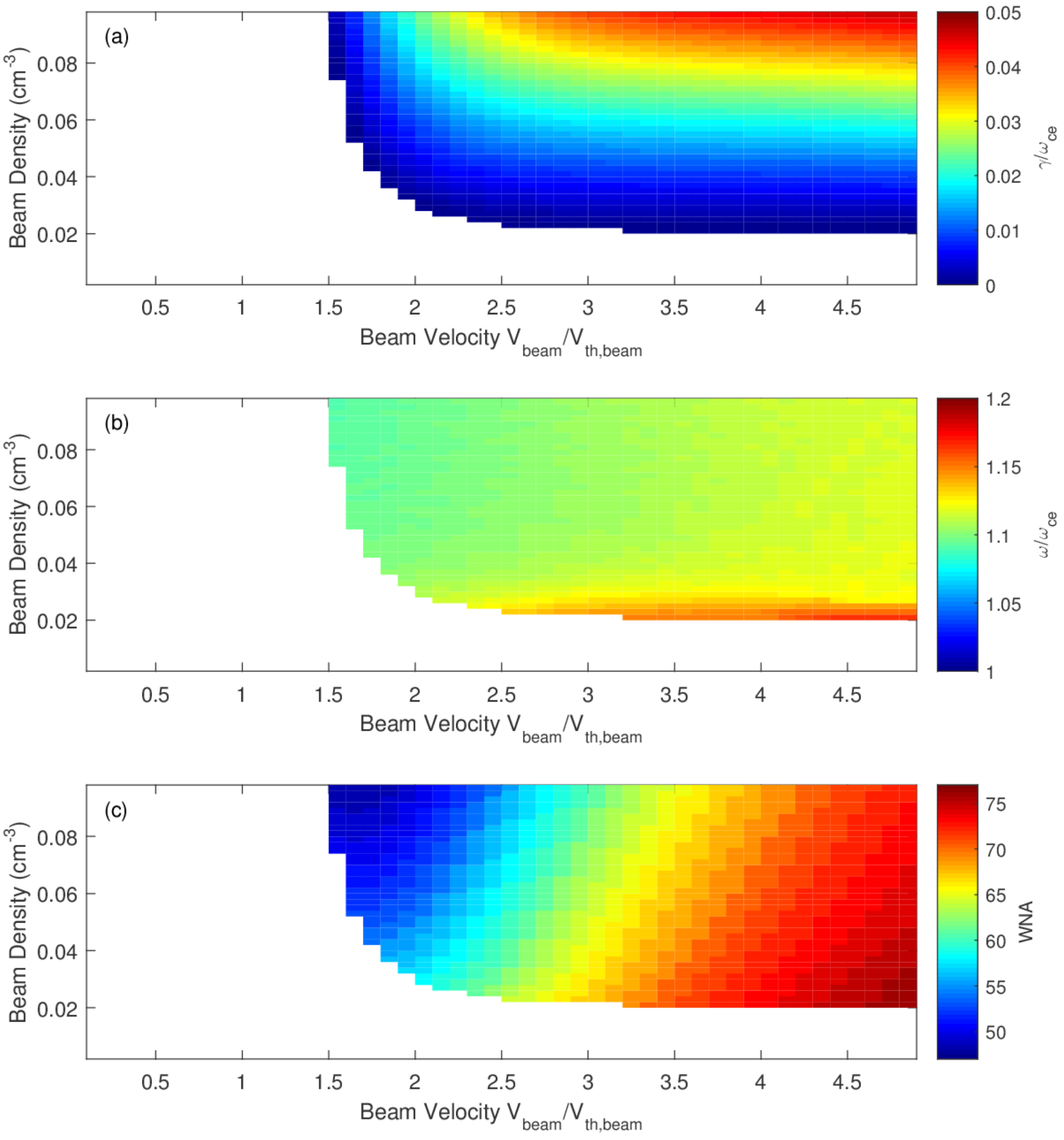

Figure 6.5: A total of 50x50 data points are in this parameter space. Each data point represents wave properties corresponding to the maximum growth rate. (a): Normalized growth rate as a function of beam velocity and beam density. The beam velocity is normalized to the thermal velocity of the beam; (b): The wave frequency is normalized to the electron cyclotron frequency; (c): Wave normal angle.

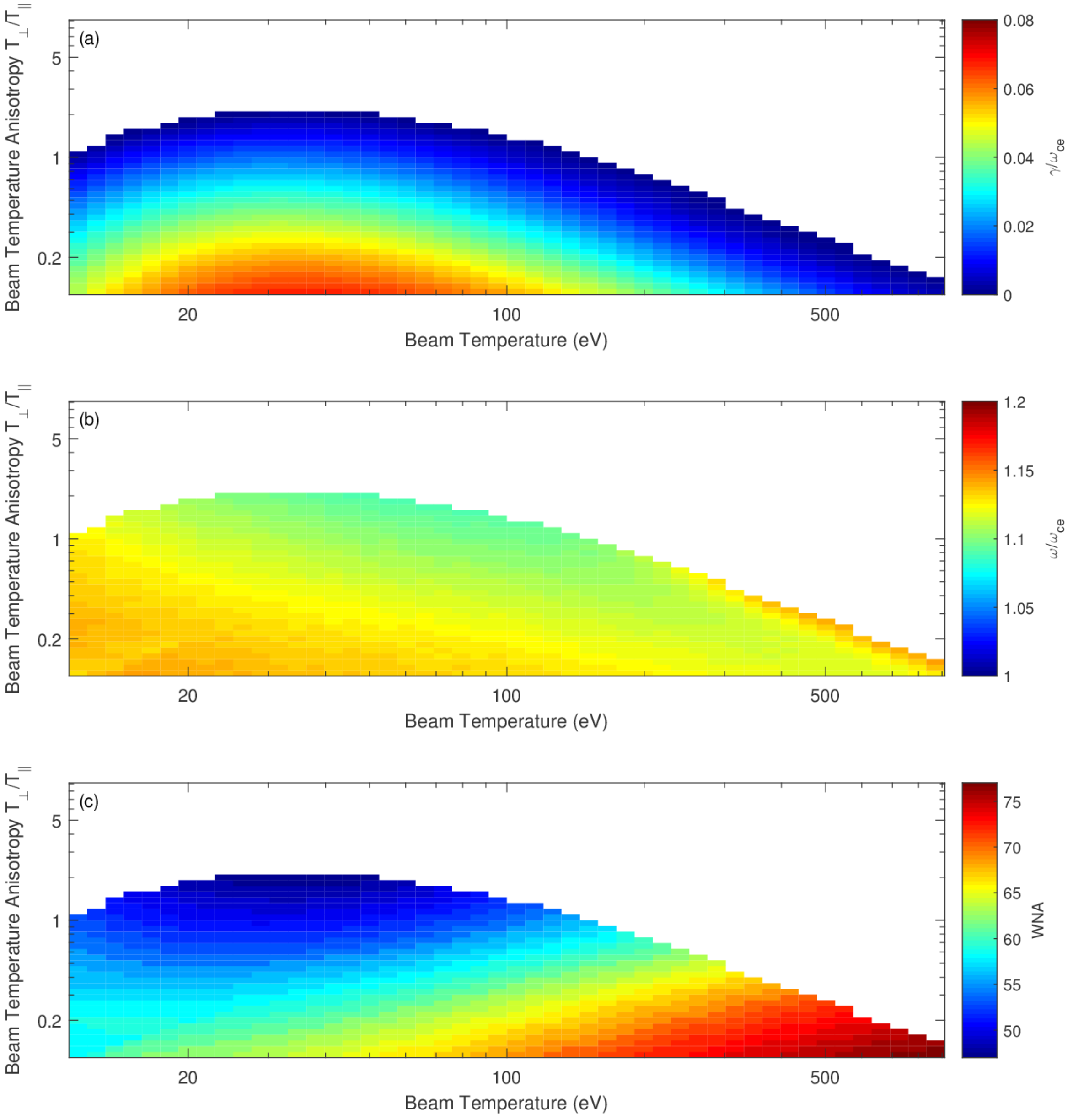

Figure 6.6: The figure format is the same as Figure 6.5. Horizontal axis is beam temperature in the parallel direction and vertical axis is beam temperature anisotropy defined as the ratio between perpendicular and parallel beam temperature.

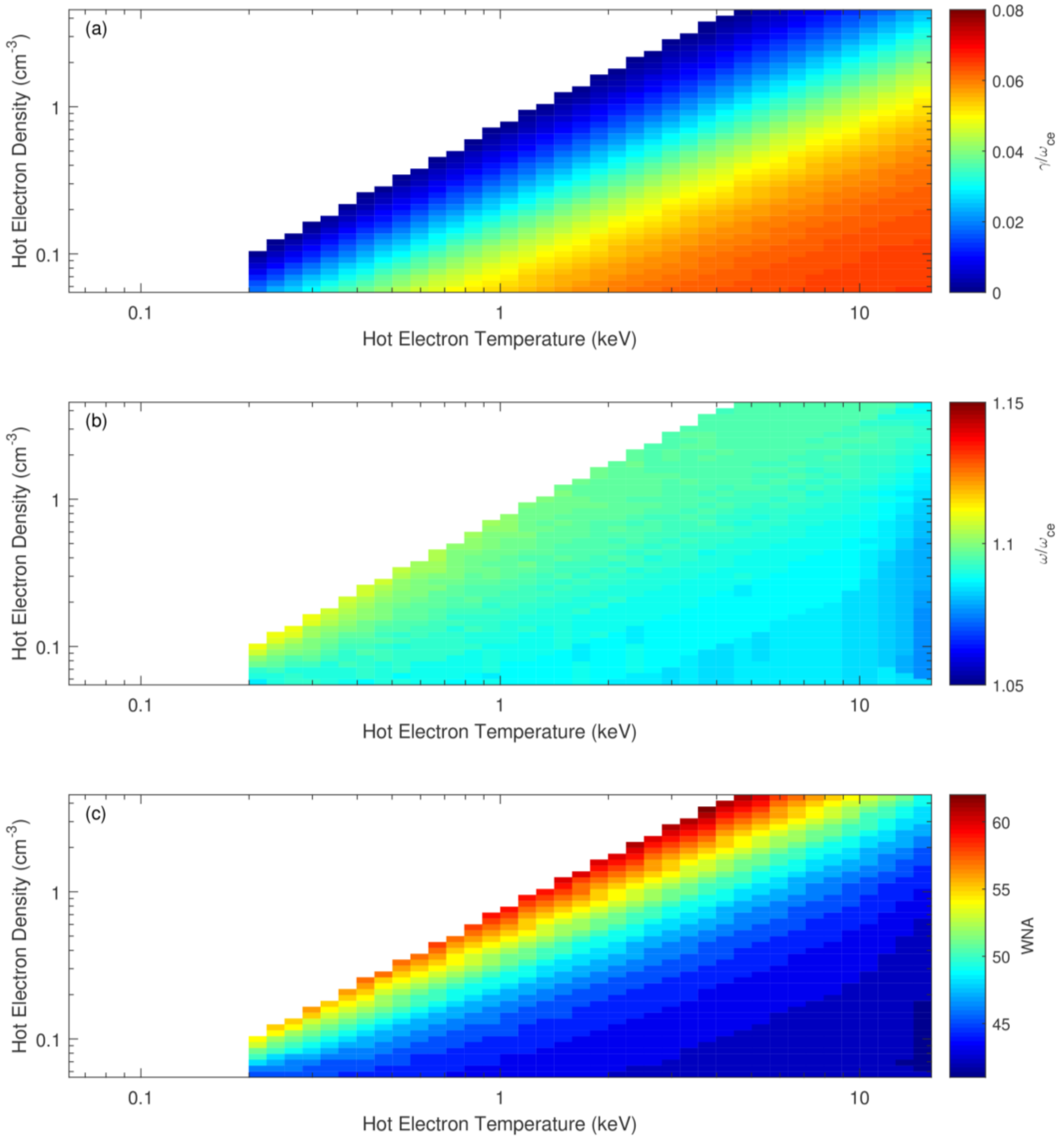

Figure 6.7: The figure format is the same as in Figure 6.5. The horizontal axis is the temperature of the hot electron component; the vertical axis is the density of the hot electron component.

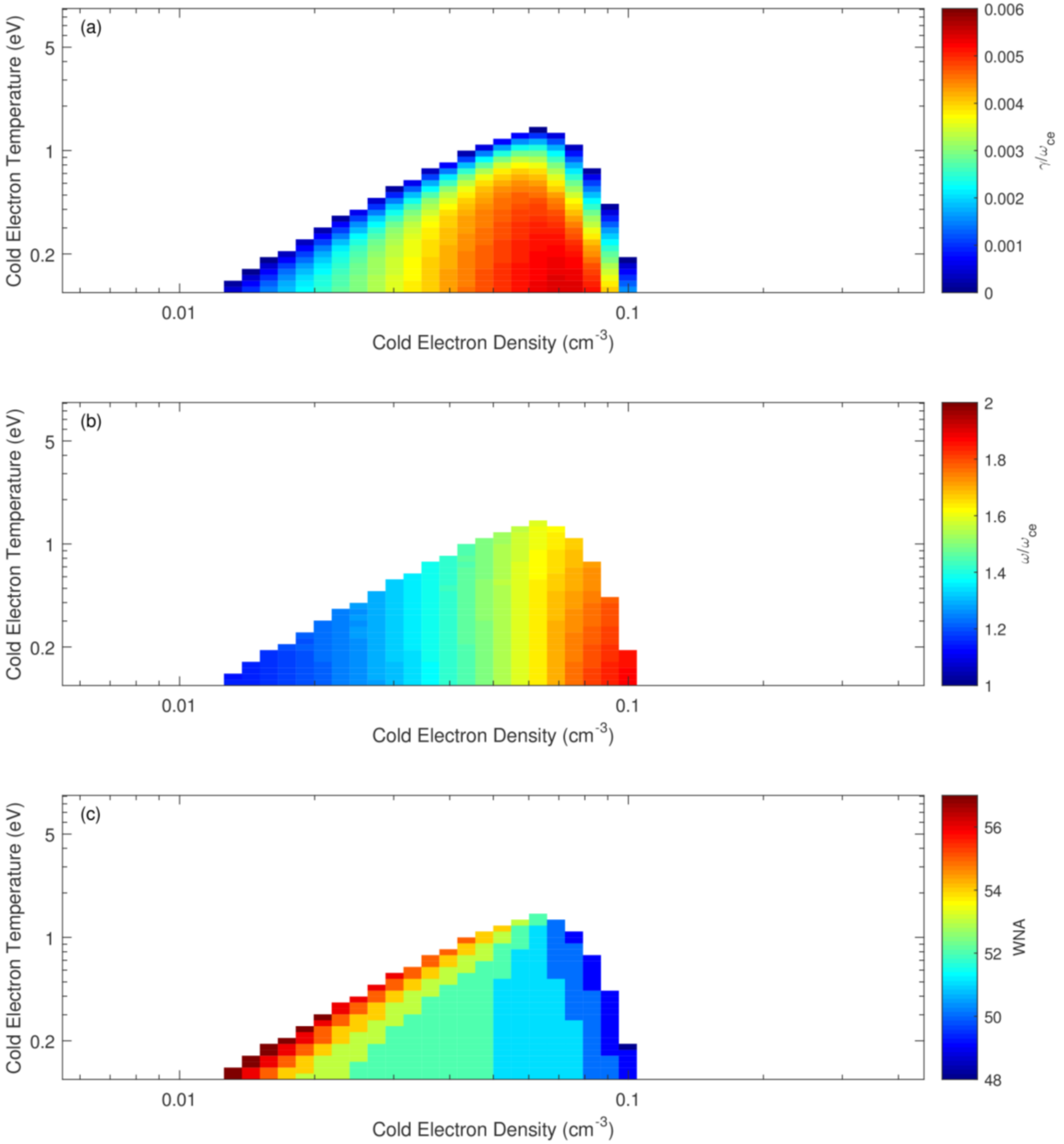

Figure 6.8: The figure format is the same as in Figure 6.5. The horizontal axis is the density of the cold electron component, and the vertical axis is the temperature of the cold electron component.

Table 6.1 Electron distribution function

Component	n (cm^{-3})	$T_{||}$ (eV)	$T_{\perp}/T_{\parallel}$	$V_{drift}/V_{thermal}$
1 Hot electron	0.5	1000	0.85	0
2 Cold electron	0.01	0.1	1	0
3 Electron beam	0.05	100	0.85	2
4 Electron beam	0.05	100	0.85	-2

Table 6.2 Electron distribution function

Component	n (cm^{-3})	$T_{\|\|}$ (eV)	$T_{\perp}/T_{\parallel}$	$V_{drift}/V_{thermal}$
1	0.5	1000	0.85	0
2	0.08	0.2	1	0
3	0.05	100	0.85	5
4	0.05	100	0.85	-5

Chapter 7

Summary and Future Work

7.1 Summary

In this dissertation, we systematically investigate different types of electron driven instabilities in and around dipolarizing flux bundles. Unstable electron distributions can form near dipolarization fronts and provide the free energy sources for plasma wave generation. These electron driven instabilities can, in turn, modify the electron distribution functions through wave-particle interaction. By investigating the generation mechanisms of these electron driven instabilities and the effectiveness of these instabilities on regulating electron dynamics, our understanding of the relations between dipolarization fronts and plasma waves are greatly improved.

In Chapter 1, we introduce the basic theory of wave-particle interaction. We briefly discuss the properties of low frequency waves (current-driven kink-like instability and kinetic Alfvén waves), whistler waves and electron cyclotron harmonic waves. These electron driven instabilities are extensively investigated in this dissertation.

In Chapter 2, L. In the simulations, these instabilities are located at the plasma sheet boundary layer, just ahead of approaching dipolarization fronts and are driven unstable by electron currents. Using observations by two THEMIS satellites, we select one case for further study. Two different instabilities, one at about 0.3 Hz and the other at a much lower frequency, 0.02 Hz, were seen in the data from the off-equatorial spacecraft. A parallel current attributed to an electron beam coexisted with the waves. Our instability analysis attributes the higher-frequency instability to a current-driven ion cyclotron instability and the lower-frequency instability to a kink-like instability. We suggest that the currents needed to excite these low-frequency instabilities are so intense that the associated electron beams are easily thermalized and hence difficult to observe.

We focus on whistler waves near dipolarization fronts in Chapter 3 and 4 and emphasize the importance of whistler waves on regulating electron dynamics near dipolarization fronts. In Chapter 3, we explore the occurrence probability and intensity of whistler instability and oblique electron firehose instability near dipolarization fronts as function of electron anisotropy and plasma beta, using 10 years of THEMIS observational data. Electron temperature anisotropies are well-constrained by the marginal stability conditions of the whistler and oblique electron firehose instabilities. In fact, the observed enhancement of magnetic field fluctuations near the instability thresholds provides good evidence for the operation of these instabilities on electrons near fronts. Since the build-up of electron anisotropy is limited by wave-particle interactions, we conclude that such interactions are important enough to affect electron dynamics and energetics.

In Chapter 4, we investigate whistler wave excitation within and around dipolarizing flux bundles (DFBs), critical energy transporters in the magnetotail, and the evacuation of perpendicular electron energy by whistler wave Poynting flux using THEMIS observations. We find that perpendicular anisotropy of suprathermal (~10keV) electrons is the major free energy source for whistler wave excitation near DFBs. This suggests that whistler wave excitation near DFs is a kinetic process involving multi-component electrons exhibiting different anisotropy levels as a function of energy. During earthward transport of electrons by DFBs, 3.7% of the suprathermal electron energy flux increases is evacuated in the form of whistler wave Poynting flux. We reveal the importance of whistler waves energetically from the point of view of radiating electron energy flux. The results in Chapter 3 and Chapter 4 suggest that whistler waves play an important role in electron thermodynamics in the magnetotail by significantly modifying the otherwise adiabatically-shaped electron distributions.

We explore the generation mechanisms of ECH waves near dipolarization fronts in Chapter 5 and Chapter 6. In Chapter 5, we investigate ECH wave properties near dipolarization fronts, the predominant source of such waves. To our surprise we find that more than 30% of observed ECH waves have moderately oblique (~70^0) wave normal angles (WNA), much less than the ~85º expected from classical loss-cone instability. These moderately oblique WNA ECH waves carry a strong field-aligned electric field that is used to identify them. They are often observed with cold, dense electrons that exhibit enhanced parallel flux at a few hundred eV energy, which suggests that low-energy counterstreaming beams (likely of ionospheric origin) might be their free energy source. By solving the linear dispersion relation for parameters representative of such plasma sheet electron distributions, we confirm that ECH waves at WNA ~ 70º can indeed be driven unstable by such beams. Our work reveals a previously unknown excitation mechanism for ECH waves and exposes the need for quantifying the conditions for and relative importance of beam-driven waves compared to those excited by the loss-cone instability in Earth's plasma sheet.

In Chapter 6, we investigate the ambient and beam plasma conditions under which beam driven ECH waves can be excited. Knowledge of such conditions would allow us to further explore the relative contribution of this excitation mechanism to ECH wave scattering of magnetospheric electrons at Earth and the outer planets. Using the hot plasma dispersion relation, we address the nature of beam-driven ECH waves and conduct a comprehensive parametric survey of this instability. We find that growth is provided by beam electron cyclotron resonances of both first and higher orders. We also find that these waves are unstable under a wide range of plasma conditions. The growth rate increases with beam density, beam velocity, and hot electron temperature; it decreases with increasing beam temperature and beam temperature anisotropy ($T_\perp/T_\parallel$), hot electron density, and cold electron density and temperature. Such conditions abound in Earth's magnetotail, where magnetospheric electrons heated by earthward convection and magnetic reconnection coexist with colder ionospheric electrons. The loss-cone distribution is not the only free energy source for ECH waves in the plasma sheet. In chapter 5 and chapter 6, we provide both observational and theoretical evidence on the generation of ECH waves by low energy electron beams.

When we analyze the interaction of plasma waves with unstable particles near dipolarization fronts in the dissertation, we assume that the zero-order particle distributions remain unchanged during their interactions with plasma waves. Since we only take into account the linear theory of wave-particle interaction, the growth rates we obtain from our instability analysis ($\gamma = 10^{-3} \sim 10^{-2}\Omega_{ce}$ for whistler waves and ECH waves) are too small and are comparable to the time-scales of the extremely dynamic environments near dipolarization fronts. The small growth rates we obtain from the linear theory, however, do not undermine our previous assumption. Due to the time-cadence of our particle measurements (3-second), the unstable particle distributions that excite plasma waves might contain much larger free energy than the free energy in particle distributions from measurements. The wave measurements, which have much shorter time cadences, can therefore be used as good tracers of unstable particle distributions, Moreover, both the plasma waves and particle distributions from spacecraft measurements are already near the marginal stability state where the wave energy saturates. The initial stage where plasma waves are excited by unstable particle distributions is difficult to observe due to fast growth of plasma waves. It can be investigated in more details in simulations where non-linear wave-particle interactions are revealed.

7.2 Future work

7.2.1 Landau and cyclotron resonance between whistler waves and electrons near dipolarization fronts

As demonstrated in Chapter 4, the perpendicular anisotropy of the suprathermal electron population is the major free energy source for whistler wave generation. During whistler wave excitation, energy of the suprathermal electron population is transferred to whistler waves through cyclotron resonance. When whistler waves interact with electrons through Landau resonance, energy can be transferred from whistler waves to electrons at different energies. Our goal is to quantify the efficiency of energy transfer between whistler waves and electrons through both Landau and cyclotron resonance.

In terms of cyclotron resonance, we can calculate the electron phase space density gradient along the diffusion curve defined by Eq 1.4 in Section 1.3. It is expressed as:

$$\frac{\partial f}{\partial v_R}dv = (\frac{\partial f}{\partial v_{||}} - \frac{v_{\parallel} - v_{ph}}{v_{\perp}}\frac{\partial f}{\partial v_{\perp}})dv_{\parallel} \tag{7.1}$$

where v_R is the resonance velocity calculated from the cyclotron resonance condition; v_{ph} is the phase velocity of whistler waves. Eq 7.1 can be further expressed as a function of $\partial f/\partial E$ and $\partial f/\partial \alpha$ (E is electron energy and α is electron pitch angle). Since $\partial f/\partial E$ and $\partial f/\partial \alpha$ can be obtained from observational data, we are able to quantify the efficiency of energy transfer between whistler waves and electron through cyclotron resonance.

In terms of Landau resonance, we can calculate the electron phase density gradient when $v_{||} = v_{ph}$. It is expressed as

$$\frac{\partial f}{\partial v_R} = \frac{\partial f}{\partial v_{||}}|_{v_{\parallel}=\omega/k} \tag{7.2}$$

It can also be further expressed as a function of $\partial f/\partial E$ and $\partial f/\partial \alpha$ and be obtained from observational data.

Positive results obtained from Eq 7.1 indicate that whistler waves gain energy from electrons through cyclotron growth. Negative values from Eq 7.2 indicate that whistler waves are damped due to Landau resonance. It can greatly improve our understanding of the energy transfer process between whistler waves and electrons near dipolarization fronts.

7.2.2 Beam-driven ECH waves in other regions of Earth's magnetosphere

As demonstrated in Chapter 5, ECH waves with moderately oblique wave normal angles observed behind dipolarization fronts are driven unstable by low energy electron beams. These low energy electron beams are likely to be ionospheric origins and could be (1) secondary electrons produced by precipitating plasma sheet electrons [Khazanov et al., 2014; Artemyev et al., 2020]; (2) upward electron beams accelerated by an electric field parallel to the magnetic field and near downward field-aligned currents [Carlson et al., 1998; Hull et al. 2020]. The presence of fast plasma sheet flows and dipolarization fronts is not the necessary condition for the generation of the ionospheric electron beams. They have also been observed during quiet time plasma sheet [Walsh et al., 2013; Artemyev et al., 2015]. The low energy electron beams have also been observed in the outer radiation belt [Kellogg et al., 2011; Mourenas et al., 2015]. Our study on beam-driven ECH waves should not be restrained to regions inside dipolarizaing flux bundles. We could expand our beam-driven ECH wave database in Chapter 5 to quiet time magnetotail when no dipolarization fronts are observed. Our parametric study in Chapter 6 demonstrates that beam-driven ECH waves can be unstable under a wide range of plasma conditions with electron plasma beta value ranging from 0.003 to 12.9. Therefore, it is worth investigating the existence of beam-driven ECH waves in quite time magnetotail and in inner magnetosphere. Investigating beam-driven ECH waves in other regions of Earth's magnetosphere can improve our understanding of this rarely discussed generation mechanism of ECH waves.

7.2.3 Evaluating the pitch-angle diffusion coefficients for beam-driven ECH waves

Electron cyclotron harmonic (ECH) waves play a significant role in driving the diffuse aurora, which constitutes more than 75% of the particle energy input into the ionosphere. It is generally accepted nowadays that ECH waves play an important role in scattering plasma electrons into the loss cone and in driving diffuse aurora in the outer magnetosphere beyond eight Earth radii in the magnetotail [Ni et al., 2011b, 2012, 2016, Zhang et al., 2013, 2015]. Quantifying the effectiveness of ECH waves in scattering plasma sheet electrons and driving diffuse aurora rely on the calculation of the pitch-angle diffusion coefficient. The pitch-angle diffusion coefficient for electrostatic ECH waves is given by the equation below [Lyons 1974]:

$$D_{\alpha\alpha} = \sum_{n=-\infty}^{\infty} k_{\perp} dk_{\perp} \cdot [\Psi_{n,k} \left(\frac{n\Omega_e/\omega_k - sin^2\alpha}{sin\alpha\ cos\alpha} \right)^2]_{k_{\parallel}=k_{res}} \tag{7.3}$$

$$\Psi_{n,k} = \frac{1}{4\pi} \frac{e^2}{m_e^2} \frac{|E_k|^2}{V} (\frac{\omega_k}{k})^2 \frac{J_n^2(k_{\perp} v_{\perp}/\Omega_e)}{v^4 |v_{\parallel} - \partial\omega_k/\partial k_{\parallel}\ |} \tag{7.4}$$

where k_{res} is the wave number calculated from the resonance condition, ω_k is the wave frequency, α is pitch angle, E_k is the wave electric field, V is the plasma volume, J_n is the Bessel function of order n.

Because wave normal angle is an important parameter in evaluating the pitch-angle diffusion coefficients for ECH waves, the pitch-angle diffusion coefficient profile as a function of equatorial pitch angle and energy for beam-driven ECH waves might be different from the profile for loss cone-driven ECH waves. In our future work, we plan to evaluate the pitch-angle diffusion coefficient for beam-driven ECH waves. Knowledge of such profile can improve our understanding of the effectiveness of beam-driven ECH waves on scattering plasma sheet electrons and driving diffusive aurora.

7.2.4 Kinetic Alfvén waves observed near dipolarization fronts

Kinetic Alfvén waves (KAWs), Alfvén waves with perpendicular wavelength comparable to the ion gyroradius, have been observed to be associated with BBFs and DFs [Chaston et al., 2012]. Previous observations have demonstrated that Poynting flux of KAWs represented a significant portion of the energy transport in BBFs and it is sufficient to account for the auroral energy decomposition during substorms [Wygant et al., 2000; Angelopoulos et al., 2002; Chaston et al., 2012]. The correlation between KAWs and DFs, however, is still not well understood.

Figure 3.1(f), 3.1(h), 3.1(i) in Chapter 3 demonstrated an example of broadband and non-monochromatic electromagnetic fluctuations observed behind dipolarization fronts. Assuming that the wave frequency observed in the spacecraft frame is mainly due to the Doppler-shift of KAWs by the plasma flows, we compared the observed E-to-B ratio with theoretical expectation for KAWs [Stasiewicz et al., 2000]. Consistency between observations and theory suggests that KAWs are a good candidate for broadband electromagnetic waves observed near DFs. In our future work, we plan to establish a KAW event database in our DFB event list. To identify KAWs, we would like to first select broadband electromagnetic wave events from magnetic field power spectra. By calculating E-to-B ratios and comparing it with theoretical expectations, we can confirm that the observed broadband electromagnetic waves are KAWs. Utilizing the database of KAWs identified near dipolarization fronts, we plan to address questions like how frequent KAWs are observed near DFBs and what the characteristics of the Poynting flux and field-aligned currents associated with KAWs in our future work.

BIBLIOGRAPHY

Agapitov, O., A. Artemyev, V. Krasnoselskikh, Y. V. Khotyaintsev, D. Mourenas, H. Breuillard, M. Balikhin, and G. Rolland (2013), Statistics of whistler-mode waves in the outer radiation belt: Cluster STAFF-SA measurements, J. Geophys. Res. Space Physics, 118, 3407–3420, doi:10.1002/jgra.50312.

Agapitov, O., A. Artemyev, D. Mourenas, V. Krasnoselskikh, J. Bonnell, O. Le Contel, C. M. Cully, and V. Angelopoulos (2014), The quasi-electrostatic mode of chorus waves and electron nonlinear acceleration, J. Geophys. Res. Space Physics, 119, 1606–1626, doi: 10.1002/2013JA019223.

Agapitov, O. V., D. Mourenas, A. V.Artemyev, and F. S. Mozer (2016), Exclusion principle for very oblique and parallel lower band chorus waves, Geophys. Res. Lett., 43, 11,112–11,120, doi: 10.1002/2016GL071250.

Agapitov, O., Drake, J. F., Vasko, I., Mozer, F. S., Artemyev, A., Krasnoselskikh, V., & Reeves, G. D. (2018). Nonlinear electrostatic steepening of whistler waves: The guiding factors and dynamics in inhomogeneous systems. Geophysical Research Letters, 45, 2168– 2176. https://doi.org/10.1002/2017GL076957

An, X., C. Yue, J. Bortnik, V. Decyk, W. Li, and R. M. Thorne (2017), On the parameter dependence of the whistler anisotropy instability, J. Geophys. Res. Space Physics, 122, 2001–2009, doi: 10.1002/2017JA023895.

Angelopoulos, V., W. Baumjohann, C. F. Kennel, F. V. Coroniti, M. G. Kivelson, R. Pellat, R. J. Walker, H. Luehr, and G. Paschmann (1992), Bursty bulk flows in the inner central plasma sheet, J. Geophys. Res., 97, 4027–4039.

Angelopoulos, V., et al. (1994), Statistical characteristics of bursty bulk flow events, J. Geophys. Res., 99, 21,257–21,280, doi: 10.1029/94JA01263.

Angelopoulos, V., Chapman, J. A., Mozer, F. S., Scudder, J. D., Russell, C. T., Tsuruda, K., Mukai, T., Hughes, T. J., & Yumoto, K. (2002). Plasma sheet electromagnetic power generation and its dissipation along auroral field lines. Journal of Geophysical Research, 107, 1181. doi: 10.1029/2001JA900136.

Angelopoulos, V., McFadden, J. P., Larson, D., Carlson, C. W., Mende, S. B., et al. (2008). Tail reconnection triggering substorm onset. Science, 321, 931–935.doi: /10.1126/science.1160,495

Angelopoulos, V. (2008), The THEMIS mission, Space Sci. Rev., 141, 5–34, doi: 10.1007/s11214-008-9336-1.

Angelopoulos, V., A. Runov, X.-Z. Zhou, D. L. Turner, S. A. Kiehas, S.-S. Li, and I. Shinohara (2013), Electromagnetic energy conversion at reconnection fronts, Science, 341, 1478–1482, doi:10.1126/science.1236992.

Angelopoulos, V., et al. (2019) The Space Physics Environment Data Analysis System (SPEDAS), Space Sci Rev 215: 9. doi: /10.1007/s11214-018-0576-4

Artemyev, A. V., Zelenyi, L. M., Petrukovich, A. A., and Nakamura, R. (2011), Hot electrons as tracers of large-scale structure of magnetotail current sheets, Geophys. Res. Lett., 38, L14102, doi: 10.1029/2011GL047979, 2011.

Artemyev, A. V., A. A. Petrukovich, R. Nakamura, and L. M. Zelenyi (2013), Profiles of electron temperature and Bz along Earth's magnetotail, Ann. Geophys., 31, 1109–1114.

Artemyev, A. V., O. V. Agapitov, F. Mozer, and V. Krasnoselskikh (2014a), Thermal electron acceleration by localized bursts of electric field in the radiation belts, Geophys. Res. Lett., 41, 5734–5739, doi: 10.1002/2014GL061248.

Artemyev, A. V., A. P. Walsh, A. A. Petrukovich, W. Baumjohann, R. Nakamura, and A. N. Fazakerley (2014b), Electron pitch angle/energy distribution in the magnetotail, J. Geophys. Res. Space Physics, 119, 7214–7227, doi: 10.1002/2014JA020350.

Artemyev, A. V., R. Rankin, and M. Blanco (2015), Electron trapping and acceleration by kinetic Alfvén waves in the inner magnetosphere, J. Geophys. Res. Space Physics, 120, 10,305–10,316, doi:10.1002/2015JA021781.

Artemyev, A.V., I. Y. Vasko, V. Angelopoulos, and A. Runov (2016), Effects of electron pressure anisotropy on current sheet configuration, Physics of Plasmas, 23 (9), 092901. doi: 10.1063/1.4961926

Artemyev, A.V., Zhang, X.-J., Angelopoulos, V., Mourenas, D., Vainchtein, D., Shen, Y., Vasko, I., and Runov, A. "Ionosphere feedback to electron scattering by equatorial whistler mode waves," J. Geophys. Res.: Space Phys., 125, e2020JA028373 (2020) doi: 10.1029/2020JA028373

Ashour-Abdalla, M., and C. F. Kennel (1978), Nonconvective and convective electron cyclotron harmonic instabilities, J. Geophys. Res., 83(A4), 1531-1543.

Ashour-Abdalla, M., C.F. Kennel, and W. Livesey (1979), A parametric study of electron multiharmonic instabilities in the magnetosphere, J. Geophys. Res., 84(A11), 6540-6546, doi: 10.1029/JA084iA11p06540.

Ashour-Abdalla, M., El-Alaoui, M., Goldstein, M. L., Zhou, M., Schriver, D., Richard, R., et al. (2011). Observations and simulations of non-local acceleration of electrons in magnetotail magnetic reconnection events. Nature Physics, 7 (4), 360–365. doi: 10.1038/nphys1903

Auster, H. U., et al. (2008), The THEMIS fluxgate magnetometer, Space Sci. Rev., 141, 235–264, doi: 10.1007/s11214-008-9365-9.

Bale, S. D., J. C. Kasper, G. G. Howes, E. Quataert, C. Salem, and D. Sundkvist (2009), Magnetic fluctuation power near proton temperature anisotropy instability thresholds in the solar wind, Phys. Rev. Lett., 103(21), 211101, doi:10.1103/PhysRevLett.103.211101

Baumjohann, W., G. Paschmann, and H. Luehr (1990), Characteristics of high-speed ion flows in the plasma sheet, J. Geophys. Res., 95, 3801–3809, doi: 10.1029/JA095iA04p03801.

Baumjohann, W., M. Hesse, S. Kokubun, T. Mukai, T. Nagai, and A. A. Petrukovich (1999), Substorm dipolarization and recovery, J. Geophys. Res., 104, 24,995–25,000.

Belmont, G., D. Fontaine, and P. Canu (1983), Are equatorial electron cyclotron waves responsible for diffuse auroral electron precipitation? J. Geophys. Res., 88(A11), 9163–9170, doi: 10.1029/JA088iA11p09163.

Birn, J., and M. Hesse (2005), Energy release and conversion by reconnection in the magnetotail, Ann. Geophys., 23, 3365–3373.

Birn, J., M. Hesse, R. Nakamura, and S. Zaharia (2013), Particle acceleration in dipolarization events, J. Geophys. Res. Space Physics, 118, 1960–1971, doi:10.1002/jgra.50132.

Birn, J., A. Runov, and M. Hesse (2014), Energetic electrons in dipolarization events: Spatial properties and anisotropy, J. Geophys. Res. Space Physics, 119, 3604–3616, doi: 10.1002/2013JA019738.

Bonnell, J. W., Mozer, F. S., Delory, G. T., Hull, A. J., Ergun, R. E., Cully, C. M., et al. (2008). The electric field instrument (EFI) for THEMIS.Space Science Reviews, 141, 303–341.

Bortnik, J., R.M. Thorne (2007), The dual role of ELF/VLF chorus waves in the acceleration and precipitation of radiation belt electrons. J. Atmos. Sol.-Terr. Phys. 69, 378–386. doi:10.1016/j.jastp.2006.05.030

Bortnik, J., Thorne, R. & Meredith, N (2008). The unexpected origin of plasmaspheric hiss from discrete chorus emissions. Nature 452, 62–66. https://doi.org/10.1038/nature06741

Breuillard, H., et al. (2016), Multi spacecraft analysis of dipolarization fronts and associated whistler wave emission susing MMS data, Geophys. Res. Lett., 43, 72797286, doi: 10.1002/2016GL069188.

Burton, R.K., Holzer, R.E (1974), The origin and propagation of chorus in the outer magnetosphere. J. Geophys. Res. 79, 1014–1023 (1974). doi:10.1029/JA079i007p01014

Carlson, C. W., McFadden, J. P., Ergun, R. E., Temerin, M., Peria, W., Mozer, F. S., Klumpar, D. M., Shelley, E. G., Peterson, W. K., Moebius, E., Elphic, R., Strangeway, R., Cattell, C., Pfaff, R., "FAST observations in the downward auroral current region: Energetic upgoing electron beams, parallel potential drops, and ion heating”. Geophys. Res. Lett., 25, 2017– 2020 (1998). https://doi.org/10.1029/98GL00851

Camporeale, E., and D. Burgess (2008), Electron firehose instability: Kinetic linear theory and 2D particle-in-cell simulations, J. Geophys. Res., 113, A07107, doi: 10.1029/2008JA013043.

Chaston, C. C., C. W. Carlson, R. E. Ergun, and J. P. McFadden (2000), Alfvén waves, density cavities and electron acceleration observed from the FAST spacecraft, Phys. Scr. T, 84, 64–68.

Chaston, C. C., J. W. Bonnell, L. Clausen, and V. Angelopoulos (2012), Energy transport by kinetic-scale electromagnetic waves in fast plasma sheet flows, J. Geophys. Res., 117, A09202, doi: 10.1029/2012JA017863

Chen, C. X., and R. A. Wolf (1993), Interpretation of high-speed flows in the plasma sheet, J. Geophys. Res., 98, 21,409, doi:10.1029/93JA02080.

Chen, L., and D. J. Wu (2010), Kinetic Alfvén wave instability driven by electron temperature anisotropy in high-plasmas, Phys. Plasmas, 17, 62107, doi:10.1063/1.3439680.

Cully, C. M., R. E. Ergun, K. Stevens, A. Nammari, and J. Westfall (2008), The THEMIS digital fields board, Space Sci. Rev., 141, 343 – 355, doi: 10.1007/s11214-008-9417-1.

Daughton, W. (2003), Electromagnetic properties of the lower-hybrid drift instability in a thin current sheet, Phys. Plasmas, 10, 3103–3119.

Deng, X., M. Ashour-Abdalla, M. Zhou, R. Walker, M. El-Alaoui, V. Angelopoulos, R. E. Ergun, and D. Schriver (2010), Wave and particle characteristics of earthward electron ejections associated with dipolarization fronts, J. Geophys. Res., 115, A09225, doi: 10.1029/2009JA015107.

Eastwood, J. P., T.-D. Phan, M. Øieroset, and M. A. Shay (2010), Average properties of the magnetic reconnection ion diffusion region in the Earth's magnetotail: The 2001–2005 Cluster observations and comparison with simulations, J. Geophys. Res., 115, A08215, doi: 10.1029/2009JA014962.

Eastwood, J. P., T. D. Phan, J. F. Drake, M. A. Shay, A. L. Borg, B. Lavraud, and M. Taylor (2013), Energy partition in magnetic reconnection in Earth's magnetotail, Phys. Rev. Lett., 110(22), 5, doi: 10.1103/PhysRevLett.110.225001

Ergun, R. E., Carlson, C. W., McFadden, J. P., Mozer, F. S., Delory, G. T., Peria, W., et al. (1998). FAST satellite observations of large-amplitude solitary structures. Geophysical Research Letters, 25, 2041– 2044. https://doi.org/10.1029/98GL00636

Ergun, R. E., Su, Y.-J., Andersson, L., Carlson, C. W., McFadden, J. P., Mozer, F. S., et al. (2001). Direct observation of localized parallel electric fields in a space plasma. Physical Review Letters, 8**7**(4), 045003. https://doi.org/10.1103/PhysRevLett.87.045003

Ergun, R. E., K. A. Goodrich, J. E. Stawarz, L. Andersson, and V. Angelopoulos (2014), Large-amplitude electric fields associated with burst y bulk flow braking in the Earth's plasma sheet, J. Geophys.Res. Space Physics, 120, 1832–1844, doi: 10.1002/2014JA020165.

Eshetu, W. W., Lyon, J. G., Hudson, M. K., & Wiltberger, M. (2018), Pitch angle scattering of energetic electrons by BBFs. Journal of Geophysical Research: Space Physics, 123, 9265–9274. doi: 10.1029/2018JA025788

Fontaine, D., and M. Blanc (1983), A theoretical approach to the morphology and the dynamics of diffuse auroral zones, J. Geophys. Res., 88(A9), 7171-7184.

Forslund, D. W., J. M. Kindel, and M. A. Stroscio (1979), Current driven electromagnetic ion cyclotron instability, J. Plasma Phys., 21, 127–139.

Fredricks, R.W., Scarf, F.L. (1973), Recent studies of magnetospheric electric field emissions above the electron gyrofrequency. J. Geophys. Res. **7**8(1), 310–314. doi:10.1029/JA078i001p00310

Fu, H. S., Y. V. Khotyaintsev, M. André, and A. Vaivads (2011), Fermi and betatron acceleration of suprathermal electrons behind depolarization fronts, Geophys. Res. Lett., 38, L16104, doi: 10.1029/2011GL048528.

Fu, H. S., J. B. Cao, F. S. Mozer, H. Y. Lu, and B. Yang (2012a), Chorus intensification in response to interplanetary shock, J. Geophys. Res., 117, A01203, doi: 10.1029/2011JA016913.

Fu, H. S., Y. V. Khotyaintsev, A. Vaivads, M. André, and S. Y. Huang (2012b), Occurrence rate of earthward-propagating dipolarization fronts, Geophys. Res. Lett., 39, L10101, doi: 10.1029/2012GL051784.

Fu, H. S., Y. V. Khotyaintsev, A. Vaivads, M. André, V. A. Sergeev, S. Y. Huang, E. A. Kronberg, and P. W. Daly (2012c), Pitch angle distribution of suprathermal electrons behind dipolarization fronts: A statistical overview, J. Geophys. Res., 117, A12221, doi: 10.1029/2012JA018141.

Fu, H. S., et al. (2013), Dipolarization fronts as a consequence of transient reconnection: In situ evidence, Geophys. Res. Lett., 40, 6023–6027, doi: 10.1002/2013GL058620.

Fu, H. S., et al. (2014), Whistler-mode waves inside flux pileup region: Structured or unstructured?, J. Geophys. Res. Space Physics, 119, 9089– 9100, doi: 10.1002/2014JA020204.

Fu, H. S., Xu, Y., Vaivads, A., & Khotyaintsev, Y. V. (2019). Super-efficient electron acceleration by an isolated magnetic reconnection. Astrophysics Journal Letters, 870(2), L22.

Gabrielse, C., V. Angelopoulos, A. Runov, and D. L. Turner (2014), Statistical characteristics of particle injections throughout the equatorial magnetotail, J. Geophys. Res. Space Physics, 119, 2512–2535, doi: 10.1002/2013JA019638.

Gabrielse, C., C. Harris, V. Angelopoulos, A. Artemyev, and A. Runov (2016), The role of localized inductive electric fields in electron injections around dipolarizing flux bundles, J. Geophys. Res. Space Physics, 121, doi: 10.1002/2016JA023061.

Gabrielse, C., Spanswick, E., Artemyev, A., Nishimura, Y., Runov, A., Lyons, L., Angelopoulos, V., Turner, D.L., Reeves, G.D., McPherron, R., Donovan, E. (2019). Utilizing the Heliophysics/Geospace System Observatory to Understand Particle Injections: Their Scale Sizes and Propagation Directions. J. Geophys. Res.: Space Physics, 124. https://doi.org/10.1029/2018JA025588

Gary, S. P. (1993), Theory of Space Plasma Microinstabilities, Cambridge Univ. Press, New York.

Gary, S.P., and D.W. Forslund (1975), Electromagnetic current instabilities, Phys. Lett. A, 54(4), 347.

Gary, S.P., R.A. Gerwin, and D.W. Forslund (1976), Electromagnetic current instabilities, Phys. Fluids. I9. 579.

Gary, S. P., and Tokar, R. L., (1985) “The electron ‐ acoustic mode.” Physics of Fluids, 28, 2439 ‐ 2441 . https://doi.org/10.1063/1.865250

Gary, S. P., and J. Wang (1996), Whistler instability: Electron anisotropy upper bound, J. Geophys. Res., 101, 10,749– 10,754.

Gary, S. P., D. Winske, and M. Hesse (2000), Electron temperature anisotropy instabilities: Computer simulations, J. Geophys. Res., 105, 10,751.

Gary, S. P., and K. Nishimura (2003), Resonant electron firehose instability: Particle-in-cell simulations, Phys. Plasmas, 10, 3571– 3576.

Gary, S. P., B. Lavraud, M. F. Thomsen, B. Lefebvre, and S. J. Schwartz (2005), Electron anisotropy constraint in the magnetosheath: Cluster observations, Geophys. Res. Lett., 32, L13109.

Gary, S. P., K. Liu, R. E. Denton, and S. Wu (2012), Whistler anisotropy instability with a cold electron component: Linear theory, J. Geophys. Res., 117, A07203, doi: 10.1029/2012JA017631

Gendrin, R., “Pitch angle diffusion of low-energy protons due to gyro-resonant interaction with hydromagnetic waves,” J. Atmos. Terr. Phys., 30, 1313 (1968).

Gendrin, R., “General relationships between wave amplification and particle diffusion in a magnetoplasma,” Rev. Geophys., 19, 171 (1981).

Gurnett, D. A., L. A. Frank, and R. P. Lepping (1976), Plasma waves in the distant magnetotail, J. Geophys. Res., 81, 6059–6071, doi: 10.1029/JA081i034p06059.

Gurnett, D. A., W. S. Kurth, G. B. Hospodarsky, A. M. Persoon, T. F. Averkamp, B. Cecconi, A. Lecacheux, P. Zarka, P. Canu, N. Cornilleau-Wehrlin et al (2005)., Radio and plasma wave observations at Saturn from Cassini’s approach and first orbit, Science, 307, 1255–1259 doi: 10.1126/science.1105356

Hada, T., A. Nishida, T. Terasawa, and E. W. Hones Jr. (1981), Bi-directional electron pitch angle anisotropy in the plasma sheet, J. Geophys. Res., 86, 11,211–11,224, doi: 10.1029/JA086iA13p11211.

Hasegawa, A. (1976), Particle acceleration by MHD surface wave and formation of aurora, J. Geophys. Res., 81(28), 5083–5090, doi:10.1029/JA081i028p05083.

Hayakawa, M., Y. Yamanaka, M. Parrot, F. Lefeuvre (1984), The wave normals of magnetospheric chorus emissions observed on board GEOS 2. J. Geophys. Res. 89, 2811–2821. doi:10.1029/JA089iA05p02811

Hellinger, P., P. M. Trávníˇcek, V. K. Decyk, and D. Schriver (2014), Oblique electron fire hose instability: Particle-in-cell simulations, J. Geophys. Res. Space Physics, 119, 59–68, doi: 10.1002/2013JA019227

Helliwell RA (1965) Whistlers and related ionospheric phenomena. Stanford University Press, Stanford

Helliwell RA (1967), A theory of discrete VLF emissions from the magnetosphere. J. Geophys. Res. **72**, 4773–4790. doi:10.1029/JZ072i019p04773

Horne, R. B. (1989), Path-integrated growth of electrostatic waves: The generation of terrestrial myriametric radiation, J. Geophys. Res., 94(A7), 8895–8909, doi: 10.1029/JA094iA07p08895.

Horne, R. B., R. M. Thorne, N. P. Meredith, and R. R. Anderson (2003), Diffuse auroral electron scattering by electron cyclotron harmonic and whistler mode waves during an isolated substorm, J. Geophys. Res., 108(A7), 1290, doi: 10.1029/2002JA009736.

Horne, R. B., and R. M. Thorne (1998), Potential waves for relativistic electron scattering and stochastic acceleration during magnetic storms, Geophys. Res. Lett., 25, 3011–3014, doi:10.1029/98GL01002.

Horne, R. B., and R. M. Thorne (2000), Electron pitch angle diffusion by electrostatic electron cyclotron harmonic waves: The origin of pancake distributions, J. Geophys. Res., 105(A3), 5391–5402.

Horne, R. B., and R. M. Thorne (2003), Relativistic electron acceleration and precipitation during resonant interactions with whistler-mode chorus. Geophys. Res. Lett. 30(10). doi:10.1029/2003GL016973

Huang, S. Y., M. Zhou, X. H. Deng, Z. G. Yuan, Y. Pang, Q. Wei, W. Su, H. M. Li, and Q. Q. Wang (2012), Kinetic structure and wave properties associated with sharp dipolarization front observed by Cluster, Ann. Geophys., 30, 97–107, doi: 10.5194/angeo-30-97-2012.

Hull, A. J., Chaston, C. C., Bonnell, J. W., Damiano, P. A., Wygant, J. R., & Reeves, G. D. (2020). Correlations between dispersive Alfvén wave activity, electron energization, and ion outflow in the inner magnetosphere. Geophysical Research Letters, 47, e2020GL088985. doi: org/10.1029/2020GL088985

Karpman, V. I., Alekhin, Ju. K., Borisov, N. D., and Rjabova, N. A. (1975) Electrostatic electron cyclotron waves in plasma with a loss-cone distribution, Plasma Phys., 17, 361.

Karimabadi, H., W. Daughton, and K. B. Quest (2004), Role of electron temperature anisotropy in the onset of magnetic reconnection, Geophys. Res.Lett., 31, L18801, doi:10.1029/2004GL020791.

Keiling, A. (2009) Alfvén Waves and Their Roles in the Dynamics of the Earth's Magnetotail: A Review. Space Sci Rev 142**,** 73–156. https://doi.org/10.1007/s11214-008-9463-8

Kellogg, P.J. Cattell, C. A, Goetz, K., Monson, S. J., Wilson, L B. III, Large amplitude whistlers in the magnetosphere observed with Wind-Waves.?? J. Geophys. Res. 116, 9224 (2011). doi: 10.1029/2010JA015919

Kennel, C. (1966). Low‐frequency whistler mode. Physical Fluids, 9, 2190.

Kennel, C. F., and H. E. Petschek (1966), Limit on stable trapped particle fluxes, J. Geophys. Res., 71, 1–28.

Kennel, C., F. Scarf, R. Fredricks, J. McGehee, and F. Coroniti (1970), VLF electric field observations in the magnetosphere

Khazanov, G. V., A. Glocer, and E. W. Himwich (2014), Magnetosphere-ionosphere energy interchange in the electron diffuse aurora, J. Geophys. Res. Space Physics, 119, 171–184, doi: 10.1002/2013JA019325.

Khotyaintsev, Y. V., C. M. Cully, A. Vaivads, M. André, and C. J. Owen (2011), Plasma jet braking: Energy dissipation and nonadiabatic electrons, Phys. Rev. Lett., 106, 165,001.

Kurth, W. S., D. D. Barbosa, D. A. Gurnett, and F. L. Scarf (1980), Electrostatic waves in the Jovian magnetosphere, Geophys. Res. Lett., 7(1), 57–60, doi: 10.1029/GL007i001p0005 7.

Le Contel, O., et al. (2009), Quasi-parallel whistler mode waves observed by THEMIS during near-Earth dipolarizations, Ann. Geophys., 27, 2259–2275.

Le Contel, O., Nakamura, R., Breuillard, H., Argall, M. R., Graham, D. B., Fischer, D., Jaynes, A. N. (2017), Lower hybrid drift waves and electromagnetic electron space-phase holes associated with dipolarization fronts and field-aligned currents observed by the Magnetospheric Multiscale mission during a substorm. Journal of Geophysical Research: Space Physics, 122, 12,236–12,257. doi: /10.1002/2017JA024550

Li, W., R.M. Thorne, N.P. Meredith, R.B. Horne, J. Bortnik, Y.Y. Shprits, B. Ni (2008), Evaluation of whistler mode chorus amplification during an injection event observed on CRRES. J. Geophys. Res. 113, 9210. doi:10.1029/2008JA013129

Li, W., R. M. Thorne, V. Angelopoulos, J. W. Bonnell, J. P. McFadden, C. W. Carlson, O. LeContel, A. Roux, K. H. Glassmeier, and H. U. Auster (2009a), Evaluation of whistler-mode chorus intensification on the nightside during an injection event observed on the THEMIS spacecraft, J. Geophys. Res., 114, A00C14, doi: 10.1029/2008JA013554.

Li, W., R. M. Thorne, V. Angelopoulos, J. Bortnik, C. M. Cully, B. Ni, O. LeContel, A. Roux, U. Auster, and W. Magnes (2009b), Global distribution of whistler-mode chorus waves observed on the THEMIS spacecraft, Geophys. Res. Lett., 36, L09104, doi:10.1029/2009GL037595.

Li, W., J. Bortnik, R. M. Thorne, C. M. Cully, L. Chen, V. Angelopoulos, Y. Nishimura, J. B. Tao, J. W. Bonnell, and O. LeContel (2013), Characteristics of the Poynting flux and wave normal vectors of whistler-mode waves observed on THEMIS, J. Geophys. Res. Space Physics, 118, 1461–1471, doi:10.1002/jgra.50176.

Li, W., R.M. Thorne, Q. Ma, B. Ni, J. Bortnik, D.N. Baker, H.E. Spence, G.D. Reeves, S.G. Kanekal, J.C. Green, C.A. Kletzing, W.S. Kurth, G.B. Hospodarsky, J.B. Blake, J.F. Fennell, S.G. Claudepierre (2014), Radiation belt electron acceleration by chorus waves during the 17 March 2013 storm. J. Geophys. Res. 119, 4681–4693. doi:10.1002/2014JA019945

Li, W., et al. (2016), Unraveling the excitation mechanisms of highly oblique lower band chorus waves, Geophys. Res. Lett., 43, 8867–8875, doi: 10.1002/2016GL070386.

Li, X., and S. R. Habbal (2000), Electron kinetic firehose instability, J. Geophys. Res., 105, 27,377–27,386.

Liang, J., B. Ni, E. Spanswick, M. Kubyshkina, E. F. Donovan, V. M. Uritsky, R. M. Thorne, and V. Angelopoulos (2011), Fast earthward flows, electron cyclotron harmonic waves, and diffuse auroras: Conjunctive observations and a synthesized scenario, J. Geophys. Res., 116, A12220, doi: 10.1029/2011JA017094.

Liang, J., Jiang, F., Donovan, E., Spanswick, E., Angelopoulos, V., and Strangeway, R. (2013): Quasi-parallel electron beams and their possible application in inferring the auroral arc's root in the magnetosphere, Ann. Geophys., 31, 1077-1101, doi:10.5194/angeo-31-1077-2013.

Liu, J., V. Angelopoulos, A. Runov, and X.-Z. Zhou (2013a), On the current sheets surrounding dipolarizing flux bundles in the magnetotail: The case for wedgelets, J. Geophys. Res. Space Physics, 118, 2000–2020, doi: 10.1002/jgra.50092.

Liu, J., V. Angelopoulos, X.-Z. Zhou, A. Runov, and Z. H. Yao (2013b), On the role of pressure and flow perturbations around dipolarizing flux bundles, J. Geophys. Res. Space Physics, 118, 7104–7118, doi: 10.1002/2013JA019256.

Liu, J., V. Angelopoulos, X.-Z. Zhou, and A. Runov (2014), Magnetic flux transport by dipolarizing flux bundles, J. Geophys. Res. Space Physics, 119, 909–926, doi: 10.1002/2013JA019395.

Liu, J., V. Angelopoulos, X. Chu, X.-Z. Zhou, and C. Yue (2015), Substorm current wedge composition by wedgelets, Geophys. Res. Lett., 42, 1669–1676, doi: 10.1002/2015GL063289.

Liu C. M. and H. S. Fu (2019), Anchor Point of Electron Acceleration around Dipolarization Fronts in Space Plasmas, ApJL 873 L2, doi:10.3847/2041-8213/ab06cb.

Liu, X., L. Chen, W. Gu, X.-J. Zhang, Electron cyclotron harmonic wave instability by loss cone distribution. J. Geophys. Res. 123, 9035–9044 (2018). https://doi.org/10.1029/2018JA025925

Liu, X., Chen, L., Engel, M. A., & Jordanova, V. K. (2020). Global simulation of electron cyclotron harmonic wave instability in a storm-time magnetosphere. Geophysical Research Letters, 47, e2019GL086368. https://doi.org/10.1029/2019GL086368

Lu, Q. M., S. Wang, and X. K. Dou (2005), Electrostatic waves in an electron - beam plasma system, Phys. Plasmas, 12, 072903, doi:10.1063/1.1951367

Lu, S., V. Angelopoulos, and H. Fu (2016), Suprathermal particle energization in dipolarization fronts: Particle-in-cell simulations, J. Geophys. Res. Space Physics, 121, doi: 10.1002/2016JA022815

Lyons, L. R., Thorne, R. M., & Kennel, C. F. (1972). Pitch-angle diffusion of radiation belt electrons within the plasmasphere. Journal of Geophysical Research, **77**, 3455.

Lyons, L. (1974), Electron diffusion driven by magnetospheric electrostatic waves, J. Geophys. Res., 79(4), 575–580.

Lyons, L. R. (1984): Electron energization in the geomagnetic tail current sheet, J. Geophys. Res., 89, 5479–5487, doi: 10.1029/JA089iA07p05479.

Lysak, R. L., and Y. Song (2003), Kinetic theory of the Alfvén wave acceleration of auroral electrons, J. Geophys. Res., 108(A4), 8005, doi:10.1029/2002JA009406

Malaspina, D. M., J. R. Wygant, R. E. Ergun, G. D. Reeves, R. M. Skoug, and B. A. Larsen (2015), Electric field structures and waves at plasma boundaries in the inner magnetosphere, J. Geophys. Res. Space Physics, 120, 4246–4263, doi: 10.1002/2015JA021137.

McFadden, J. P., C. W. Carlson, D. Larson, M. Ludlam, R. Abiad, B. Elliott, P. Turin, M. Marckwordt, and V. Angelopoulos (2008), The THEMIS ESA plasma instrument and in-flight calibration, Space Sci. Rev., 141, 277–302, doi: 10.1007/s11214-008-9440-2.

Menietti, J. D., O. Santolik, J. D. Scudder, J. S. Pickett, and D. A. Gurnett (2002), Electrostatic electron cyclotron waves generated by low-energy electron beams, J. Geophys. Res., 107(A10), 1285, doi: 10.1029/2001JA009223.

Menietti, J. D., O. Santolik, A. M. Rymer, G. B. Hospodarsky, A. M. Persoon, D. A. Gurnett, A. J. Coates, and D. T. Young (2008), Analysis of plasma waves observed within local plasma injections seen in Saturn's magnetosphere, J. Geophys. Res., 113, A05213, doi: 10.1029/2007JA012856.

Menietti, J. D., Y. Y. Shprits, R. B. Horne, E. E. Woodfield, G. B. Hospodarsky, and D. A. Gurnett (2012), Chorus, ECH, and Z mode emissions observed at Jupiter and Saturn and possible electron acceleration, J. Geophys. Res., 117, A12214, doi: 10.1029/2012JA018187.

Meredith, N. P., R. B. Horne, A. D. Johnstone, and R. R. Anderson (2000), The temporal evolution of electron distributions and associated wave activity following substorm injections in the inner magnetosphere, J. Geophys. Res., 105(A6), 12,907–12,917, doi: 10.1029/2000JA900010.

Meredith, N. P., R. B. Horne, R. M. Thorne, and R. R. Anderson (2003), Favored regions for chorus-driven electron acceleration to relativistic energies in the Earth's outer radiation belt, Geophys. Res. Lett., 30(16), SSC 7–1, doi:10.1029/2003GL017698.

Meredith, N. P., R. B. Horne, R. M. Thorne, D. Summers, and R. R. Anderson (2004), Substorm dependence of plasmaspheric hiss, J. Geophys. Res., 109, A06209, doi:10.1029/2004JA010387.

Meredith, N. P., R. B. Horne, R. M. Thorne, and R. R. Anderson (2009), Survey of upper band chorus and ECH waves: Implications for the diffuse aurora, J. Geophys. Res., 114, A07218, doi: 10.1029/2009JA014230.

Millan, R. M., R. P. Lin, D. M. Smith, and M. P. McCarthy (2007), Observation of relativistic electron precipitation during a rapid decrease of trapped relativistic electron flux, Geophys. Res. Lett., 34, L10101, doi: 10.1029/2006GL028653

Mourenas, D., & Beghin, C. (1991). Packets of cyclotron waves induced by electron beam injection from the space shuttle 1. Linear theory. Radio Science, 26(2), 469– 479. https://doi.org/10.1029/90RS02580

Mourenas, D., C. Beghin, and J.-P. Lebreton, Electron cyclotron and upper hybrid harmonics produced by electron beam injections on Spacelab 1, Ann. Geophys.,7, 519, 1989.

Mourenas, D., A.V. Artemyev, O.V. Agapitov, V. Krasnoselskikh, F.S. Mozer, Very oblique whistler generation by low-energy electron streams. J. Geophys. Res. 120, 3665–3683 (2015). doi: 10.1002/2015JA021135

Mozer, F S., Carlson, C. W., Hudson, M. K., Torbert, R. B., Parady, B., Yatteau, J., & Kelley, M. C. (1977). Observations of paired electrostatic shocks in the polar magnetosphere. Physical Review Letters, 38, 292.

Mozer, F. S., O. V. Agapitov, A. Artemyev, J. F. Drake, V. Krasnoselskikh, S. Lejosne, and I. Vasko (2015), Time domain structures: What and where they are, what they do, and how they are made, Geophys. Res. Lett., 42, 3627–3638, doi: 10.1002/2015GL063946.

Nakamura, R., et al. (2002), Motion of the dipolarization front during a flow burst event observed by Cluster, Geophys. Res. Lett., 29(20), 1942, doi: 10.1029/2002GL015763.

Newell, P. T., T. Sotirelis, and S. Wing (2009), Diffuse, monoenergetic, and broadband aurora: The global precipitation budget, *J. Geophys. Res.*, *114*, A09207, doi:10.1029/2009JA014326.

Ni, B., R. Thorne, J. Liang, V. Angelopoulos, C. Cully, W. Li, X. Zhang, M. Hartinger, O. Le Contel, and A. Roux (2011a), Global distribution of electrostatic electron cyclotron harmonic waves observed on THEMIS, Geophys. Res. Lett., 38, L17105, doi: 10.1029/2011GL048793

Ni, B., R. M. Thorne, R. B. Horne, N. P. Meredith, Y. Y. Shprits, L. Chen, and W. Li (2011b), Resonant scattering of plasma sheet electrons leading to diffuse auroral precipitation: 1. Evaluation for electrostatic electron cyclotron harmonic waves, J. Geophys. Res., 116, A04218, doi:10.1029/2010JA016232.

Ni, B., R. M. Thorne, N. P. Meredith, R. B. Horne, and Y. Y. Shprits (2011c), Resonant scattering of plasma sheet electrons leading to diffuse auroral precipitation: 2. Evaluation for whistler mode chorus waves, J. Geophys. Res., 116, A04219, doi:10.1029/2010JA016233.

Ni, B., J. Liang, R. M. Thorne, V. Angelopoulos, R. B. Horne, M. Kubyshkina, E. Spanswick, E. F. Donovan, and D. Lummerzheim (2012), Efficient diffuse auroral electron scattering by electrostatic electron cyclotron harmonic waves in the outer magnetosphere: A detailed case study, J. Geophys. Res., 117, A01218, doi:10.1029/2011JA017095.

Ni, B., Thorne, R. M., Zhang, X., Bortnik, J., Pu, Z., Xie, L., et al. (2016). Origins of the Earth's diffuse auroral precipitation. Space Science Reviews,200, 205–259. https://doi.org/10.1007/s11214-016-0234-7

Ni, B., Gu, X., Fu, S., Xiang, Z., & Lou, Y. (2017). A statistical survey of electrostatic electron cyclotron harmonic waves based on THEMIS FFF wave data. Journal of Geophysical Research: Space Physics, 122, 3342– 3353. https://doi.org/10.1002/2016JA023433

Nishimura, Y., J. Bortnik, W. Li, R.M. Thorne, L.R. Lyons, V. Angelopoulos, S.B. Mende, J.W. Bonnell, O. Le Contel, C. Cully, R. Ergun, U. Auster (2010), Identifying the driver of pulsating aurora. Science 330, 81. doi:10.1126/science.1193186

Northrop, T. G. (1963), The Adiabatic Motion of Charged Particles, Intersci. Publ., New York.

Ohtani, S., M. A. Shay, and T. Mukai (2004), Temporal structure of the fast convective flow in the plasma sheet: Comparison between observations and two-fluid simulations, J. Geophys. Res., 109, A03210, doi:10.1029/2003JA010002.

Omura, Y., and H. Matsumoto (1987), Competing processes of whistler and electrostatic instabilities in the magnetosphere, Journal of Geophysical Research: Space Physics 92, 8649-8659.

Omura, Y., and D. Nunn (2011), Triggering process of whistler mode chorus emissions in the magnetosphere, J. Geophys. Res., 116, A05205, doi:10.1029/2010JA016280.

Perraut, S., O. Le Contel, A. Roux, and A. Pedersen (2000), Current-driven electromagnetic ion cyclotron instability at substorm onset, J. Geophys. Res., 105, 21,097–21,107.

Pritchett, P. L., and F. V. Coroniti (1998), Interchange instabilities and localized high-speed flows in the convectively-driven near-Earth plasma sheet, in Substorms-4, edited by S. Kokubun and Y. Kamide, pp. 443, Kluwer Acad., Dordrecht.

Pritchett, P. L., and F. V. Coroniti (2010), A kinetic ballooning/interchange instability in the magnetotail, J. Geophys. Res., 115, A06301, doi: 10.1029/2009JA014752.

Pritchett, P. L., and F. V. Coroniti (2013), Structure and consequences of the kinetic ballooning/interchange instability in the magnetotail, J. Geophys. Res. Space Physics, 118, 146–159, doi: 10.1029/2012JA018143.

Pritchett, P. L., F. V. Coroniti, and Y. Nishimura (2014), The kinetic ballooning/interchange instability as a source of dipolarization fronts and auroral streamers, J. Geophys. Res. Space Physics, 119, 4723–4739, doi: 10.1002/2014JA019890.

Roeder, J. L., and H. C. Koons (1989), A survey of electron cyclotron waves in the magnetosphere and the diffuse auroral electron precipitation, J. Geophys. Res., 94(A3), 2529–2541, doi: 10.1029/JA094iA03p02529.

Roeder, J. L., Angelopoulos, V., Baumjohann, W., & Anderson, R. R. (1991). Observations of correlated broadband electrostatic noise and electron cyclotron emissions in the plasma sheet. Geophysical Research Letters, 18(1), 53– 56. doi: 10.1029/90GL02036

Ronnmark, K. (1982), WHAMP- Waves in Homogeneous Anisotropic Multicomponent Plasmas, Kiruna Geophys. Rep. 179, Kiruna Geophys. Inst., Kiruna.

Roux, A., O. Le Contel, C. Coillot, A. Bouabdellah, B. de la Porte, D. Alison, S. Ruocco, and M. C. Vassal (2008), The search coil magnetometer for THEMIS, Space Sci. Rev., 141, 265–275, doi: 10.1007/s11214-008-9455-8.

Runov, A., V. Angelopoulos, M. I. Sitnov, V. A. Sergeev, J. Bonnell, J. P. McFadden, D. Larson, K. Glassmeier, and U. Auster (2009), THEMIS observations of an earthward-propagating dipolarization front, Geophys. Res. Lett., 36, L14106, doi: 10.1029/2009GL038980.

Runov, A., V. Angelopoulos, X.-Z. Zhou, X.-J. Zhang, S. Li, F. Plaschke, and J. Bonnell (2011), ATHEMIS multicase study of dipolarization fronts in the magnetotail plasma sheet, J. Geophys. Res., 116, A05216, doi: 10.1029/2010JA016316.

Runov, A., V. Angelopoulos, C. Gabrielse, J. Liu, D. L. Turner, and X.-Z. Zhou (2015), Average thermodynamic and spectral properties of plasma in and around dipolarizing flux bundles, J. Geophys. Res. Space Physics, 120, 4369–4383, doi: 10.1002/2015JA021166.

Russell, C. T., R. E. Holzer, and E. J. Smith (1969), OGO 3 observations of ELF noise in the magnetosphere: 1. Spatial extent and frequency of occurrence, J. Geophys. Res., **7**4, 755–777.

Santolík, O., D. A. Gurnett, J. S. Pickett, M. Parrot, and N. Cornilleau-Wehrlin (2003), Spatiotemporal structure of storm-time chorus, J. Geophys. Res., 108(A7), 1278, doi:10.1029/2002JA009791.

Santolík, O., et al. (2010a), Wave-particle interactions in the equatorial source region of whistler-mode emissions, J. Geophys. Res., 115, A00F16, doi: 10.1029/2009JA015218.

Santolík, O., J. S. Pickett, D. A. Gurnett, J. D. Menietti, B. T. Tsurutani, and O. Verkhoglyadova (2010b), Survey of Poynting flux of whistler mode chorus in the outer zone, J. Geophys. Res., 115, A00F13, doi: 10.1029/2009JA014925

Scarf, F. L., R. W. Fredricks, C. F. Kennel, and F. V. Coroniti (1973), Satellite studies of magnetospheric substorms on August 15, 1968: 8. Ogo 5 plasma wave observations, J. Geophys. Res., 78(16), 3119–3130, doi: 10.1029/JA078i016p03119.

Schmid, D., M. Volwerk, R. Nakamura, W. Baumjohann, and M. Heyn (2011), A statistical and event study of magnetotail dipolarization fronts, Ann. Geophys., 29, 1537–1547.

Sergeev, V. A., E. M. Sazhina, N. A. Tsyganenko, J. A. Lundblad, and F. Soraas (1983), Pitch-angle scattering of energetic electrons in the magnetotail current sheet as the dominant source of their isotropic precipitation into the nightside ionosphere, Planet. Space Sci., 31(10), 1147–1155.

Sergeev, V. A., K. Liou, C.-. I. Meng, P. T. Newell, M. Brittnacher, G. Parks, and G. D. Reeves (1999), Development of auroral streamers in association with localized impulsive injections to the inner magnetotail, Geophys. Res. Lett., 26, 417–420, doi: 10.1029/1998GL900311.

Sergeev, V. A., V. Angelopoulos, S. Apatenkov, J. Bonnell, R. Ergun, R. Nakamura, J. McFadden, D. Larson, and A. Runov (2009), Kinetic structure of the sharp injection/dipolarization front in the flow-braking region, Geophys. Res. Lett., 36, L21105, doi: 10.1029/2009GL040658.

Shaw, R. R., and D. A. Gurnett (1975), Electrostatic noise bands associated with the electron gyrofrequency and plasma frequency in the outer magnetosphere, J. Geophys. Res., 80(31), 4259–4271, doi: 10.1029/JA080i031p04259.

Shklyar, D., Matsumoto, H. (2009) Oblique Whistler-Mode Waves in the Inhomogeneous Magnetospheric Plasma: Resonant Interactions with Energetic Charged Particles. Surv Geophys 30, 55–104. https://doi.org/10.1007/s10712-009-9061-7

Sibeck, D. G., and V. Angelopoulos (2008), THEMIS science objectives and mission phases, Space Sci. Rev., 141, 35–59, doi: 10.1007/s11214-008-9393-5.

Singh, S. V., and G. S. Lakhina (2001), Generation of electron ‐ acoustic waves in the magnetosphere, Planet. Space Sci., 49, 107 ‐ 114.

Sitnov, M. I., M. Swisdak, and A. V. Divin (2009), Dipolarization fronts as a signature of transient reconnection in the magnetotail, J. Geophys. Res., 114, A04202, doi: 10.1029/2008JA013980.

Sonwalkar, V. S., & Inan, U. S. (1989). Lightning as an embryonic source of VLF hiss. Journal of Geophysical Research, 94, 6986– 6994. https://doi.org/10.1029/JA094iA06p06986

Stasiewicz, K., et al. (2000), Small scale Alfvénic structure in the aurora, Space Sci. Rev., 92, 423–533, doi:10.1023/A:1005207202143.

Stix, T. H. 1962, The Theory of Plasma Waves (New York: McGraw-Hill)

Štverák, Ś., P. Trávníček, M. Maksimovic, E. Marsch, A. N. Fazakerley, and E. E. Scime (2008), Electron temperature anisotropy constraints in the solar wind, J. Geophys. Res., 113, A03103, doi: 10.1029/2007JA012733

Summers, D., R. M. Thorne, and F. Xiao (1998), Relativistic theory of wave-particle resonant diffusion with application to electron acceleration in the magnetosphere, J. Geophys. Res., 103, 20,487.

Summers, D., C. Ma, N. P. Meredith, R.B. Horne, R.M. Thorne, D. Heynderickx, R.R. Anderson (2002), Model of the energization of outer-zone electrons by whistler-mode chorus during the October 9, 1990 geomagnetic storm. Geophys. Res. Lett. **29**(24). doi:10.1029/2002GL016039

Sundkvist, D., et al. (2012), Dispersive nature of high Mach number collisionless plasma shocks: Poynting flux of oblique whistler waves, Phys. Rev. Lett., 108(2), 025002.

Tao, X., R. M. Thorne, R. B. Horne, S. Grimald, C. S. Arridge, G. B. Hospodarsky, D. A. Gurnett, A. J. Coates, and F. J. Crary (2010), Excitation of electron cyclotron harmonic waves in the inner Saturn magnetosphere within local plasma injections, J. Geophys. Res., 115, A12204, doi: 10.1029/2010JA015598.

Tao, X., L. Chen, X. Liu, Q. Lu, and S. Wang (2017), Quasilinear analysis of saturation properties of broadband whistler mode waves, Geophys. Res. Lett., 44, 8122–8129, doi: 10.1002/2017GL074881

Temerin, M., Cerny, K., Lotko, W., & Mozer, E S. (1982). Observations of double layers and solitary waves in the auroral plasma. Physical Review Letters, 48, 1175.

Thorne, R. M., E. J. Smith, R. K. Burton, and R. E. Holzer (1973), Plasmaspheric hiss, J. Geophys. Res., 78, 1581.

Thorne, R. M., R. B. Horne, S. A. Glauert, N. P. Meredith, Y. Shprits, D. Summers, and R. R. Anderson (2005), The influence of wave ‐ particle interactions on relativistic electron dynamics during storms, in Inner Magnetosphere Interactions: New Perspectives from Imaging, edited by J. Burch, M. Schulz, and H. Spence, pp. 101– 112, AGU, Washington, D. C., doi:10.1029/159GM07.

Thorne, R. M. (2010), Radiation belt dynamics: The importance of wave-particle interactions, Geophys. Res. Lett., 37, L22107, doi: 10.1029/2010GL044990.

Thorne, R. M., B. Ni, X. Tao, R. B. Horne, and N. P. Meredith (2010), Scattering by chorus waves as the dominant cause of diffuse auroral precipitation, Nature, 467, 943–946, doi: 10.1038/nature09467.

Thorne, R., Li, W., Ni, B. et al (2013). Rapid local acceleration of relativistic radiation-belt electrons by magnetospheric chorus. Nature 504**,** 411–414. https://doi.org/10.1038/nature12889

Tsurutani, B. T., and E. J. Smith (1974), Postmidnight Chorus: A Substorm Phenomenon, J. Geophys. Res., 79, 118–127, doi:10.1029/JA079i001p00118.

Tverskoy, B. A. (1969). Main mechanisms in the formation of the Earth's radiation belts. Reviews of Geophysics and Space Physics, 7(1, 2), 219– 231. doi: /10.1029/RG007i001p00219

Vasko, I. Y., O.V. Agapitov, F.S. Mozer, J. W. Bonnell, A. V. Artemyev, V. V. Krasnoselskikh, G. Reeves, and G. Hospodarsky (2017), Electron-acoustic solitons and double layers in the inner magnetosphere, Geo-phys. Res. Lett., 44, 4575–4583, doi:10.1002/2017GL074026

Vedenov, A. A., & Sagdeev, R. Z. (1961). Some properties of plasma with an anisotropic ion velocity distribution in a magnetic field. Plasma Physics and the Problem of Controlled Thermonuclear Reactions, 3, 332– 339.

Viberg, H., Y. V. Khotyaintsev, A.Vaivads, M. André, H. S. Fu, and N. Cornilleau-Wehrlin (2014), Whistler mode waves at magnetotail dipolarization fronts, J. Geophys. Res. Space Physics, 119, 2605–2611, doi:10.1002/2014JA019892

Walsh, A. P., C. J. Owen, A. N. Fazakerley, C. Forsyth, and I. Dandouras (2011), Average magnetotail electron and proton pitch angle distributions from Cluster PEACE and CIS observations, Geophys. Res. Lett., 38, L06103, doi: 10.1029/2011GL046770.

Walsh, A. P., A. N. Fazakerley, C. Forsyth, C. J. Owen, M. G. G. T. Taylor, and I. J. Rae (2013), Sources of electron pitch angle anisotropy in the magnetotail plasma sheet, J. Geophys. Res. Space Physics, 118, 6042–6054, doi:10.1002/jgra.50553.

Wilson, L. B. III (2016) Low Frequency Waves at and Upstream of Collisionless Shocks, in Low-Frequency Waves in Space Plasmas (eds A. Keiling, D.-H. Lee and V.Nakariakov), John Wiley & Sons, Inc, Hoboken, NJ. doi:10.1002/9781119055006.ch16

Wygant, J.R., et al. (2002), Evidence for kinetic Alfvén waves and parallel electron energization at 4-6 Re altitudes in the plasma sheet boundary layer. J. Geophys. Res. 107(A8), 1201. doi:10.1029/2001JA900113

Xu, Y., Fu, H. S., Norgren, C., Hwang, K.-J., & Liu, C. M. (2018). Formation of dipolarization fronts after current sheet thinning. Physics of Plasmas, 25(7), 072123. doi: 10.1063/1.5030200.

Yang, J., J. B. Cao, H. S. Fu, T. Y. Wang, W. L. Liu, and Z. H. Yao (2017), Broadband high-frequency waves detected at dipolarization fronts, J. Geophys. Res. Space Physics, 122, 4299–4307, doi: 10.1002/2016JA023465.

Yao, Z. H., et al. (2015), A physical explanation for the magnetic decrease ahead of dipolarization fronts, Ann. Geophys., 33(10), 1301-C1309, doi:10.5194/angeo-33-1301-2015.

Yao, Z., et al. (2016), Substructures within a dipolarization front revealed by high-temporal resolution Cluster observations, J. Geophys. Res. Space Physics, 121, 5185-C5202, doi:10.1002/2015JA022238.

Young, T. S. T., J. D. Callen, and J. E. McCune (1973), High‐frequency electrostatic waves in the magnetosphere, J. Geophys. Res., 78(7), 1082–1099, doi: 10.1029/JA078i007p01082.

Yue, C., X. An, J. Bortnik, Q. Ma, W. Li, R. M. Thorne, G. D. Reeves, M. Gkioulidou, D. G. Mitchell, and C. A. Kletzing (2016), The relationship between the macroscopic state of electrons and the properties of chorus waves observed by the Van Allen Probes, Geophys. Res. Lett., 43, 7804–7812, doi: 10.1002/2016GL070084.

Zelenyi, L. M., Zogin, D. V., and Buchner, J.: Quasi adiabatic dynamics of charged particles in the tail of the magnetosphere, Cosmic Research, 28, 369–380, 1990.

Zhang, X.-J., and V. Angelopoulos (2014), On the relationship of electrostatic cyclotron harmonic emissions with electron injections and dipolarization fronts, J. Geophys. Res. Space Physics, 119, 2536–2549, doi: 10.1002/2013JA019540.

Zhang, X.-J., V. Angelopoulos, B. Ni, R. M. Thorne, and R. B. Horne (2013), Quasi-steady, marginally unstable electron cyclotron harmonic wave amplitudes, J. Geophys. Res. Space Physics, 118, 3165–3172, doi:10.1002/jgra.50319.

Zhang, X.-J., V. Angelopoulos, B. Ni, R. M. Thorne, and R. B. Horne (2014), Extent of ECH wave emissions in the Earth's magnetotail, J. Geophys. Res. Space Physics, 119, 5561 – 5574, doi:10.1002/2014JA019931.

Zhang, X.-J., V. Angelopoulos, B. Ni, and R. M. Thorne (2015), Predominance of ECH wave contribution to diffuse aurora in Earth's outer magnetosphere, J. Geophys. Res. S pace Physics, 120,295–309, doi:10.1002/2014JA020455

Zhang, X., V. Angelopoulos, P. L. Pritchett, and J. Liu (2017), Off-equatorial current-driven instabilities ahead of approaching dipolarization fronts, J. Geophys. Res. Space Physics, 122, 5247–5260, doi: 10.1002/2016JA023421.

Zhang, X., Angelopoulos, V., Artemyev, A. V., & Liu, J. (2018). Whistler and electron firehose instability control of electron distributions in and around depolarizing flux bundles. Geophysical Research Letters, 45, 9380–9389. doi: /10.1029/2018GL079613

Zhang, X., Angelopoulos, V., Artemyev, A. V., & Liu, J. (2019). Energy transport by whistler waves around dipolarizing flux bundles. Geophysical Research Letters, 46. https://doi.org/10.1029/2019GL084226

Zhang, X., Angelopoulos, V., Artemyev, A. V., Zhang, X.-J., & Liu, J. (2021). Beam-driven electron cyclotron harmonic waves in Earth's magnetotail. Journal of Geophysical Research: Space Physics, 126, e2020JA028743. doi: 10.1029/2020JA028743

Zhang, Y., H. Matsumoto, and H. Kojima (1999), Whistler mode waves in the magnetotail, J. Geophys. Res., 104, 28,633–28,644, doi: 10.1029/1999JA900301.

Zhou, M., M. Ashour-Abdalla, X. Deng, D. Schriver, M. El-Alaoui, and Y. Pang (2009), THEMIS observation of multiple dipolarization fronts and associated wave characteristics in the near-Earth magnetotail,Geophys. Res. Lett., 36, L20107, doi: 10.1029/2009GL040663.